Spring 2014

Application of electrically invisible antennas to the modulated scatterer technique

Dylan Andrew Crocker

Department:

APPLICATION OF ELECTRICALLY INVISIBLE ANTENNAS TO THE MODULATED SCATTERER TECHNIQUE

by

DYLAN ANDREW CROCKER

A THESIS

Presented to the Faculty of the Graduate School of the

MISSOURI UNIVERSITY OF SCIENCE AND TECHNOLOGY

In Partial Fulfillment of the Requirements for the Degree

MASTER OF SCIENCE IN ELECTRICAL ENGINEERING

2014

Approved by

Kristen M. Donnell, Advisor
David Pommerenke
Reza Zoughi

ABSTRACT

The Modulated Scatterer Technique (MST) has shown promise for applications in microwave imaging, electric field mapping, and materials characterization. Traditionally, MST scatterers consist of dipole antennas centrally loaded with a lumped element capable of modulation (commonly a PIN diode). By modulating the load element, the signal scattered from the MST scatterer is also modulated. However, due to the small size of such scatterers, it can be difficult to reliably detect the modulated signal. Increasing the modulation depth (a parameter related to how well the scatterer modulates the scattered signal) may improve the detectability of the scattered signal. In an effort to improve the modulation depth of scatterers commonly used in MST, the concept of electrically invisible antennas is applied to the design of these scatterers and is the focus of this work. Electrical invisibility of linear antennas, such as loaded dipoles, can be achieved by loading a scatterer in such a way that, when illuminated by an electromagnetic wave, the integral of the current induced along the length of the scatterer (and hence the scattered field as well) approaches zero. By designing a scatterer to be capable of modulation between visible (scattering) and invisible (minimum scattering) states, the modulation depth may be improved. This thesis presents simulations and measurements of new MST scatterers that have been designed to be electrically invisible during the reverse bias state of the modulated element (i.e., a PIN diode). Further, the scattering during the forward bias state remains the same as that of a traditional MST scatterer, resulting in an increase in modulation depth. This new MST scatterer design technique may also have application in improving the performance of similar sensors such as radio frequency identification (RFID) tags.

ACKNOWLEDGMENTS

Thank you to my Advisor Dr. Kristen Donnell for all her encouragement, guidance, and patient support. I would also like to thank my committee members Dr. Reza Zoughi and Dr. David Pommerenke for their valuable work serving on my committee as well personally teaching me many things regarding microwave engineering. Special thanks to my friends and colleagues at the applied microwave nondestructive testing laboratory (*amntl*), in particular Dr. Tayeb Ghasr, for their valuable help and collaboration.

Thanks to Sandia National Laboratories for making it possible for me to attend graduate school through their Critical Skills Master's Program. Thank you to my colleagues at Sandia, especially my manager Earl, for all the support and encouragement.

I would like to thank my family and friends without whom I could not have accomplished this work. Thank you to my wife Grace who spent many long hours as a "single mom" while I was busy with school as well as always supporting and encouraging me. Without her I could not have survived all the work and stress. Thank you to my two wonderful children who have provided so much happiness and relief by all the smiles and hugs for their dad! I would also like to thank my parents and siblings for their constant support and encouragement throughout my life. Also, my in-laws have given my family much support during our time as students. Thank you to all our friends at Rolla Bible Church for all their prayers and support of my family during our time here in Rolla.

Thanks most importantly to Jesus who has saved me from myself and continues every day to make me in all ways a better person.

This work was supported by Sandia National Laboratories, Albuquerque, NM, through their Critical Skills Master's Program.

TABLE OF CONTENTS

LIST OF ILLUSTRATIONS

Page

LIST OF TABLES

Page

1. INTRODUCTION

1.1. THE MODULATED SCATTERER TECHNIQUE (MST)

Modulated Scatterer Technique (MST) has shown potential for microwave imaging, electric field mapping, and materials characterization applications [1]-[4]. The technique is based on irradiating a small scatterer (typically a resonant dipole centrally loaded with a PIN diode) with an electromagnetic wave. This incident wave induces a current on the dipole, corresponding to its geometry. This induced current subsequently causes the element to re-radiate, or scatter, an additional signal related to the incident signal and scatterer geometry [5]. Loading the dipole antenna with a PIN diode enables the dipole impedance to be (electronically) changed by modulating the PIN diode bias between a forward and reverse state in a controlled manner. In this way, the distribution of current induced along the dipole will also be modulated. Subsequently, the scattering from the dipole will also be modulated and can be uniquely distinguished from the scattering of other objects [1]. More specifically, signal detection is improved with modulation since modulated signals are distinct from non-coherent clutter present in the environment and noise in the detection system. Additionally, with regard to an array of MST scatterers, modulation allows an array element to "tag" its own signal, providing a means for spatial identification of the location from which the signal is received.

Recently, a new MST scatterer design was proposed (primarily for embedded sensing applications including materials characterization), consisting of a dual loaded dipole scatterer, referred to as a dual loaded scatterer, or DLS [6]-[7]. A schematic of the traditional MST scatterer and DLS is provided in Figure 1.1. The DLS differs from the (single-loaded) conventional MST scatterer as it is loaded with two PIN diodes instead of one, each offset from the center by a distance, d_z. The dual-loading results in four possible (modulation) states of the scatterer (as opposed to two for traditional MST scatterers). For materials characterization, the scattered signal from all four states can be used, together in the form of a differential ratio calculation, to remove unwanted signals (common to all states, including the carrier signal) from the total detected signal [7]. This ratio can then be related to properties of the material in the vicinity of the DLS.

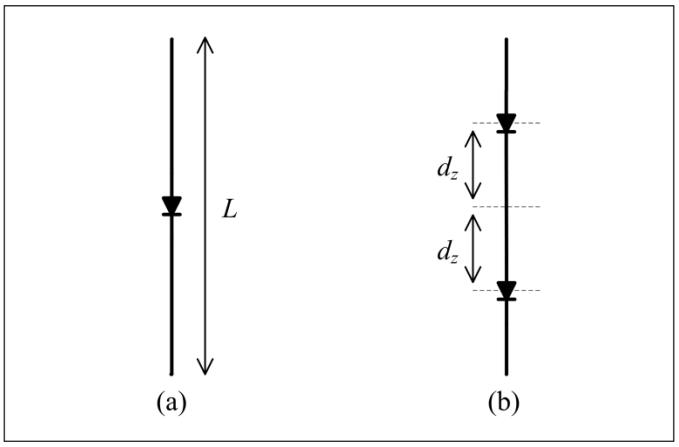

Figure 1.1. Schematic of MST elements: (a) Traditional MST element (dipole centrally loaded with a PIN diode), (b) recently proposed dual loaded MST scatterer (DLS).

In either configuration (single or dual loaded), the MST scatterer is usually quite small and therefore the (modulated) scattering is also quite small. Hence, the residual carrier (i.e., the incident signal present in the scattered signal), can significantly limit the dynamic range of a detection system [8]. Furthermore, in array applications, the mutual coupling between elements of different modulation states within an array of MST scatterers can result in far-field calculation errors [8]. Increasing the capability of the scatterer to modulate the scattered signal may help to mitigate these issues and make this technique more robust. One method used to describe this capability is through a quantity known as modulation depth (MD).

1.2. MODULATION DEPTH

Modulation depth is a dimensionless quantity defined as the amplitude ratio of the power in the modulated signal to the power in the carrier, expressed as a percentage [9]. It can also be defined as a ratio of signal amplitudes (e.g., S-parameters or electric field) [9]. For the purposes of this work, MD will be determined in terms of signal amplitude and calculated as shown below in (1) [9]:

$$MD = \frac{A - B}{A + B} * 100\% \tag{1}$$

where A is the maximum peak-to-peak amplitude of the scattered electric field, and B is the minimum peak-to-peak amplitude of the scattered electric field. MD is useful to consider with respect to modulated scatterers since it quantifies how well a scatterer can modulate the scattered signal. Improving the MD may help mitigate the detection issues mentioned above (e.g., limitations on the detection system dynamic range, mutual coupling, etc.), since an increase in the MD indicates an increase in the relative power of the modulated signal to that of the carrier, thus potentially decreasing the required sensitivity of the detection system. Consequently, weak scattering objects (such as MST scatterers) may be more reliably detected [10]. Such an approach has been applied in the radio frequency identification (RFID) regime to improve and optimize the performance (operating range, data rate, etc.) of RFID tags [11]-[12]. More specifically, techniques have been developed in order to maximize the difference in power received (related to the differential radar cross section of the tag [12]) between the modulation states of RFID tags [11].

Additionally, the concept of improving MD has already been applied for increasing the robustness of MST scatterers as well. In [13], in order to maximize the MD, a printed dipole with length, L, of $\lambda/10$ (see Figure 1.1) was centrally loaded with an optical diode which was conjugate matched (during the forward biased state) to the input impedance of the dipole. Another technique was proposed in [10] which maximizes the MD by maximizing the scattered power of the MST element during the diode forward state for short ($L \leq 0.4\lambda$) MST elements. However, these techniques do not address unwanted mutual coupling between nearby elements (an issue that may be encountered in array applications). Therefore, to continue the improvements to MST, this work focuses on applying the concept of electrically invisible antennas [14]-[18] to the design of MST scatterers in order to improve the MD.

1.3. INVISIBLE SCATTERERS

Previous work has shown that electrically invisible antennas have application in reduction of radar cross section [19], frequency-selective surfaces [20], reconfigurable antennas [15], [18], as well as reduction in mutual coupling between array elements [15].

Considering these applications with respect to MST, by designing an MST scatterer that can operate in electrically visible (i.e., scattering) and invisible (i.e. minimum/zero scattering) states, the MD may be enhanced [21].

In [14]-[18], it is shown that a linear scatterer may be loaded in such a way that the integral of the induced current distribution, and the subsequent scattering, approaches zero (i.e., the scatter becomes electrically invisible). However, without the ability to change between visible and invisible states, such a scatterer's practical application may be limited (unless the precise scattering response is *a priori* known). This implies the need for a second load capable of modulation. Building on the DLS design (illustrated in Figure 1.1) mentioned above, this work focuses on the integration of electrically invisible antennas to the DLS design. By choosing the loading characteristics of the DLS (i.e., load location and type) in a specific way, the DLS can be designed to be electrically invisible during one state of the modulating load. Such a DLS is herein known as the invisible DLS or IDLS. For this work, an IDLS is designed to have one fixed load (e.g., a lumped element), and one load capable of modulation (e.g., a PIN diode). In this way, the IDLS will have two states (similar to the conventional single-loaded MST element), but one state will cause the IDLS to be electrically invisible. In other words, the IDLS will have the capability to be modulated between an electrically visible and invisible state, thereby improving the MD. As such, incorporating the IDLS into MST may improve the overall robustness and practicality of this technique.

1.4. SUMMARY OF CHAPTERS

In order to thoroughly investigate the application of invisible antennas to MST, both simulations and measurements of MST scatterers were conducted. Electromagnetic simulations based on the Method of Moments (MM) were developed for the purposes of this analysis. Both the Numerical Electromagnetics Code (NEC) [22]-[23] and CST Microwave Studio® [24] were used to verify this simulation technique. The development and verification of the electromagnetic simulations is discussed in detail in Section 2. Section 3 presents simulations, performed with the developed MM code, of both single loaded electrically invisible scatterers (ISLS) as well as new invisible dual loaded scatterers (IDLS described above). Additionally, Section 3 also presents simulations of an

IDLS designed for fabrication on printed circuit boards. For comparison, simulations of a traditional MST scatterer (half-wave dipole loaded with a PIN diode) are also presented. In Section 4, measurements of the ISLS as well as the IDLS are presented and analyzed. The results of the new IDLS design are compared to measurements of a traditional MST scatterer in order to illustrate the improvement in performance (i.e., modulation depth) offered by this new approach. Concluding remarks and a discussion of future work is given in Section 5.

2. THEORY AND NUMERICAL METHODS

In order to investigate the potential improvement to the modulation depth (MD) of MST scatterers by designing one modulation state to be electrically invisible, electromagnetic (EM) simulations capable of simulating the current induced on, and the subsequent scattering of, linear scatterers loaded by multiple arbitrary impedances (i.e., loaded dipoles) were developed. Custom simulations were desired in order to gain a deeper understanding of the MST scatterer physics, and for simulation flexibility (e.g., ability to investigate different MST scatterer designs) and speed not easily attained by general (commercially available) EM solvers.

The custom developed EM simulations utilize the Method of Moments (MM) to solve Pocklington's Electric Field Integral Equation (EFIE) which has been simplified using thin-wire approximations [25]. For improved accuracy of practical wire diameters, an extended thin-wire approximation to the Pocklington EFIE kernel was utilized [26]. In addition, the Numerical Electromagnetics Code (NEC) [22]-[23] and CST Microwave Studio® [24] were used to verify the accuracy of this simulation technique. These comparisons are provided throughout the discussion of the MM simulation results provided in this Section.

2.1. POCKLINGTON'S ELECTRIC FIELD INTEGRAL EQUATION (EFIE)

Pocklington's EFIE can be used to calculate the current induced on a wire resulting from any arbitrary incident electric field [25]. Such a situation is illustrated in Figure 2.1, where a current, I_z, (represented by a filament of current at the wire axis) is induced on a wire of length, L, and radius, a, by an incident (plane wave) electric field, $\bar{E}^i$, which has an incident angle, θ^i, from normal. The induced current, I_z, results in a scattered electric field, $\bar{E}^s$, radiating away from the scatterer.

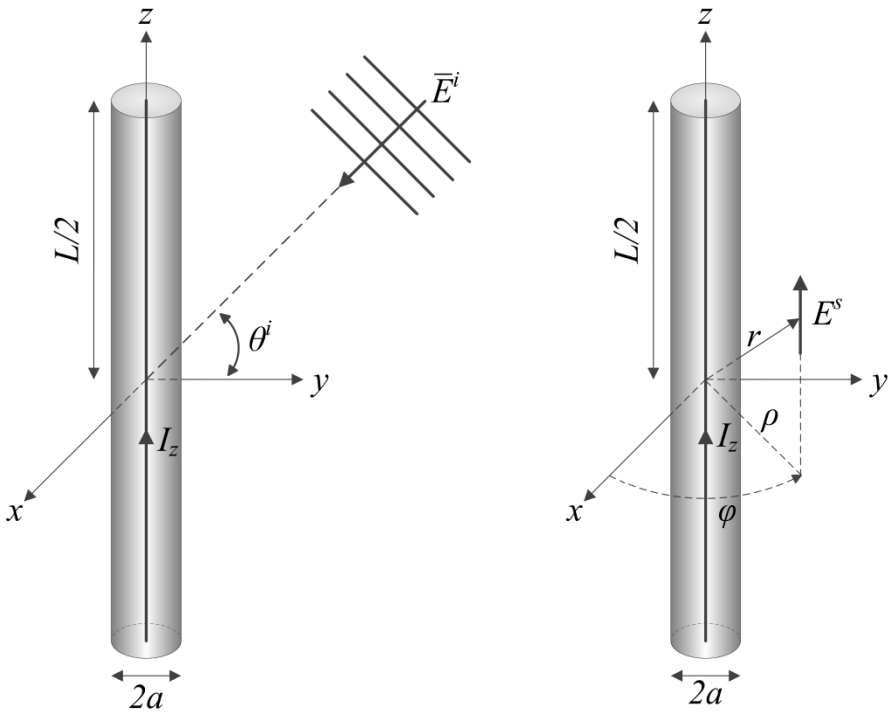

Figure 2.1. Geometry of a thin wire illuminated by an incident plane wave (a), and the scattering from the illuminated wire (b).

The derivation of Pocklington's EFIE begins by considering that the total electric field, $\bar{E}^t$, surrounding a scatterer is composed of both the incident, $\bar{E}^i$, and scattered, $\bar{E}^s$, field components:

$$\bar{E}^t(x,y,z) = \bar{E}^s(x,y,z) + \bar{E}^i(x,y,z) \tag{2}$$

where the fields are assumed to be time harmonic, meaning the fields have an $e^{j\omega t}$ time dependence, where ω is the frequency of the fields in radians per second. If the scatterer meets thin-wire conditions (e.g., $a \ll \lambda$, where λ is the wavelength in the medium surrounding the scatterer, and $a \ll L$), the transverse components of the induced current are negligible relative to the axial currents and the current can be represented by a filament on the wire axis, I_z [22]. In other words, if the wire is oriented along the z-axis

(as shown in Figure 2.1) and meets the thin-wire conditions, only the z-component, E_z^i, of the incident field is needed to determine the subsequent scattering since the currents induced by the transverse components of the incident field are negligible. Changing to cylindrical coordinates (see Figure 2.1) and applying perfect electrical conductor (PEC) boundary conditions at the surface of the wire ($\rho = a$) results in the following relation:

$$E_z^s(\rho = a) = -E_z^i(\rho = a) \tag{3}$$

Neglecting edge effects, and assuming k is the wave number and μ and ε are the permeability and permittivity respectively of the medium, the scattered field can be written as [25]:

$$E_z^s(r) = -j\frac{1}{\omega\mu\varepsilon}\left(\frac{\partial^2}{\partial z^2} + k^2\right)A_z(r) \tag{4}$$

In (4), the variable r (at the surface of the wire), when using the prime symbol to differentiate source points from observation points, is given by:

$$r(\rho = a) = \sqrt{4a^2\,sin^2\left(\frac{\varphi'}{2}\right) + (z - z')} \tag{5}$$

Also, in (4), A_z is the "magnetic vector potential" [25] and, is given by:

$$A_z(r) = \frac{\mu}{4\pi}\int_{-\frac{l}{2}}^{\frac{l}{2}}\int_0^{2\pi} J_z\frac{e^{-jkr}}{r}a\,d\varphi' dz' \tag{6}$$

where J_z is the current density induced on the wire by the incident field. Again assuming the scatterer meets thin-wire conditions; the circumferential variation in the axial current

may be neglected [22]. Therefore, the current density, J_z, may be assumed to be invariant with φ' and can be expressed as [25]:

$$J_z = \frac{1}{2\pi a} I_z(z') \tag{7}$$

For observation points at the surface of the wire ($\rho = a$), E_z^s can be interchanged for $-E_z^i$, as shown by (3), which, when combined with the above equations, results in Pocklington's EFIE:

$$-j\omega\varepsilon E_z^i(z) = \int_{-l/2}^{l/2} I_z(z') \left[\left(\frac{d^2}{dz^2} + k^2 \right) \frac{1}{2\pi} \int_0^{2\pi} \frac{e^{-jkr}}{4\pi r} d\varphi' \right] dz' \tag{8}$$

Equation (8) may now be solved, by numerical methods, for the current induced on a thin-wire scatterer given an incident field.

2.2. NUMERICAL METHODS

2.2.1. The Method of Moments. The Method of Moments, also known as the Moment Method, is a numerical method used to solve complex integral equations by expanding them into a system of linear equations that can be solved using matrix techniques. This technique has been used extensively in the area of thin-wire modeling [22], [25]-[30]. An overview of its application to the solution of Pocklington's equation (discussed above) is given next.

The MM solution starts by discretizing the scatterer into N, or $2M + 1$ (where M is an integer), segments of length Δ (where $\Delta = L/N$). This process is also known as "meshing." The induced current, I_z, is then described as a sum of basis (or expansion) functions, B, multiplied by coefficients, I_m [27]:

$$I_z(z') = \sum_{m=-M}^{M} I_m \, B(z' - z_m) \tag{9}$$

where z_m represents discrete source points defined by meshing the scatterer. Many different basis functions may be used in (9); a discussion of the basis functions used here follows later in this Section. This process results in the following changes to (8), which are shown below:

$$-j\omega\varepsilon E_z^i(z) = \sum_{m=-M}^{M} I_m \int_{-l/2}^{l/2} B(z'-z_m)\left[\left(\frac{d^2}{dz^2}+k^2\right)G(z-z')\right]dz' \tag{10}$$

Equation (10) has been simplified by substituting in $G(z-z')$, which is referred to as the Pocklington EFIE kernel:

$$G(z-z') = \frac{1}{2\pi}\int_0^{2\pi}\frac{e^{-jkr}}{4\pi r}d\varphi' \tag{11}$$

where r is given by (5). Weighting (or testing) functions are then applied to each side of the equation to form a weighted average around each discrete observation point, z_n [25]. It is important that these weighting functions be able to accurately approximate the distributions represented by each side of (10) [29]. *Dirac* delta functions were used as the weighting functions in this analysis for simplicity (no extra computation required) and generality (can be used to represent distributions of various shapes). This technique is also known as point-matching [27] and results in the modified equation shown below:

$$-j\omega\varepsilon\int_{-\frac{l}{2}}^{\frac{l}{2}} E_z^i(z)\delta(z-z_n)dz = \sum_{m=-M}^{M} I_m \int_{-l/2}^{l/2}\int_{-l/2}^{l/2} B(z'-z_m)\left(\frac{d^2}{dz^2}+k^2\right)G(z-z')\delta(z-z_n)dzdz' \tag{12}$$

which simplifies to:

$$-j\omega\varepsilon E_z^i(z_n) = \sum_{m=-M}^{M} I_m \int_{-l/2}^{l/2} B(z'-z_m)\left(\frac{d^2}{dz_n^2}+k^2\right)G(z_n-z')dz' \tag{13}$$

Pocklington's EFIE can now be written in matrix form and solved for the induced current [27] as shown below:

$$[I_m] = [Z_{mn}]^{-1}[V_n] \tag{14}$$

where

$$V_n = -j\omega\varepsilon E_z^i(z_n) \tag{15}$$

and

$$Z_{mn} = \int_{-l/2}^{l/2} B(z'-z_m)\left(\frac{d^2}{dz_n^2}+k^2\right)G(z_n-z')dz' \tag{16}$$

Solving (14) for the current induced on the scatterer is easily accomplished with matrix routines available in today's mathematical computation software (e.g., MATLAB® [31]). However, the calculation of the $[Z_{mn}]$ matrix is non-trivial since it involves an integration of the kernel, differential operator and current basis functions, each of which are discussed in turn below.

2.2.2. Pocklington EFIE Kernel Calculation. In order to evaluate the kernel numerically and avoid the singularity at $z = 0$ found in (11), often the current is approximated to be an infinitely thin filament of current located on the wire axis which is valid if the thin-wire conditions are met [22]. As discussed above, in this case, the current has no φ dependence. This can be used to simplify the kernel from (11) to (17); which is known as the "thin-wire kernel" (G_o).

$$G_o(r_o) = \frac{e^{-jkr_o}}{4\pi r_o} \tag{17}$$

Likewise r can be simplified to r_o (at the surface of the wire), as shown below:

$$r_o(\rho = a) = \sqrt{a^2 + (z - z')} \tag{18}$$

In [26], Poggio and Adams further analyze this approximation and give criteria for its use. In order for the approximate thin-wire kernel to remain within 1% of the exact kernel, the mesh segment length must be greater than 10 times the scatterer radius [26].

$$\Delta/a > 10 \tag{19}$$

This provides a limit for how fine the scatterer may be meshed. That is to say, the number of segments, N, is limited by the relationship shown below:

$$N < l/10a \tag{20}$$

For thicker wires, additional accuracy may be desired and possibly required if the inequality in (20) does not allow enough segments for solution convergence. An "Extended Thin-Wire Kernel" (21) was derived in [26] for this purpose. This kernel is valid when thin-wire conditions are met except the current is now considered as a sheet of current dispersed around the circumference of the wire instead of a filament of current at the scatterer center [26].

$$G_e(r_o) = \frac{e^{-jkr_o}}{4\pi r_o}\left\{1 - \frac{1+jkr_o}{2\left(\frac{r_o}{a}\right)^2} + \frac{1}{4\left(\frac{r_o}{a}\right)^4}[3jkr_o + 3 - (kr_o)^2]\right\} \tag{21}$$

In order for this approximation to remain within 1% error from the exact value, the mesh segment length must be greater than twice the wire radius, as shown by (22).

$$\Delta/a > 2 \tag{22}$$

This allows for a finer mesh (more segments) while maintaining the accuracy of the calculated kernel, which is desirable because a finer mesh may at times be needed for solution convergence. If the above criteria (22) cannot be met, a more precise calculation of the kernel must be utilized [26]. However, for the purposes of this analysis, the extended thin-wire kernel was sufficient.

2.2.3. The Differential Operator. In order to evaluate Pocklington's EFIE numerically, the differential operator (23) must be applied, as shown in (8).

$$\left(\frac{d^2}{dz^2} + k^2\right) \tag{23}$$

Different methods have been employed to accomplish this part of the numerical calculation. In [27], the operator is moved outside the integral in (16) and applied numerically via a first order finite difference (FD) once the kernel and basis functions are integrated. Early versions of the MM simulations developed for this work also employed this method until a thorough analysis of its accuracy was performed.

The analytical solution for the application of the differential operator applied directly to the thin-wire kernel is given by Thiele in [30] and is shown in (24).

$$\left(\frac{d^2}{dz^2} + k^2\right) G_o(r_o) = \frac{e^{-jkr_o}}{4\pi r_o^5}[(1+jkr_o)(2r_o^2 - 3a^2) + (kar_o)^2] \tag{24}$$

No such analytical method was provided for the extended thin-wire kernel, which made the FD method appear more suitable. However, in an attempt to improve the accuracy of the simulations, it was decided to test the accuracy of the numerical method (i.e., FD) against this analytical expression.

This comparison evaluated the differential operator applied to the kernel using (24) and via the numerical method. The numerical method was a first order finite difference that was based on that developed in [27]. For the purposes of the evaluation, a half-wave scatterer of radius 0.0017λ was considered. The scatterer was meshed into 51 segments. The result of this comparison (differential operator applied to the kernel using the two methods) is shown by Figure 2.2 below.

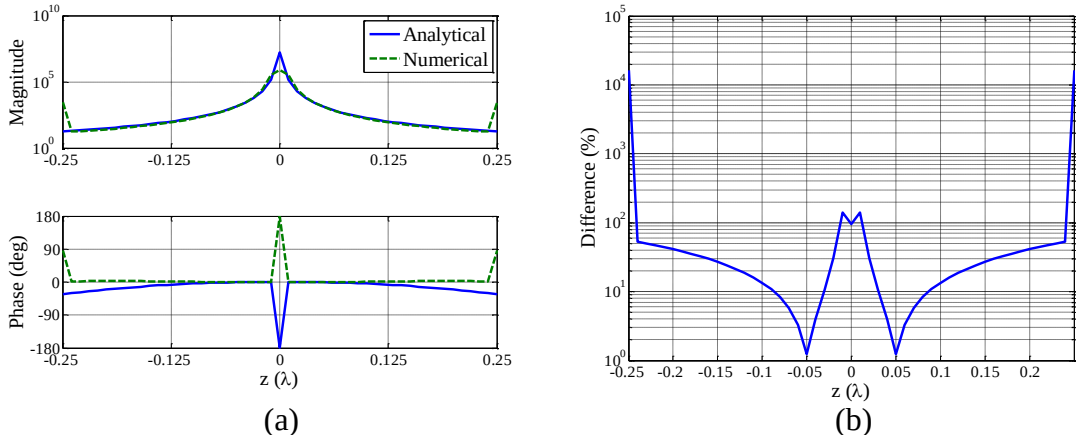

(a) (b)

Figure 2.2. Application of the Differential Operator to the Thin-Wire Kernel: (a) analytical vs. numerical, (b) percent difference.

The results in Figure 2.2 indicate significant error in the numerical method when compared to the analytical expression (24). As such, the same comparison was performed for the extended thin-wire kernel. This required an analytical solution for the application of the differential operator to extended thin-wire kernel be derived. In order to accomplish this, the computational tool *Mathematica*® [32] was used to apply the differential operator to the extended thin-wire kernel as well as simplify the equation symbolically, which is given below (25).

$$\left(\frac{d^2}{dz^2}+k^2\right)G_e(r_o)$$

$$=\frac{e^{-jkr}}{16\pi r_o^9}\langle 8r_o^6(1+jkr_o)+12a^2r_o^4[-3+kr_o(-3j+kr_o)] \quad (25)$$
$$+8a^4r_o^2\{15+kr_o[15j+kr_o(-6-jkr_o)]\}$$
$$-\ a^6(105+kr_o\{105j+kr_o[-45+kr_o(-10j+kr_o)]\})\rangle$$

Once the analytical expression, (25), had been developed, a similar comparison (analytical vs. numerical evaluation of the differential operator applied to the extended thin-wire kernel) was performed with the results shown below in Figure 2.3.

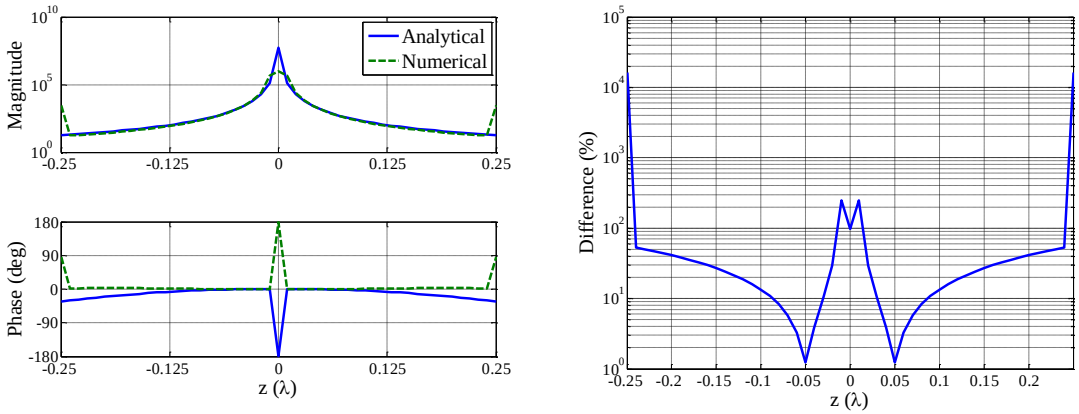

(a) (b)

Figure 2.3. Application of the Differential Operator to the Extended Thin-Wire Kernel: (a) analytical vs. numerical, (b) percent difference.

The results of the comparison, shown in Figure 2.3, are similar to those of the thin-wire kernel shown above. In other words, the numerical method results deviate significantly from the analytical results given by (25). However, the accuracy of the finite difference method will increase with increased sample points; therefore, the comparison was re-done but with 501 segments (e.g., increased meshing of the scatterer). The results of the comparison are shown below in Figure 2.4 and Figure 2.5.

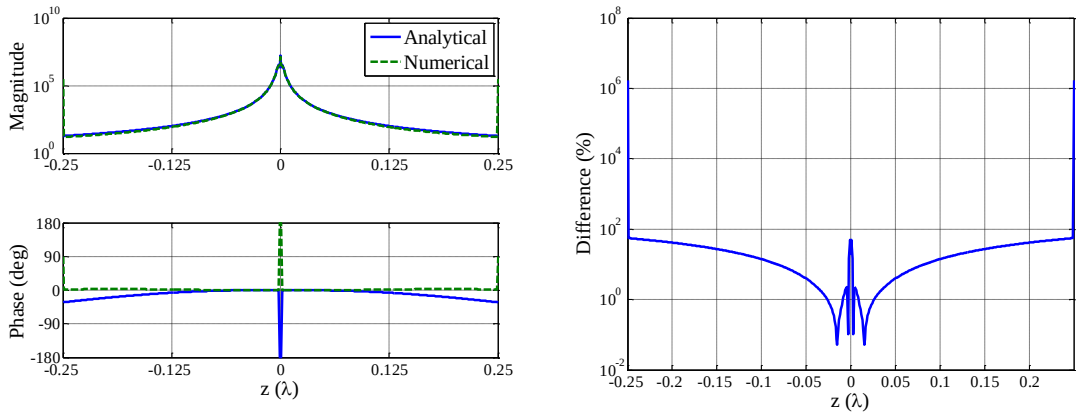

(a) (b)

Figure 2.4. Application of the Differential Operator to the Thin-Wire Kernel (501 Segments): (a) analytical vs. numerical, (b) percent difference.

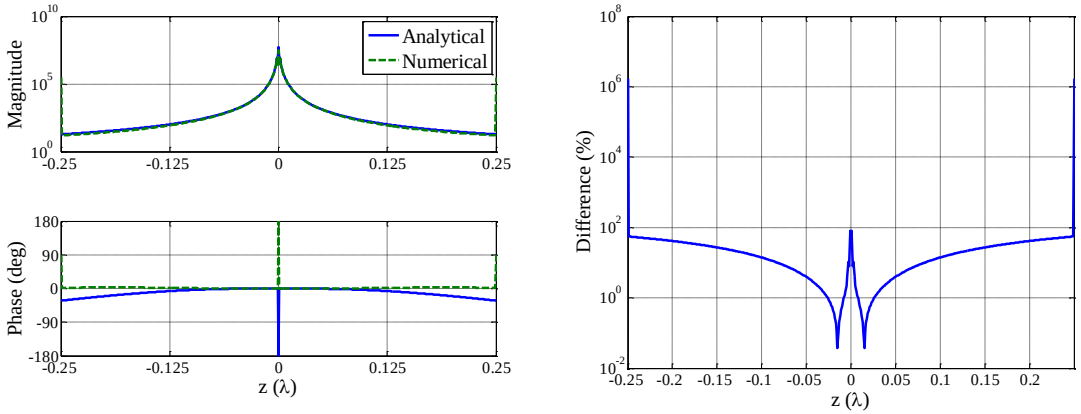

(a) (b)

Figure 2.5. Application of the Differential Operator to the Extended Thin-Wire Kernel (501 Segments): (a) analytical vs. numerical, (b) percent difference.

It is evident from Figure 2.4 and Figure 2.5 (comparing to the results of Figure 2.3 and Figure 2.2) that the accuracy of the finite difference method improves with increased data points (mesh segments); however, it should be noted here that 501 mesh results in a Δ/a ratio of 0.588, which according to (19) and (22) indicates the accuracy of both kernel approximations are no longer within 1% of the exact kernel value [26]. These results indicated the finite difference method employed by the simulations needed to be replaced.

More detailed numerical methods may have been implemented, however, since exact analytical expressions have been developed, such methods are unnecessary. As such, the simulations were updated to include the analytical expressions for applying the differential operator to the kernel in Pocklington's EFIE, thereby removing the error in the solution introduced by the numerical method (i.e., finite difference). The last aspect of the numerical solution to Pocklington's EFIE that is worthy of discussion is the current basis functions, which are discussed next.

2.2.4. Current Basis Functions. Properly selected basis functions must maintain the ability to accurately represent the function for which they are being used to model [25]. In the case of these simulations, the unknown function is the distribution of current induced along a wire scatterer by an incident field, which may be modeled using many different types of basis functions. All possible basis functions that could be utilized for this application fall into two main categories: entire domain basis functions, and subdomain basis functions. Entire domain basis functions (e.g., Fourier series) are non-zero over the entire calculation domain which requires the shape of the current distribution being calculated to be *a priori* known [25]. Hence, as the shape of the induced current is unknown, entire domain basis functions were not utilized in the MM simulations.

Subdomain basis functions (or piecewise basis functions) have the ability to model more arbitrary and complex functions since they are only defined (non-zero) over a sub section of the calculation domain and hence do not require *a priori* knowledge of the function being modeled [25]. As such, subdomain basis functions were used in these simulations. Many different types of subdomain basis functions exist; however, only pulse and triangle subdomain basis functions were implemented for this work, each of which are discussed below.

Pulse basis functions are the simplest to implement of all the subdomain basis functions. Also, due to their simplicity, they may have computational advantages. They produce a step approximation to the current distribution with no interpolation between sample points (mesh segments) which is illustrated in Figure 2.6.

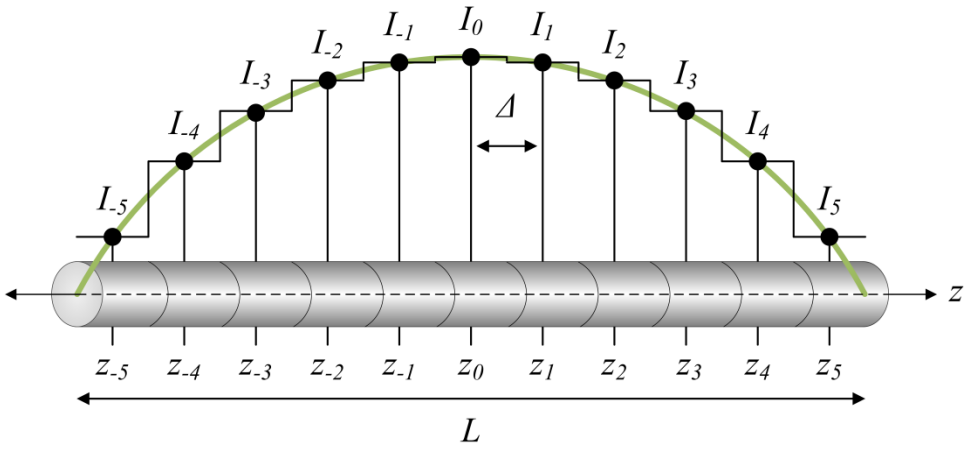

Figure 2.6. Pulse basis functions.

However, while pulse basis functions are simple to implement, the lack of interpolation between sample points may limit accuracy. The equation used to define the pulses over each segment is given below:

$$B_{pulse}(z' - z_m) = \begin{cases} 1\,, & if\ |z' - z_m| \leq \Delta/2 \\ 0\,, & otherwise \end{cases} \tag{26}$$

The calculation of the Z_{mn} terms in (16) then reduces to:

$$Z_{mn} = \int_{z_m - \Delta/2}^{z_m + \Delta/2} K(z_n - z')dz' \tag{27}$$

where K is used to represent the kernel term after the differential operator has been applied analytically as discussed above. As can be seen from (27), the effect of the basis function was to merely change the limits of integration to include only the individual segment of the scatterer. The developed simulations then use a change of integration variable ($\hat{z}$ is integrated over the length of the segment) [27] to further simplify the calculation:

$$Z_{mn} = \int_{-\Delta/2}^{\Delta/2} K(z_n - z_m - \hat{z})d\hat{z} \tag{28}$$

With the ability to calculate the Z_{mn} terms using (28), the number of segments needed for solution convergence (in order to accurately calculate the induced current) was investigated.

The current distribution on a λ/2 scatterer, with a wire radius of 0.0021λ, was modeled with pulse basis functions for various mesh sizes (i.e., number of segments), the results of which are shown in Figure 2.7. The simulated excitation was a normally incident plane wave of unity magnitude and uniform phase, with the polarization of the electric field aligned with the axis of the scatterer.

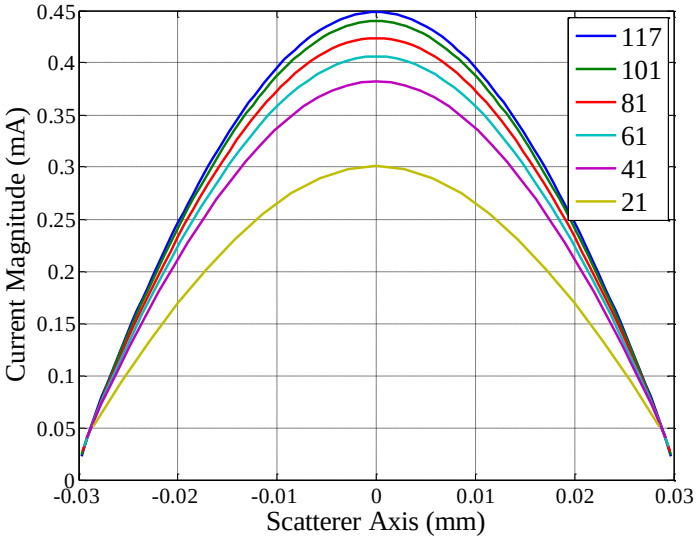

Figure 2.7. Magnitude of induced current for different number of segments utilizing pulse basis functions (i.e., convergence test for pulse basis functions).

It is evident from Figure 2.7 that convergence of the current is achieved by using more than 100 segments; however, for the scatterer geometry simulated, the accuracy of the extended thin-wire kernel degrades beyond 1% when using more than 117 mesh

segments. Further, it should be noted that the current shown in Figure 2.7 only approaches zero (but does not equal zero) at the ends of the scatterer due to the approximation of the basis functions, i.e., the current is sampled in the center of the discrete segment (shown in Figure 2.7), and not at the wire ends, as shown in Figure 2.8. In an effort to achieve improved accuracy and faster convergence (i.e., less mesh segments), triangle basis functions were also considered.

Triangle basis functions require the scatterer be discretized into one less segment than pulse basis function with the sample points defined at the ends of the segments as illustrated in Figure 2.8.

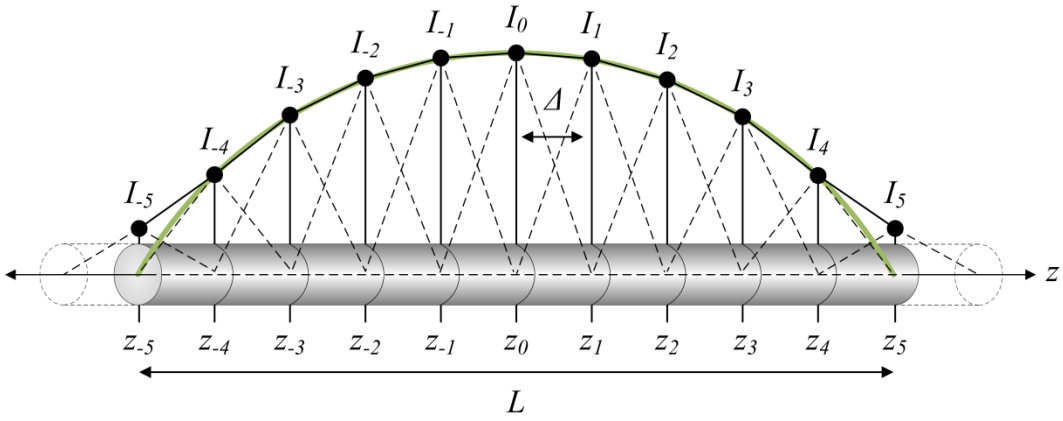

Figure 2.8. Triangle basis functions.

From Figure 2.8, it can be seen that triangle basis functions result in a linear interpolation between segments, as the current is integrated along the length of the wire in (13). This can increase the accuracy of the solution when compared to pulse basis functions [25]. The triangle basis functions for each source point, z_m, are defined by the equation below:

$$B_{tri}(z' - z_m) = \begin{cases} 1 - \dfrac{|z' - z_m|}{\Delta}, & if\ |z' - z_m| \le \Delta \\ 0, & otherwise \end{cases} \tag{29}$$

This results in the following calculation of the Z_{mn} terms:

$$Z_{mn} = \int_{-\Delta}^{\Delta} \left(1 - \frac{|\hat{z}|}{\Delta}\right) K(z_n - z_m - \hat{z}) d\hat{z} \tag{30}$$

According to [25], the accuracy of this method (i.e. triangle basis functions) degrades when choosing observation points, z_n, along the wire that corespond to the peaks of the triangles (i.e., non-differentiable points), z_m. In an effort to avoid this problem, the observation points are slightly shfted from coresponding source points, exept for the center ($z = 0$) point, during meshing. Using a mesh of different sizes (number of segments) and triangle basis functions, the current distribution on a λ/2 dipole scatterer, with a wire radius of 0.0021λ, was simulated and is shown in Figure 2.9.

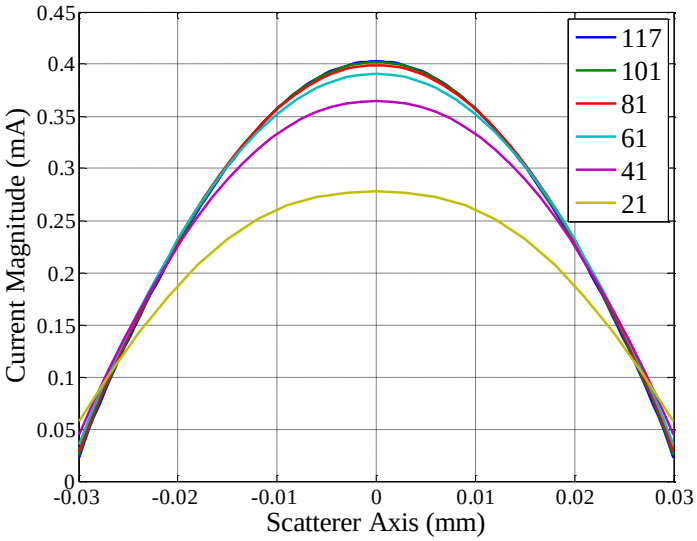

Figure 2.9. Magnitude of induced current for different number of segments utilizing triangle basis functions (i.e., convergence test for triangle basis functions)

From Figure 2.9, it is evident that the current distribution converges faster than the pulse basis functions, requiring only approximately 81 mesh segments to converge. This is desirable since not only do fewer segments require less computational resources (e.g.,

memory) which result in faster simulations, but fewer segments also means a smaller Δ/a ratio which may prevent degradation of approximate kernel accuracy, as discussed above. Similar to the case of pulse basis functions, the induced current only approaches zero, but does not equal zero, at the ends of the scatterer. This is due to the definition of triangle basis functions which causes the integration of "fictitious" end segments by (30) as shown in Figure 2.8.

As mentioned previously, calculating the current basis functions was the last step in solving for the terms of the $[Z_{nm}]$ matrix. With these terms now solvable by either (28) or (30), Pocklington's EFIE can now be solved for the current distribution $[I_m]$ as shown in (14). This was displayed in the current convergence tests which were shown in Figure 2.7 and Figure 2.9. In order to investigate the accuracy of the calculated current distribution (after convergence), this technique was verified against results from the NEC.

The current induced on a λ/2 shorted dipole illuminated by a 1 V/m incident plane wave was simulated by the NEC as well as the developed MM simulation, utilizing triangle basis functions. The results are compared below in Figure 2.10. Figure 2.10 shows very close agreement between the two simulations which indicates the developed simulations can reliably calculate the current induced on a scatterer by an incident field. However, since the goal of this work is to investigate loaded scatterers, the input impedance of the scatterer at the location of the load (e.g., a PIN diode at the center of a traditional MST scatterer) must also be known. Now that Pocklington's EFIE can be accurately solved in order to determine the induced current distribution, the input impedance may be calculated using the method discussed next.

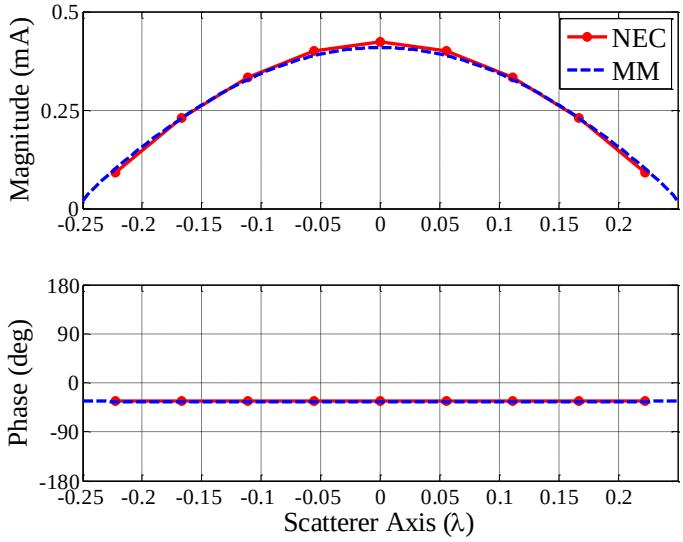

Figure 2.10. Comparison of current distribution on shorted dipole.

2.2.5. Input Impedance Calculation. The input impedance of the scatterer, at the segment(s) containing a load, is calculated by applying an ideal -1V (negative used here due to the current reference direction shown by Figure 2.1) source at a fictitious port at the same location on the scatterer. The source was modeled using the magnetic frill technique [33], which can be used to represent a voltage source on a wire as an equivalent (effective) impressed electric field at the axis of the wire ($\rho = 0$). The effective impressed electric field along the antenna produced by the -1 V source is given by the equation below:

$$E_z(z - z') = \frac{-1}{2 * ln(a/b)}\left[\frac{e^{-jkr_a}}{r_a} - \frac{e^{-jkr_b}}{r_b}\right] \tag{31}$$

where, r_a and r_b are given by (32) and (33) respectively and $b = 2.3a$ [25].

$$r_a = \sqrt{a^2 + (z - z')^2} \tag{32}$$

$$r_b = \sqrt{b^2 + (z - z')^2} \tag{33}$$

Once calculated by (31), the effective electric field can be used in conjunction with Pocklington's EFIE which can then be solved for the current distribution by the developed MM technique (discussed above). The input impedance is calculated from the subsequent current (calculated) at the port. It is important to ensure enough segments were utilized in the simulation for the current calculation to converge or the calculated input impedance may be inaccurate.

The developed MM simulations employ an adaptive meshing routine which systematically refines the mesh until solution convergence is achieved. The simulation monitors the Δ/a ratio to ensure the accuracy of the employed kernel (thin-wire or extended thin-wire) is not degraded beyond 1% (as discussed above). Solution convergence is determined by checking the variation of the calculated scatterer input impedance over the last five iterations of the solver (34), hence a minimum of five mesh refinements are required. The simulations calculate the "*% error*" using the equation below:

$$\%\ error = \left| \frac{std(\bar{Z})}{|avg(\bar{Z})|} \right| \tag{34}$$

where $\bar{Z}$ is a vector containing the last five calculations of the complex input impedance, as the mesh was refined. As a result of convergence testing, it was determined that this percent error should be near 1% for simulations to converge to results with good accuracy.

Using this technique, the convergence of the calculated input impedance at the center of a λ/2 dipole scatterer, with a wire radius of 0.0021λ, was investigated for each basis function type (pulse and triangle). Even though triangle basis functions were already shown above to converge faster than pulse basis functions, it was still necessary to compare the accuracy of the input impedance calculated with the two basis functions. The results are shown below in Figure 2.11 as a function of the number of mesh segments.

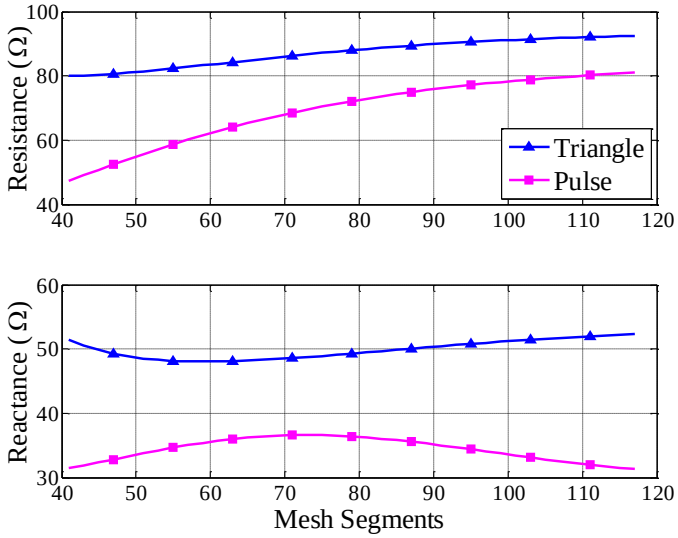

Figure 2.11. Convergence of input impedance calculation.

From Figure 2.11, it is evident that the reactive part of the input impedance does not seem to converge to the same value for both basis functions. This is not unexpected since, in general, it is difficult to use numerical methods to accurately calculate the reactive part of the input impedance [27]. However, from the results of Figure 2.11, triangle basis functions produce a more stable result as the value of the reactive part does not vary as widely as that calculated with pulse basis functions. The convergence of the calculated input impedance, of different wire sizes, for each basis function is investigated next. Figure 2.12 shows the number of mesh segments required for convergence of the calculated input impedance of a λ/2 dipole as a function of wire diameter for each basis function. For this test, the percent error (34) threshold was set to 2% for the result to be considered converged. As can be seen from Figure 2.12, the triangle basis functions require fewer segments to converge. This is consistent with the analysis of the current convergence shown in Figure 2.7 and Figure 2.9, which when combined with the advantages of the triangle basis functions when used to calculate the input impedance, confirms that the triangle basis functions are more accurate than the pulse basis functions. Therefore, triangle basis functions are used in all subsequent simulations discussed herein. The input impedance calculation of the developed MM technique (using triangle basis functions) was then compared with other EM solvers for verification.

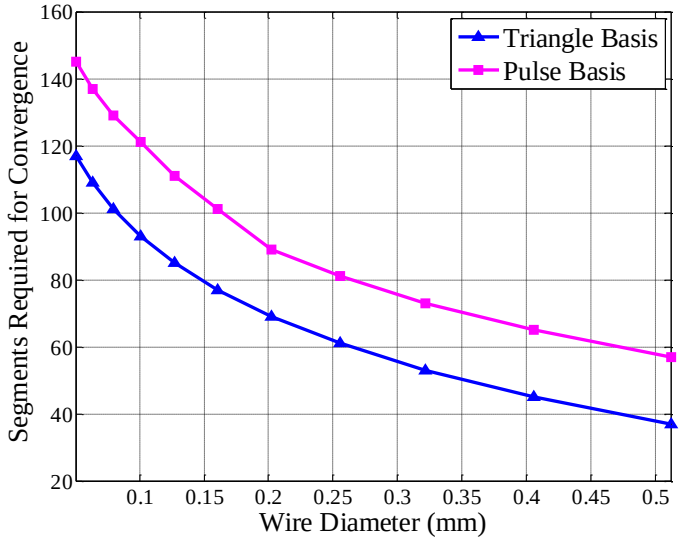

Figure 2.12. Segments required for convergence of the input impedance.

The input impedance of a dipole scatterer, calculated at the center, was compared to that calculated by NEC and CST for a variety of dipole geometries, i.e., length and diameter. Figure 2.13a compares the calculated input impedance as a function of dipole length with a fixed wire radius of 0.0017λ and Figure 2.13b compares the calculated input impedance as a function of wire radius with a fixed length of λ/2.

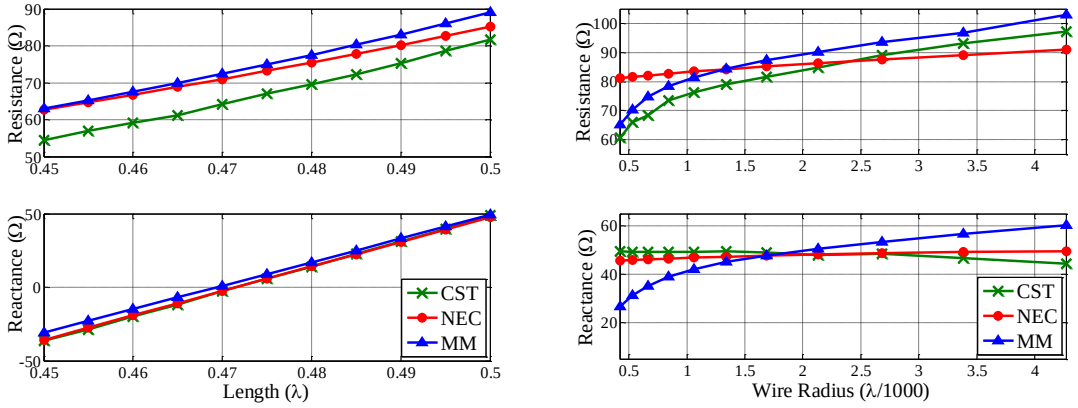

(a) (b)

Figure 2.13. Input impedance as a function of: (a) scatterer length, (b) wire radius.

As shown by Figure 2.13, the developed MM simulations compare well to the other EM solvers. The variations between the methods are not considered significant and are attributed to differences in the numerical methods utilized. The results show the different techniques have the best correlation for wires of radius 0.0017λ and 0.0021λ. With the ability to calculate both induced current as well as the input impedance, the simulations can now be adapted to account for loads on the scatterer (e.g., MST scatterers).

2.2.6. Simulating a Loaded Scatterer. In order to simulate the effects of loads on the current distribution and subsequent scattering of a loaded scatterer, network theory was utilized [28]. The theory and subsequent developed simulations can account for an arbitrary number of loads placed on the scatter; however, for simplicity this discussion considers a scatterer with two loads (similar to the DLS shown in Figure 1.1).

From [28], a system consisting of an arbitrarily loaded scatterer and transmit and receive antennas can be characterized by the following network equations:

$$\begin{bmatrix} \Delta I_r \\ \Delta I_t \\ [I_s] \end{bmatrix} = \begin{bmatrix} \Delta Y_{rr} & \Delta Y_{rt} & [Y_{rs}] \\ \Delta Y_{tr} & \Delta Y_{tt} & [Y_{ts}] \\ [Y_{sr}] & [Y_{st}] & [Y_{ss}] \end{bmatrix} \begin{bmatrix} V_r \\ V_t \\ [V_s] \end{bmatrix} \tag{35}$$

where Δ indicates a change in the mutual coupling between transmit and receive antennas (denoted by the subscripts t and r respectively) due to the presence of the loaded scatterer (denoted by the subscript s). The current and voltages at the ports are denoted, along with the appropriate subscripts, by I and V respectively. Additionally, the admittance parameters given in (35) describe the interaction between the ports (the subscripts are used to denote which ports) of the entire system. For example, $[Y_{st}]$ (equivalent to $[Y_{ts}]$ if the media is reciprocal as is the case here) describes the interaction between the transmit antenna port and each port (one for each load) on the scatterer. Such a system is shown below in Figure 2.14, where the scatterer is loaded with two arbitrary admittances, Y_1 and Y_2.

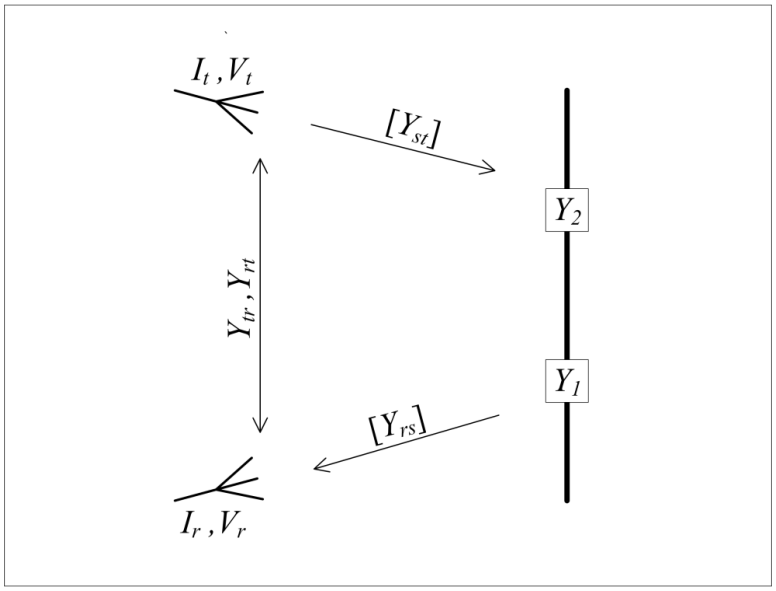

Figure 2.14. Loaded scatterer network diagram.

In (35), $[Y_{ss}]$ is the self-admittance matrix of the scatterer and is calculated from the definition of Y-parameters (admittance parameters) [34]. The diagonal terms (i.e., Y_{11} and Y_{22}) are the input admittances which are calculated using the same technique as that used for the input impedance described above. When the scatterer is loaded with more than one load, the input admittance of a given port is calculated while considering all other loads as shorts. The self-admittance matrix for the scatterer shown in Figure 2.14 is given by:

$$[Y_{ss}] = \begin{bmatrix} Y_{11} & Y_{12} \\ Y_{21} & Y_{22} \end{bmatrix} \tag{36}$$

Also from the definition of Y-parameters [34], the vector $[Y_{st}]$ is calculated for the two load case as:

$$[Y_{st}] = \begin{bmatrix} I_1/V_t \Big|_{V_1=V_2=0} \\ I_2/V_t \Big|_{V_2=V_1=0} \end{bmatrix} \tag{37}$$

where I_1 and I_2 are calculated by the current induced on an unloaded scatterer by the incident electric field, since an unloaded scatterer is the same as shorting ports 1 and 2 (i.e., $V_1 = V_2 = 0$).

In [28], the receive antenna is assumed to be short circuited ($V_t = 0$) for simplicity. This assumption can also be made for small scatterers (e.g., MST scatterers), since the received signal is small. Also, the constraints at the load terminals [28], given by (38), can be used to remove the currents on the scatterer, $[I_s]$, from the system of equations (35).

$$[I_s] = -[Y_L][V_s] \tag{38}$$

In (38), $[V_s]$ represents the voltages at the loads (a negative sign is used due to the current reference direction shown in Figure 2.1) and $[Y_L]$ is the admittance matrix of the loads, which for the case shown in Figure 2.14 is given by:

$$[Y_L] = \begin{bmatrix} Y_1 & 0 \\ 0 & Y_2 \end{bmatrix} \tag{39}$$

The application of these simplifications to (35) results in the new system of equations shown below:

$$\begin{bmatrix} \Delta I_r \\ \Delta I_t \\ 0 \end{bmatrix} = \begin{bmatrix} \Delta Y_{rr} & \Delta Y_{rt} & [Y_{rs}] \\ \Delta Y_{tr} & \Delta Y_{tt} & [Y_{ts}] \\ [Y_{sr}] & [Y_{st}] & [Y_{ss}] + [Y_L] \end{bmatrix} \begin{bmatrix} 0 \\ V_t \\ [V_s] \end{bmatrix} \tag{40}$$

Setting V_t to unity and solving for $[V_s]$ from (40) yields the equation for the voltages at the loads shown below.

$$[V_s] = -([Y_{ss}] + [Y_L])^{-1}[Y_{st}] \tag{41}$$

The actual value of V_t is arbitrary since, due to (37), the desired equation for $[V_s]$ is ultimately independent of this parameter; therefore, V_t is set to unity for simplicity.

Once the voltages induced at the loads, $[V_s]$, are determined, the magnetic frill and MM solver can be used to calculate the current distribution along the scatterer excited by each voltage independently. The total current induced on the loaded scatterer is determined by the superposition of the induced current on an unloaded scatterer and the currents excited by the voltages (representing each load) at the load locations. In order to verify the accuracy of this technique, the induced current distribution of a centrally loaded, half-wave dipole scatterer (illuminated by an incident plane wave) was simulated both by the NEC as well as by the developed MM simulations. Both a very high resistive load of 1^{10} Ω (simulating an open circuit) and a reactive load of 764j Ω (chosen for comparison to simulations discussed in the next Section) were considered. The results of this comparison are shown below in Figure 2.15.

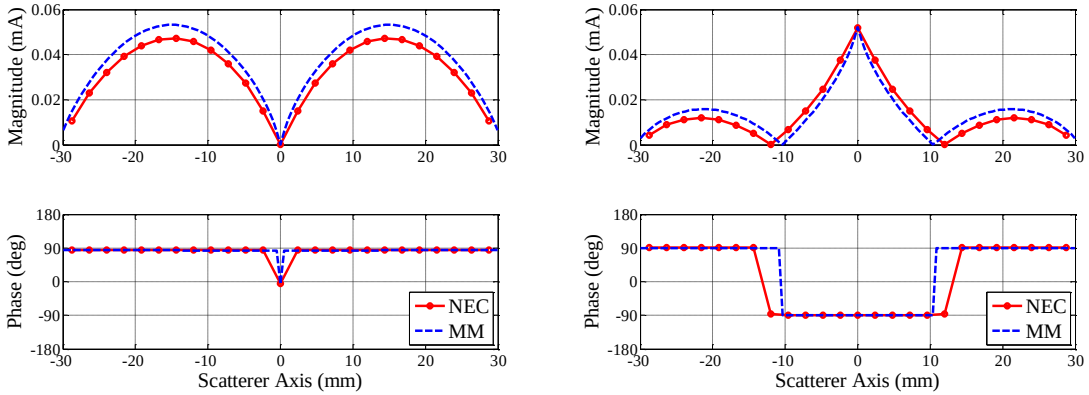

Figure 2.15. Comparison of induced current distribution on centrally loaded half-wave dipole scatterer: (a) open circuit, (b) reactive load.

As can be seen in Figure 2.15, close agreement is achieved between the results obtained with the developed MM simulations and those of the NEC. Overall, the developed MM technique has been shown to reliably simulate the current distribution induced on a loaded scatterer by an incident field; therefore, the subsequent scattered fields radiated by the current distribution can be calculated.

2.2.7. Scattering Calculation. Once the total current distribution along the simulated loaded scatterer has been determined, the scattered field at any point away from the scatterer can be calculated using the following equation (42) from [35]:

$$E_z^s(\rho, z) = \frac{j\eta}{4\pi k} \int_{-l/2}^{l/2} I_z(z')[G_1 + G_2(z - z')^2]e^{-jkr} dz' \tag{42}$$

where

$$G_1 = \frac{-1 - jkr + (kr)^2}{r^3} \tag{43}$$

$$G_2 = \frac{3(1 + jkr) - (kr)^2}{r^5} \tag{44}$$

and

$$r = \sqrt{\rho^2 + (z - z')^2} \tag{45}$$

This equation was derived assuming the source is a very thin line current. In the limit, as $a \to 0$, the current density equals the current ($J_z = I_z$), hence the calculated current is used in (42). Also, note that since the current distribution has been assumed to have no variation in φ due to thin-wire approximations, the scattered electric field is also φ independent (i.e., the scattered field is omnidirectional).

In order to verify this calculation technique for the scattered fields, a λ/2 unloaded scatterer (i.e., a shorted dipole) illuminated by a 1 V/m incident plane wave was simulated. The resulting broadside scattered field at 3 m, calculated by the developed

MM simulations, is verified against the results of the NEC. The results of the two simulations are shown in Figure 2.16.

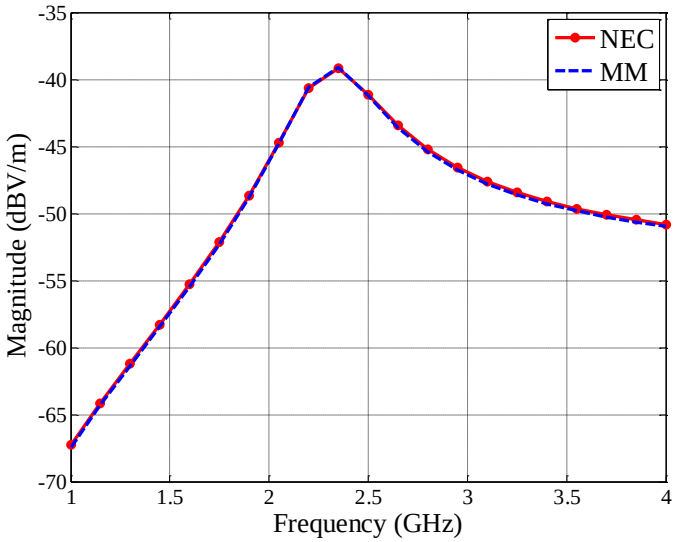

Figure 2.16. Comparison of calculated scattering from short circuited dipole.

From Figure 2.16, it is evident that the technique employed by the developed MM simulations results in calculated scattering that corresponds with that calculated by the NEC. This gives confidence in the ability of the MM simulations to accurately simulate the scattering from an arbitrarily loaded scatterer.

2.3. SUMMARY

This Section detailed the theory and techniques utilized in the development of electromagnetic simulations, based on the Method-of-Moments, for the purpose of investigating the behavior of MST scatterers, i.e., loaded dipole antennas. These simulations calculate the current distribution induced on a loaded scatterer by an incident electric field. Once the induced current distribution has been determined, the subsequent scattered fields can be calculated. These simulations were checked against other EM simulation software packages (Numerical Electromagnetics Code (NEC) [22]-[23] and CST Microwave Studio® [24]) and showed to be in good agreement. Using these

developed simulations, the current distributions and subsequent scattered fields of single and dual loaded MST scatterers are investigated in the next Section. The developed simulation code (implemented in MATLAB® [31]) is provided in the Appendices.

3. SIMULATIONS

In this Section, the electromagnetic simulations developed in Section 2 are used to simulate the distribution of current, induced by an electromagnetic wave incident on dipole scatterers with various loads. In particular, the effects of inductive (reactive) loading, which, when chosen properly, can cause the integral of the induced current distribution along the length of the scatterer to vanish [14], are studied. The subsequent scattering from such a reactively-loaded scatterer, referred to herein as an invisible single loaded scatterer (ISLS), is also calculated and analyzed. Additionally, simulations of new MST scatterers, based on the dual loaded scatterer (DLS) design (discussed in Section 1) [6]-[7], are provided. These new scatterers have been designed to be electrically invisible during one modulation state in order to increase the modulation depth (MD) of their scattering. In addition, the performance (i.e., MD), of these new scatterers, herein referred to as invisible dual loaded scatterers (IDLS), is compared to a traditional MST scatterer (a half-wave dipole centrally loaded with a PIN diode) to illustrate the improvement offered by this new approach. With the concept of the new IDLS successfully shown for the case of a wire-based IDLS, CST Microwave Studio® (CST MWS) [24] is used to simulate the performance of an IDLS fabricated on a printed circuit board (PCB). This PCB-based IDLS was also investigated since scatterers implemented on a PCB may offer practical benefits (e.g., manufacturing flexibility, etc.).

3.1. ELECTRICALLY INVISIBLE SINGLE LOADED SCATTERER (ISLS)

Initially, in order to fully understand the application of electrically invisible antennas to MST, a centrally-loaded dipole, herein referred to as a single-loaded scatterer (SLS), was studied. The SLS is illustrated below in Figure 3.1.

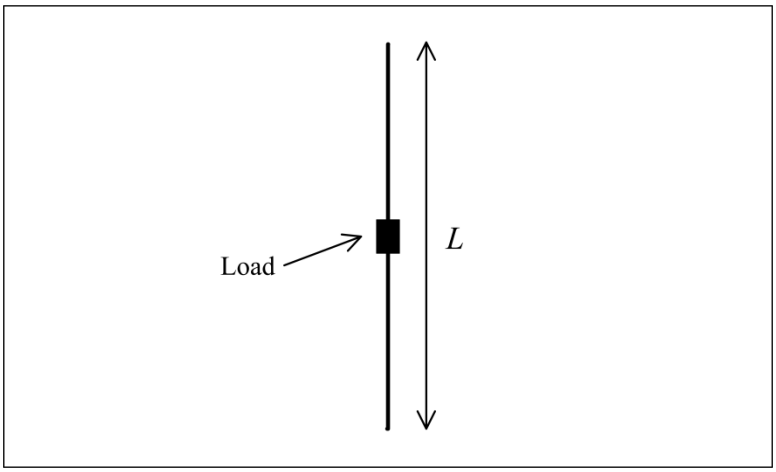

Figure 3.1. Schematic of a Single Loaded Scatterer (SLS).

According to [14], zero scattering (i.e. electrical invisibility) is achieved by loading an SLS (Figure 3.1) with an inductive reactance. This causes a 180° phase shift in the current induced on the scatterer in the vicinity of the load. When this reactance is chosen properly, the resulting phase shift causes the integral of the current induced along the SLS to vanish [14], thereby minimizing the scattering of the SLS and achieving electrical invisibility [16]. Such a scatterer is herein referred to as an invisible SLS, or ISLS.

3.1.1. ISLS Design. Using the developed simulations (discussed in Section 2), various inductive loads were considered in order to determine the optimal load for electrical invisibility of an SLS (see Figure 3.1) with a length (L) of 60 mm ($\lambda/2$ at 2.5 GHz) and diameter of 0.511 mm (24 AWG). The particular wire size of 24 AWG was chosen because it provides a good balance between practical usability (e.g., mechanical strength) and dimensions for the thin-wire approximation employed by the simulations (as mentioned in Section 2). A design frequency of 2.5 GHz was chosen for correlation to measurements discussed in Section 4. The simulated excitation of the scatterer was a normally-incident plane wave (i.e., broadside illumination) of unity magnitude, polarized along the length of the scatterer. Additionally, due to the thin wire approximations employed by the simulations (discussed in Section 2), the simulated scattering is symmetric about the dipole (i.e., the scattering is omnidirectional). All subsequent simulations also use this basic scatterer geometry (wire length and diameter) and excitation. Additionally, all scattering simulations presented herein consider broadside

scattering, E_s, at a distance of 1.5 m (far-field region) from the scatterer. Figure 3.2 shows the resulting magnitude of the scattered field, $|E_s|$, of the designed ISLS as a function of reactive load impedance.

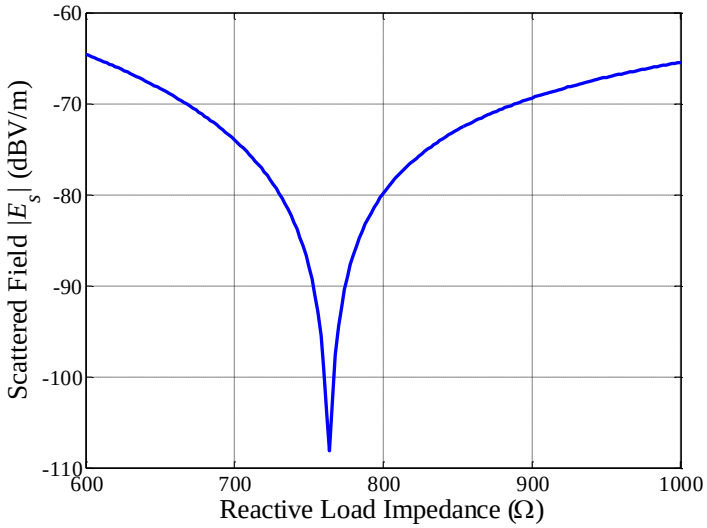

Figure 3.2. Scattering from an SLS centrally loaded with an ideal inductor as a function of load reactance.

As shown in Figure 3.2, when a reactive (inductive) load of ~764 Ω (corresponding to an inductance of 48.6 nH at the design frequency) is placed at the center of the scatterer, the magnitude of the scattered field, $|E_s|$, is significantly reduced, indicating that the scattered field approaches zero (i.e., the SLS becomes an ISLS). It should be noted here that $|E_s|$ is also significantly reduced by other reactance values (for example, $|E_s|$ is less than -70 dBV/m for reactive impedances in the range of ~675-900 Ω). However, the optimal load (764 Ω) is defined at the point of minimal scattering, herein referred to as the scattering null.

As mentioned above, the use of an inductive load affects the current induced along the length of the scatterer. To this end, the current induced along the length of this ISLS is shown in Figure 3.3. For comparison, the current induced on an open-circuited (i.e., high impedance load) SLS, of the same geometry is also included.

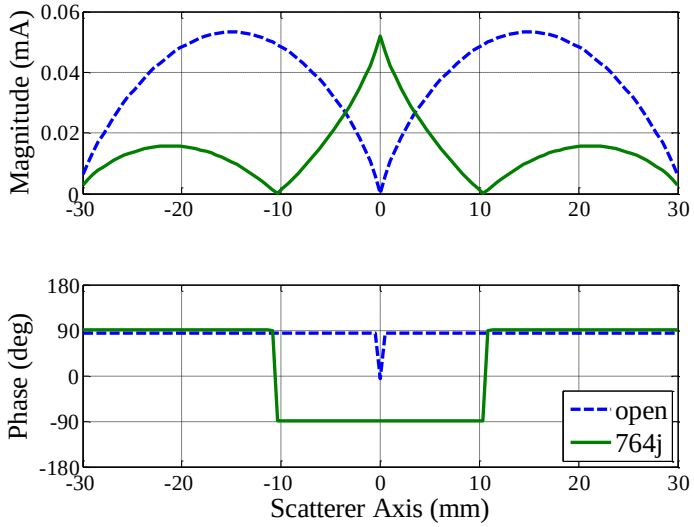

Figure 3.3. Distribution of current induced on an open-circuited SLS and a reactively loaded ISLS.

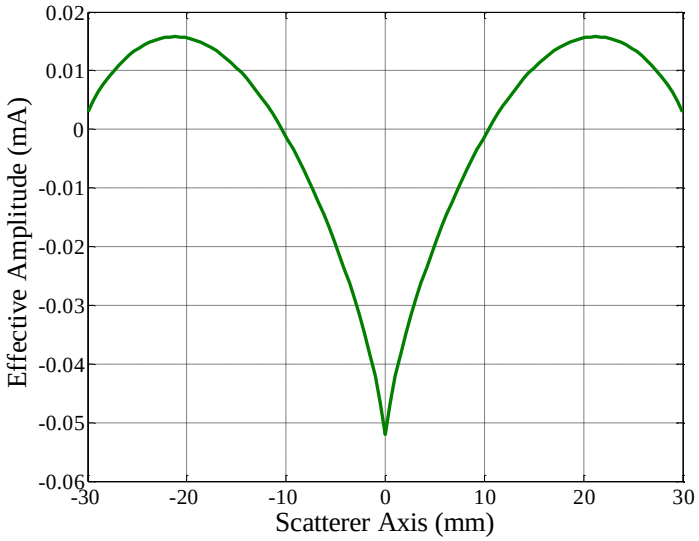

Figure 3.4. Effective amplitude of the induced current distribution on the ISLS.

As can be seen from Figure 3.3, the (approximate) 180° phase shift (mentioned above) is evident through the central region of the ISLS current distribution (solid line). As previously discussed, the phase shift introduced by the reactive load causes the integral of the current distribution to approach zero, which results in a scattering null. In

contrast, the current induced along the length of the open-circuited SLS (dashed line) has relatively uniform phase, hence the integral of the induced current (and the subsequent scattering) does not approach zero. To better illustrate this, Figure 3.4 displays the effect of the phase shift by incorporating the 180° phase shift as a coefficient of -1, allowing the induced current of the ISLS to be represented as an effective amplitude quantity. As can be seen from Figure 3.4, the effective amplitude of the ISLS current becomes negative over the central region of the scatterer (corresponding to the 180° phase shift shown in Figure 3.3). Representing the induced current in this way provides a better visualization of how the integral vanishes. This can be considered similar to that of an unbiased sinusoid, integrated over one period, where the negative and positive areas under the curve are equal, resulting in the integral of the curve (over one period) equaling zero. The above investigation of the ISLS current distribution leads to a good analogy which helps explain how the scattering null physically takes place. This phenomenon (i.e., electrical invisibility) can be considered similar to the superposition of two radiating antennas, collocated in space, with an excitation for one antenna that is 180° out of phase with respect to the excitation of the other antenna. Such a system would result in destructive interference of the radiation, thereby achieving electrical invisibility. Similarly, the scattering contributions from the center of the scatter (where the current is out of phase) destructively interferes with the scattering contributions of the outer sections (see Figure 3.4). The resulting scattering from this current distribution is therefore minimized. This is illustrated below in Figure 3.5, where the scattered field as a function of frequency is provided for the ISLS. From Figure 3.5, it is evident that the scattering null is very narrow with respect to frequency. This fact, when combined with the results of Figure 3.2, indicates that the frequency at which invisibility is achieved (scattering null) is quite sensitive to physical and/or operating parameters (e.g., scatterer dimensions, operating frequency, etc.), making such a sensor difficult to employ in practice (unless the precise scattering response is *a priori* known). Nonetheless, the ISLS may still have potential as a tool for materials characterization (e.g., structural health monitoring).

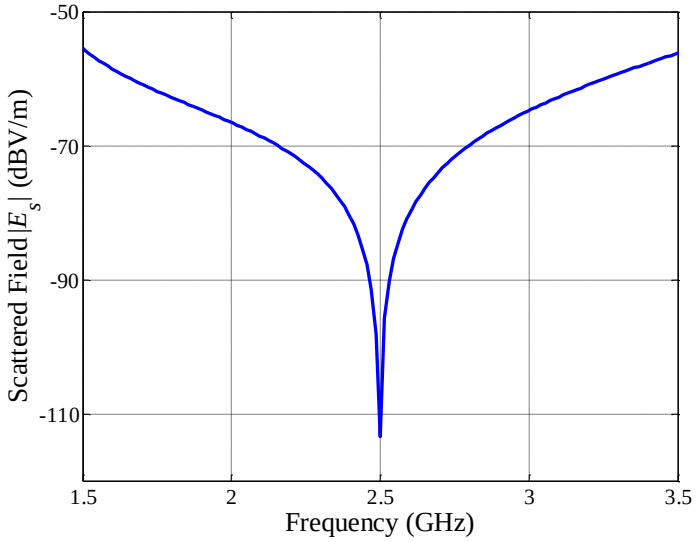

Figure 3.5. Scattering from the ISLS.

3.1.2. Application to Materials Characterization. Considering the results in Figure 3.2 and Figure 3.5, if any physical or operating parameters (frequency, load impedance or location, dipole length, dielectric properties of the material surrounding the ISLS, etc.) were to change, the condition for electrical invisibility would also change. To this end, such a scatterer may be designed to purposely lose (or gain) invisibility as a result of environmental (e.g., material property) changes. For example, cracks, ingress of chloride or moisture, etc., will change the dielectric properties of cement-based materials. Therefore, to investigate the potential of the ISLS as a materials characterization tool, an ISLS was designed to be invisible at 2.5 GHz in mortar (relative complex dielectric properties, ε_r, assumed to be 4 - j0.1). To achieve electrical invisibility for this case, an inductive load of ~33 nH was required.

Simulations were conducted to vary the relative permittivity (i.e., the real part of ε_r) that may result from changes in the material; for example, cracks may occur which may cause the permittivity to reduce, or the ingress of chloride or moisture may cause the permittivity to increase. The results of this simulation are shown in Figure 3.6.

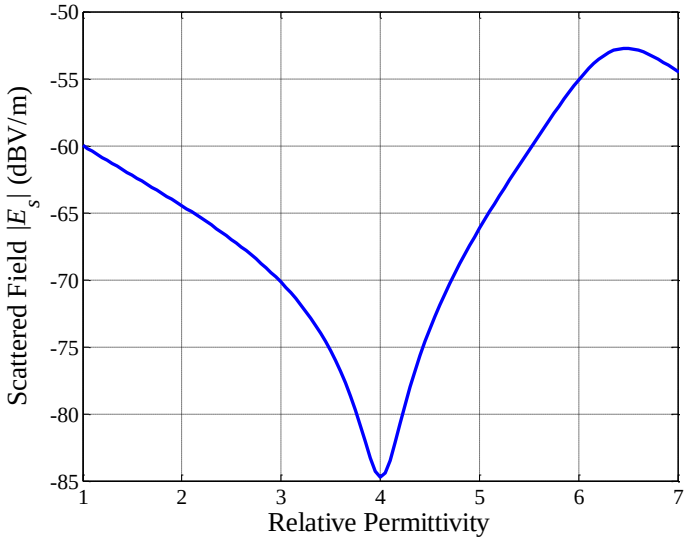

Figure 3.6. Scattering from an ISLS designed for invisibility in mortar as a function of relative permittivity.

As expected and evident in Figure 3.6, the scattered field of the ISLS is sensitive to changes in the surrounding material. Therefore, a scatterer may be designed to become visible if the permittivity in the vicinity of the probe decreases (for example, due to cracking), or increases (possibly due to the presence of moisture). However, for this case, the scattering null is quite wide, meaning a relatively large change in permittivity is required to change the scatterer from a visible to invisible state. An additional, practical concern is the magnitude of the scattered field itself. In order to reliably detect changes in E_s on the order of that shown in Figure 3.6, sensitive (expensive\complex) detection equipment may be required. Further, the ISLS cannot be modulated (modulation may improve detection as discussed in Section 1), making detection more challenging if the expected (visible state) response is not *a priori* known.

To this end, the addition of modulation capability may render an improved scatterer design useful for other MST applications [1] as well. As such, an improvement to the ISLS, referred to as the invisible dual loaded scatterer (IDLS) design, which maintains the ability to modulate between visible and invisible states, is considered next.

3.2. ELECTRICALLY INVISIBLE DUAL LOADED SCATTERER (IDLS)

A modeling approach, similar to that used for the ISLS, was used to simulate the scattering properties of an IDLS. As discussed in Section 1, the IDLS concept is based on the dual loaded scatterer (DLS) design [6]-[7] (shown in Figure 1.1b) with one load capable of modulation (e.g., a PIN diode) and the other an inductor similar to the ISLS. However, unlike an ISLS (which cannot be modulated), an IDLS maintains the capability for modulation. As mentioned above, the geometry (load placement, etc.) of the scatterer design directly affects the induced current and subsequent scattered field. As such, two (new) IDLS designs were considered. The first IDLS design, referred to as the "equidistant IDLS" design, was directly based on previous work done in [6]-[7] with one of the PIN diodes (see Figure 1.1b) replaced by an inductor, as shown in Figure 3.7a. A second IDLS design was also considered, where both loads (PIN diode and inductor) are collocated at the center of the scatterer in a parallel configuration, illustrated in Figure 3.7b, and referred to as the "collocated IDLS" design. The collocated IDLS design provides a load switching capability similar to what was done in [36]. In [36], a single-pole four-throw (SP4T) switch was used to switch between four different loads on the MST scatterer resulting in four different modulation states. Contrary to this design, the collocated IDLS design has one switching element (PIN diode) which effectively switches the inductive load in and out of the loading circuit (Figure 3.7b).

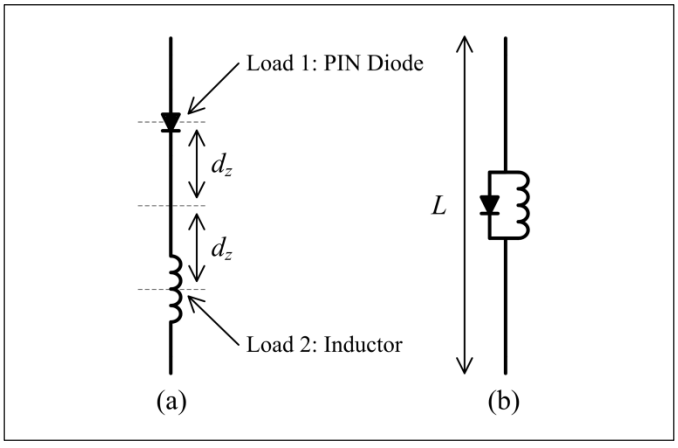

Figure 3.7. Schematic of IDLS designs: (a) equidistant IDLS design, (b) collocated IDLS design.

3.2.1. Equidistant IDLS Design. In order to determine the optimal (inductive) impedance necessary for electrical invisibility, simulations were conducted to study the effect of the inductor on the scattering properties of this design. The two loads were placed (equidistantly) a distance, d_z, of 15 mm ($\lambda/8$) from the center (see Figure 3.7a). The PIN diode was modeled (based on a Microsemi GC4270 PIN diode) as a resistance in series with an inductance (1.5 Ω and 0.6 nH respectively) during forward bias (FWD) and an inductance in series with a capacitance (0.6 nH and 0.2 pF respectively) during reverse bias (REV) [37]-[38], as shown in Figure 3.8.

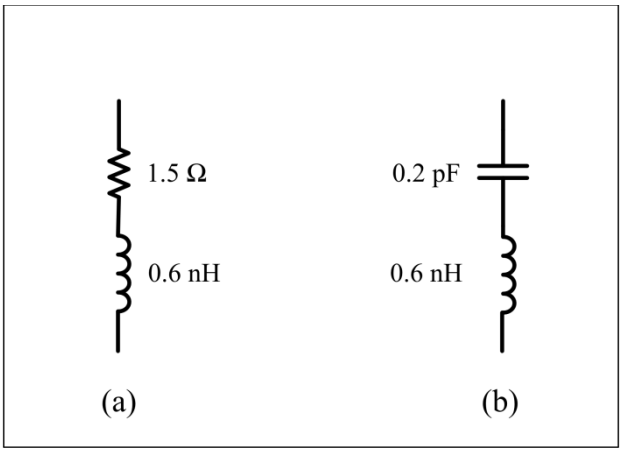

Figure 3.8. Equivalent circuit for the (a) FWD, and (b) REV, PIN diode states.

This model for the PIN diode FWD and REV states (shown in Figure 3.8) was utilized for all simulations presented herein. From the simulations, it was determined that a 36.6 nH inductor produced the optimal current distribution on the IDLS required to achieve electrical invisibility. The current distribution for this IDLS is shown in Figure 3.9a with the location of the load elements indicated on the figure. For comparison, the current distribution along the length of a traditional MST scatterer (half-wave dipole scatterer centrally loaded with a PIN diode as shown in Figure 1.1a), referred to herein as a "traditional SLS", was simulated at the design frequency and is shown in Figure 3.9b.

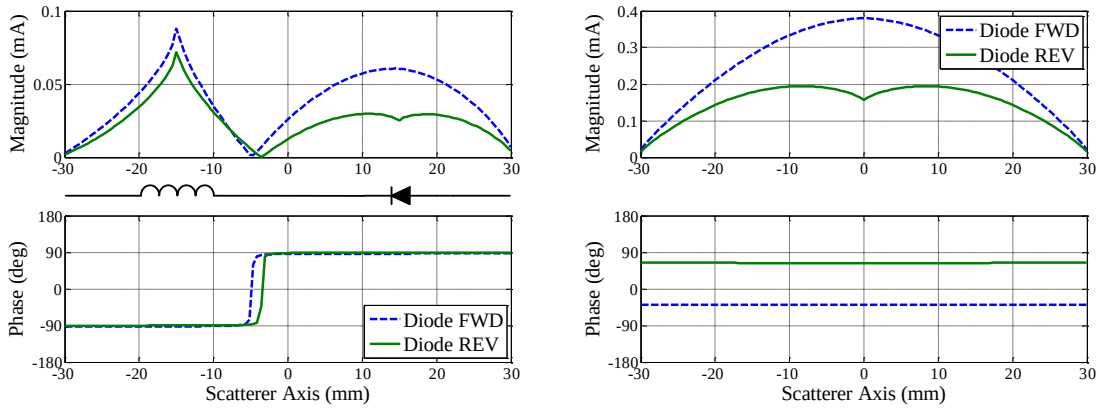

Figure 3.9. Current induced along the length of: (a) an equidistant IDLS (locations of the loads indicated by the scatterer schematic), (b) a traditional SLS.

From Figure 3.9a, it can be seen that the inductor causes a phase shift in the induced current, similar to the ISLS current of Figure 3.3, only the location of the inductor (and therefore the phase shift) is offset at a distance of -λ/8 (-15 mm) from the center of the scatterer. Likewise, at +λ/8 (15 mm), the effect of the diode can be clearly seen as the current is higher during the FWD state of the diode than during the REV state due to the low and high impedance of the respective diode states (similar to that shown in Figure 3.9b). As previously discussed, the phase shift caused by the inductor minimizes the integral of the induced current. It is evident from Figure 3.9a that this phase shift is present for both states of the diode, indicating the scattering from both states will be affected. To this end, $|E_s|$ of the equidistant IDLS, for both diode states, as a function of frequency is shown below in Figure 3.10a. For comparison, $|E_s|$ as a function of frequency for a traditional SLS was also simulated and is shown in Figure 3.10b.

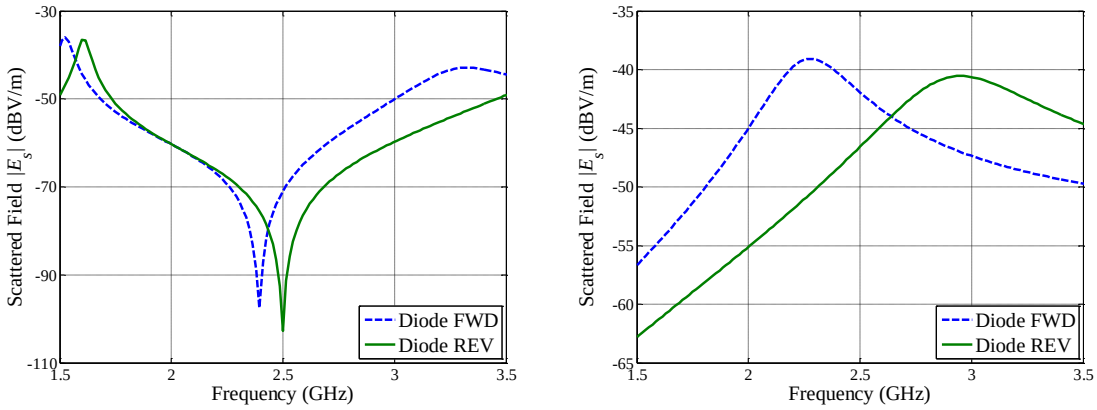

Figure 3.10. Scattering from: (a) the equidistant IDLS, (b) the traditional SLS.

As mentioned above, the objective of the IDLS design is to improve the MD of the scattered signal. Therefore, (1), the equation used to calculate MD from Section 1, was used to calculate the MD of the equidistant IDLS using the simulated scattered fields (shown in Figure 3.10a). At the design frequency, the equidistant IDLS has a MD of 95%. Using the simulated results shown in Figure 3.10b, the modulation depth at 2.5 GHz for the traditional SLS was likewise calculated using (1) to be 26%. However, as can be seen in Figure 3.10b, the maximum MD for the traditional SLS does not occur at the design frequency, but rather at 2.26 GHz. For such a scatterer, the MD could be improved by adjusting physical parameters of the scatterer so that the maximum scattering occurs at the design frequency. Using the results at this frequency, the (maximum) MD for the traditional SLS is approximately 59%, which is better than the 26% MD at the design frequency but still less than the 95% MD achieved by the IDLS. Thus, the IDLS introduces a substantial improvement in modulation depth, which is quite significant as it relates to the detection of scattered signals for MST.

However, this improvement to the MD is not without practical drawbacks. When comparing the simulated results of the equidistant IDLS design (Figure 3.10a) to those of the traditional SLS (Figure 3.10b), it is evident that the phase shift in the induced current (caused by the inductive load) decreases the scattering during the REV state of the diode, which is desired (i.e., the invisible state). However, it is also evident from Figure 3.10

that the effect of the inductor (phase shift in the current which reduces scattering) is present regardless of the PIN diode state. At the design frequency, the scattering from the equidistant IDLS (shown in Figure 3.10a) during the FWD state of the diode is 30 dB less than the scattering of the traditional SLS (shown in Figure 3.10b) during the same diode state. This reduction in the FWD state scattering could prevent a less sensitive detection system from reliably detecting the FWD state signal. In addition, the inductor causes both states of the IDLS to have scattering nulls very close in frequency (shown in Figure 3.10a) which may also cause detection challenges (e.g. reliably distinguishing between the two states) for practical detection systems. Ultimately, these practical challenges may outweigh the improvements gained by increasing the MD. To this end and in order to alleviate these challenges, the second IDLS design, the collocated IDLS design, was developed and is discussed next.

3.2.2. Collocated IDLS Design. In an effort to mitigate the potential drawbacks of the equidistant IDLS design discussed above, a new IDLS design, referred to as the collocated IDLS design, was considered (shown in Figure 3.7b). The intention of this design is to modulate between visible and invisible scattering states without decreasing the scattering during the FWD state of the diode, when compared to that of a traditional SLS, thereby reducing the detection challenges presented by the equidistant IDLS discussed above. This is achieved by utilizing the PIN diode to effectively switch the inductor in and out of the load circuit. More specifically, when the PIN diode is in the FWD (low impedance) state, the parallel combination of the collocated loads will resemble that of the SLS (Figure 1.1a) in the same state, effectively removing the inductor and the subsequent phase shift in the induced current. Similarly, during the REV (high impedance) state of the diode, the reactive impedance of the inductor will dominate and the scatterer will resemble an ISLS, operating in the electrically invisible state (see Figure 3.3). This concept is presented in Figure 3.11 which shows the ideal performance of the collocated IDLS when considering the PIN diode as an ideal switch.

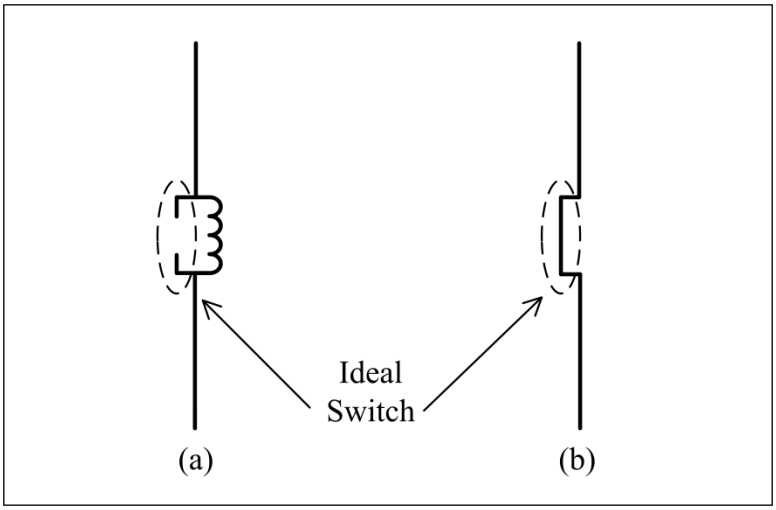

Figure 3.11. Performance of the collocated IDLS utilizing an ideal switching element.

This design approach (shown in Figure 3.11) is similar to that of reconfigurable antennas, where switching elements (e.g., PIN diodes) are used to change physical parameters of an antenna by electrical connections (switch on) or disconnections (switch off) [39].

As above, using the MM simulations, the optimal value for the reactive impedance (i.e., inductive load) to achieve electrical invisibility was determined. It was found that an inductance of 14 nH was optimum; which, when combined in parallel with the impedance of the REV state of the PIN diode (0.2 pF in series with 0.6 nH, as shown in Figure 3.8) resulted in a reactive impedance of approximately 764 Ω at the design frequency. This is the same impedance value required for electrical invisibility of an ISLS (discussed above), which is to be expected since the collocated IDLS design also loads the scatterer in the center (e.g., SLS) for electrical invisibility. In order to illustrate the effect of the collocated loads on the IDLS, the current distribution at the design frequency (for both PIN diode states) is shown in Figure 3.12. For comparison, Figure 3.12 represents the current distribution of a traditional SLS during the FWD state of the diode (shown in Figure 3.9b) with square markers, and the current distribution of the ISLS (shown in Figure 3.3) with circle markers.

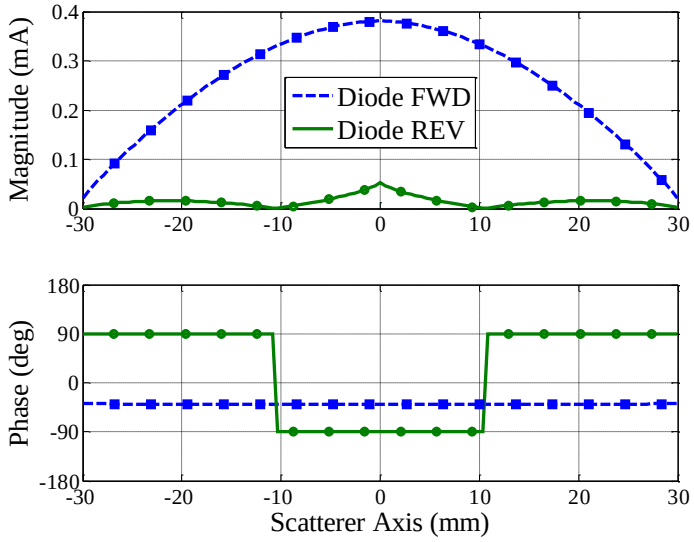

Figure 3.12. Current induced along a collocated IDLS (the square markers represent the current distribution of a traditional SLS during the FWD state of the diode and the circle markers represent the current distribution of the ISLS).

It is evident from Figure 3.12 that during the REV (high impedance) state of the diode, the current distribution of the collocated IDLS design matches that of an ISLS (SLS loaded with inductor only), which is shown in Figure 3.3 and represented in Figure 3.12 by circle markers. This current distribution was expected since the parallel combination of the REV diode and the 14 nH inductor resulted in the same reactive impedance (~764 Ω) of the ISLS discussed in Section 3. Similarly, during the FWD (low impedance) state of the diode, the current distribution of the collocated IDLS design matches that of a traditional SLS during the same state of the diode, which is shown in Figure 3.9b and represented in Figure 3.12 by square markers. This correlation of the current distribution is attributed to the fact that the load impedance of the collocated IDLS, during the FWD diode state, matches that of the FWD diode only. From the results of the current distribution simulations (Figure 3.12), it is expected that the scattering of the collocated IDLS will resemble that of a traditional SLS during the FWD state of the diode and that of an ISLS during the REV state of the diode. To this end, the magnitude of the simulated scattering, $|E_s|$, for this design is presented in Figure 3.13 as a function of frequency.

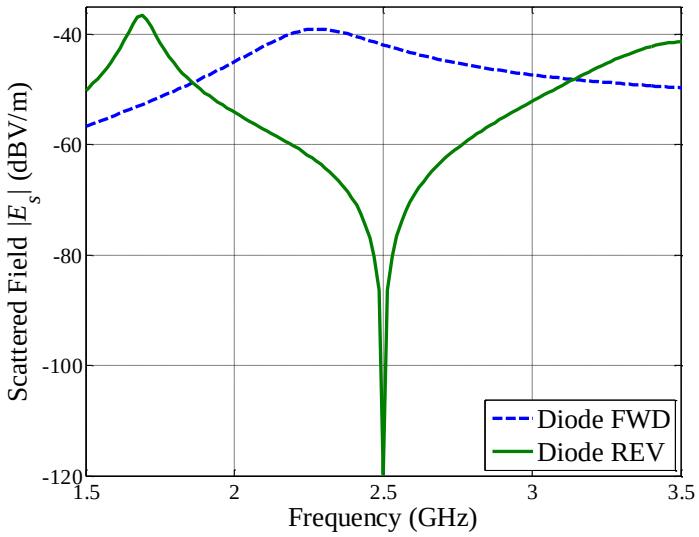

Figure 3.13. Scattering from the collocated IDLS design.

As can be seen from Figure 3.13 (and comparing to Figure 3.10b), the FWD state of the PIN diode produces |*Es*| identical to that of the traditional SLS for the same diode state. Further, the REV state is minimized (invisible) at 2.5 GHz. Such a response during both states was expected from the current distribution shown in Figure 3.12. Thus, the collocated IDLS provides the response of an ISLS (invisible at the design frequency) during the REV state of the diode while maintaining the ability to modulate between this invisible state and a visible (scattering) state during the FWD state of the diode. Moreover, the scattering during the visible state is 30 dB higher than the corresponding state of the equidistant IDLS design. Using the results shown in Figure 3.13 and (1), the MD at 2.5 GHz was calculated to be 99.9% (meaning the design effectively achieved electrical invisibility). Not only is the simulated MD for the collocated IDLS design improved as compared to the equidistant IDLS design (95% MD), but the potential measurement issues have also been mitigated. More specifically, |*Es*| during the FWD state of diode has substantially increased compared to the equidistant IDLS (by nearly 30 dB); therefore, less sensitive (i.e., lower cost) measurement equipment may be more readily utilized [40].

Given that simulations showed the collocated IDLS has the potential to significantly improve the MD of MST scatterers while improving the robustness and

(measurement) practicality (as compared to the equidistant design), the collocated design was considered for further analysis. More specifically, fabrication of the collocated IDLS on a printed circuit board was considered for the manufacturing flexibility offered by such an implementation.

3.3. PRINTED CIRCUIT BOARD (PCB) IDLS

Given the improvements to the MD offered by the collocated IDLS design (discussed above), it was decided to study the implementation of such a scatterer on a printed circuit board (PCB) due to the ease and precision of PCB fabrication (e.g., such scatterers are easily mass produced). Additionally, scatterers implemented on a PCB are built on some form of substrate (e.g., FR4) which provides mechanical support for the scatterer. More specifically, due to the small size of MST scatterers, when realized using lumped elements and wire, they may be easily bent or broken. The mechanical support of the PCB substrate may help to mitigate these issues. A PCB implementation also provides the ability to use integrated loads (e.g., printed spirals for inductance) instead of lumped elements which may result in better precision (e.g., more exact load impedances). To this end, CST Microwave Studio® (CST MWS) [24] was used to simulate a PCB implementation of the collocated IDLS (also designed to operate at 2.5 GHz). Schematics of the new designs are shown below in Figure 3.14.

As shown in Figure 3.14a, vias are used to connect the scatterer (on the top layer of the PCB) to the inductive load on the back layer of the board underneath the pin diode. In this way, the design places the loads in parallel. It is well known that vias are a source of parasitic inductance [41], which is usually unwanted in board designs. However, in this case, inductive loading is desired. Therefore, the use of vias results in a lower value of (lumped element) inductance required for invisibility. This is helpful when selecting physical components for scatterer fabrication since as the inductance of surface mount inductors is reduced, it is common for the self-resonant frequency (SRF) to increase. It is necessary to utilize inductors well below their respective SRF since operating at frequencies near and beyond the SRF causes the impedance of the inductor to vary significantly (i.e., resonant effects) from the intended value.

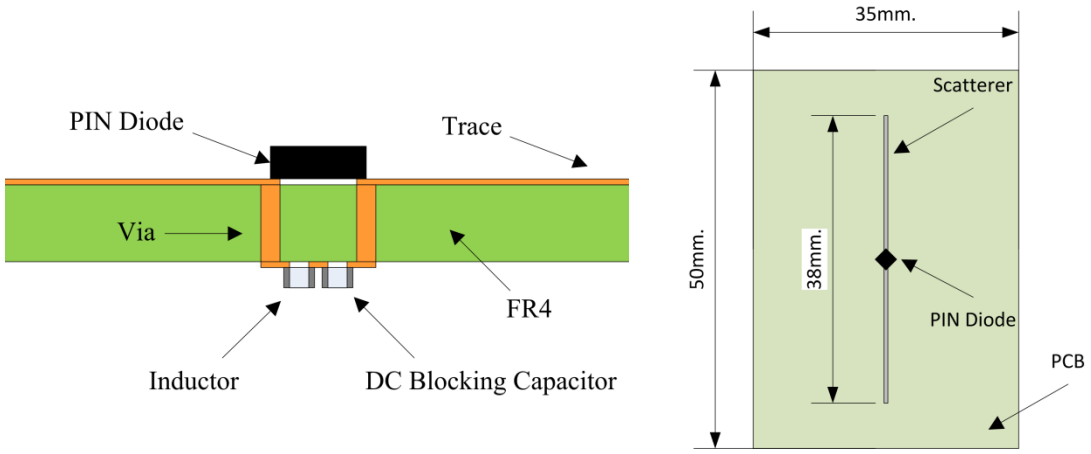

(a) (b)

Figure 3.14. Schematic of the PCB-based collocated IDLS: (a) side and (b) top view.

A first-order approximation of the lumped element inductance provided by the via can be obtained from the equation below [42]:

$$L_{via} = \frac{\mu_0}{2\pi}\left[h * ln\left(\frac{h+\sqrt{r^2+h^2}}{r}\right) + \frac{3}{2}\left(r - \sqrt{r^2+h^2}\right)\right] \quad (46)$$

where h is the dielectric (here FR4) height and r is the via radius. This equation was originally derived for calculating the inductance of vias from microstrip to a ground plane which is not the case here. However, (46) is used here to get an order of magnitude understanding of the parasitic inductance provided from the vias [42]. Using (46), the lumped element inductance was calculated to be approximately 0.6 nH (per via).

The pad and hole size for the vias is determined by the fabrication constraints of the PCB manufacturer and alignment with the trace width. For this simulation, the diameter of the hole was set to 15 mils with an assumed coating thickness of 5 mils, and the pad size was set at 0.6 mm. Smaller via pads and hole sizes are also possible which may be necessary for higher frequency designs. The traces on the back side of the scatterer (shown in Figure 3.14) were designed for 0201 surface mount components using the suggested pad dimensions from [43]. A trace width of 0.511 mm was chosen to correspond to the wire scatterers simulated in the previous Sections which had a diameter

of 0.511 mm (24 AWG). The length was optimized to achieve maximum scattering at the design frequency which resulted in a total scatterer length of 38 mm (as shown in Figure 3.14b). Using the CST MWS model, it was determined that a value of 6 nH for the load inductance (see Figure 3.14a) resulted in minimum $|E_s|$ (electrical invisibility) at 2.5 GHz. The simulated scattering, $|Es|$, from this design is shown below in Figure 3.15.

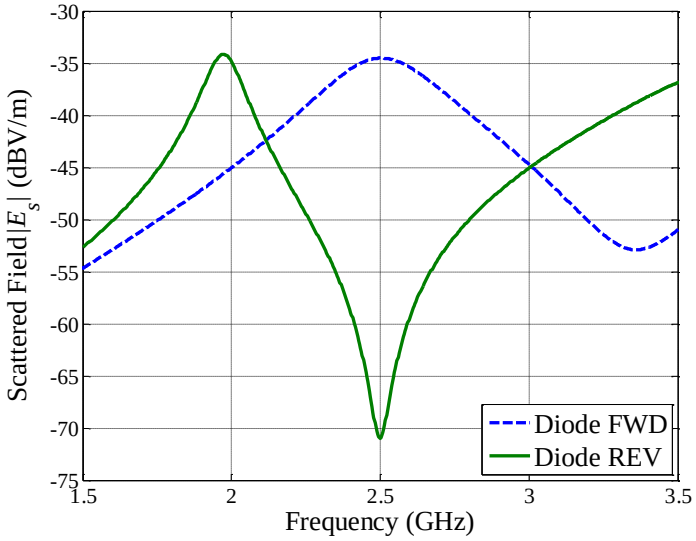

Figure 3.15. Scattering from the PCB-based collocated IDLS design.

Figure 3.15 displays the simulated broadside scattering of the design, for both states of the diode, under plane wave illumination (as was used in the simulations of the wire scatterers discussed above). A lumped element of 0.22 µF was simulated for the DC blocking capacitor (required in practical applications to prevent diode biasing currents from shorting through the inductor). This capacitance value was chosen due to the relatively low frequency break-over point which prevents the impedance of the capacitor from affecting the loading circuit at the design frequency (GHz range). From Figure 3.15, it is evident that the scatterer performs similar to that of the simple wire-based version of the collocated IDLS (see Figure 3.13). Using (1) and the results displayed in Figure 3.15, the MD at 2.5 GHz was calculated to be 97%.

A similarly designed (PCB-based) traditional SLS was also simulated and analyzed for comparison. The structure was identical to that of the PCB version of the collocated IDLS described above (without the parallel loading aspect). The $|E_s|$ of the traditional SLS, for both states of the diode, is given below in Figure 3.16.

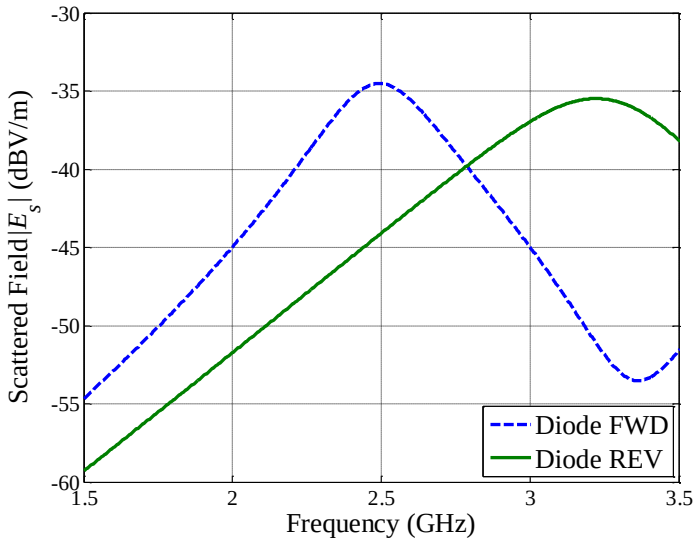

Figure 3.16. Scattering from the PCB-based traditional SLS.

From Figure 3.16, it is evident that the simulated $|E_s|$ during the FWD state of the diode is identical to that for the IDLS design (as shown in Figure 3.15). However, the $|E_s|$ of the scatterer during the REV state of the diode is significantly higher, which corresponds to lower modulation depth. The modulation depth at 2.5 GHz for this scatterer was calculated to be only 50%. It should be noted here that the simulations show an improved MD could be achieved at a higher frequency (~76% at 3.35 GHz) where the scattering from the REV state surpasses the scattering from the FWD state. However, this would not only require the scatterer be designed larger with respect to wavelength (often undesirable), but also the MD achieved would still be less than that achieved by the collocated IDLS design. Therefore, the PCB version of the collocated IDLS should significantly improve the performance (i.e., MD) of MST scatterers when compared to a traditional SLS likewise implemented on a PCB.

Clearly, the MD of MST scatterers has been improved. However, the results discussed above only consider broadside monostatic scattering. This means the scattering is calculated on the same axis as the incident plane wave propagates, as shown in Figure 3.17.

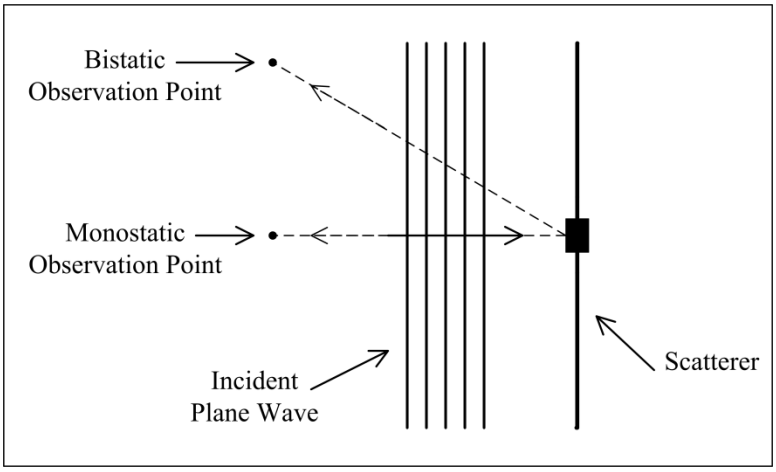

Figure 3.17. Monostatic vs. Bistatic Observation Points.

This may not be representative of practical applications of MST scatterers which are often utilized in bistatic (shown in Figure 3.17) applications. Therefore, in order to understand the operation of the collocated IDLS under bistatic scattering, the three dimensional (far-field) radiation pattern of the design is considered next.

3.3.1. Radiation Pattern. In order to investigate the performance of the PCB-based collocated IDLS (discussed above) in a bistatic system, the three dimensional radiation pattern was simulated in CST MWS and is shown below in Figure 3.18 for both the FWD and REV states of the diode. Additionally, two dimensional slices of the patterns (presented in Figure 3.18) are provided for further analysis in Figure 3.19. The results shown in Figure 3.18 and Figure 3.19 were obtained with the scatterer aligned on the y-axis and the excitation (plane wave) incident from the z direction. Note that this orientation is different from the simulations discussed in Section 2, where the scatterer was oriented on the z-axis.

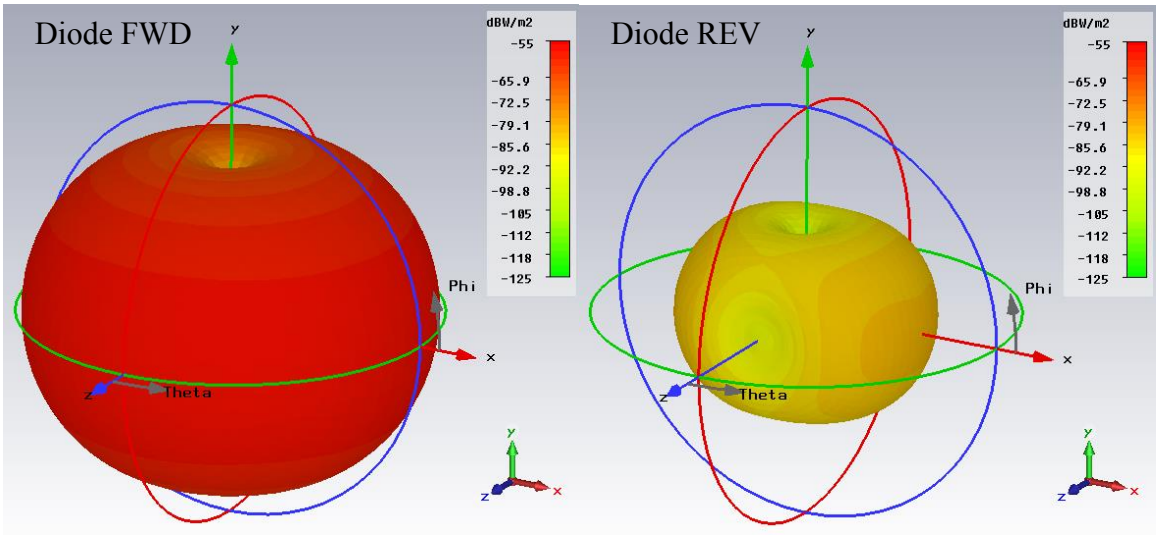

Figure 3.18. Radiation Pattern of PCB-based collocated IDLS design.

The patterns shown in Figure 3.18 and Figure 3.19 are consistent with that expected from a linear scatterer since there are nulls in the pattern on the y-axis (corresponding to the ends of the scatterer). During the FWD state of the diode, the PCB-based collocated IDLS produces relatively uniform scattering (radiation) at broadside (for this simulation broadside is the Phi=0 plane) with the maximum at theta equal to zero (as defined in Figure 3.18).

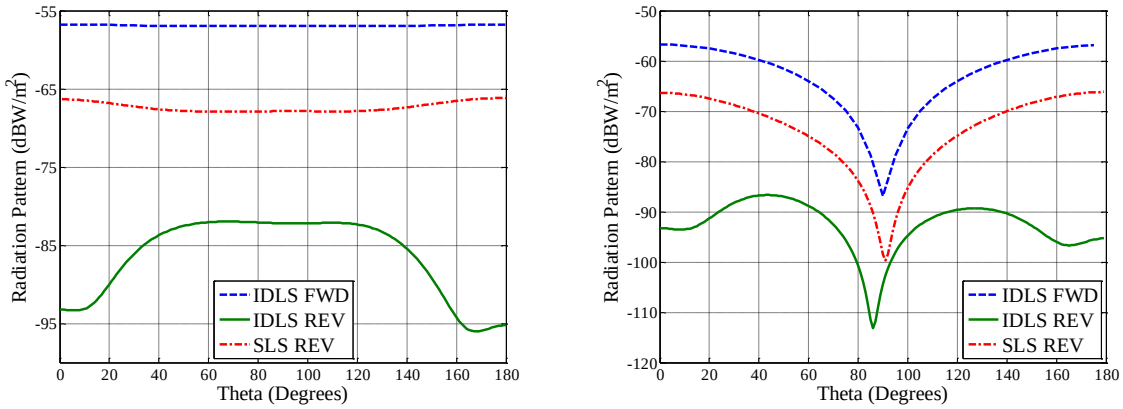

Figure 3.19. Radiation pattern of the PCB collocated IDLS: (a) Phi = 0°, (b) Phi = 90°.

Considering the pattern for the REV state of the diode, a radiation minimum is shown to occur broadside at Theta equal to zero as expected (where the radiation was maximum during the FWD diode state). Additionally, the REV state pattern indicates the scattering increases (i.e., the scatterer becomes less invisible) as the observation point moves away from the z-axis (observation along the z-axis would be the monostatic case as shown in Figure 3.17). This corresponds to a decrease in MD for certain bistatic cases. However, Figure 3.19 also shows that the scattering is significantly less in all directions from that of the traditional SLS during the REV diode state. This means that even though the maximum MD (and electrical invisibility) only occurs for specific observation angles, the MD achieved by the collocated IDLS will still outperform that achieved by a traditional SLS, regardless of the observation angle.

Although the performance (i.e., MD) gains achieved by this design may be significant, non-ideal effects of the practical system may decrease performance. One aspect of practical implementation that may hamper the performance is the scattering from wires utilized to deliver the biasing current necessary to modulate the diode. The effect of these wires is investigated next.

3.3.2. Effects of Diode Biasing Wires. The CST MWS model of the PCB-based collocated IDLS lends itself well to the investigation of practical effects such as those from the diode biasing wires. This investigation was done in order to better understand the performance of the scatterer in practical applications. In this design, the biasing wires are connected to the back side of the scatterer through high impedance lumped elements (in this case a 500Ω resistance), in order to prevent high frequency currents from leaving the scatterer and flowing into the biasing circuitry. The simulated biasing wires had a length of 0.5 m and radius of 0.0635 mm (corresponding to the 36 AWG wire used for measurements discussed in Section 4) and are placed normal to the incident electric field to reduce interference. The scattering from the PCB-based collocated IDLS including the biasing wires is shown below in Figure 3.20.

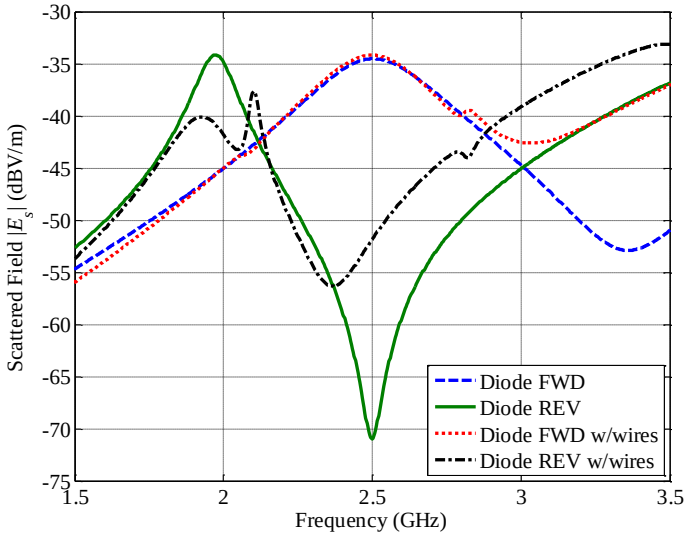

Figure 3.20 Scattering from the PCB-based IDLS including biasing wires.

From Figure 3.20, it is evident that the wires change the simulated response of the scatterer. Most notably, the depth of the scattering null at 2.5 GHz is significantly reduced. More specifically, the addition of biasing wires decreased the MD at the design frequency to 77%; much less than the 97% MD achieved by the scatterer simulated without the biasing wires (Figure 3.15). This is to be expected since the biasing wires, although small and normal to the incident electric field, will scatter some of the incident signal, effectively increasing the ambient noise and partially masking the scattering null. To improve the sensitivity, steps may be taken to reduce or remove the effect of the biasing wires. For instance, optical diodes may be utilized which do not require biasing wires. However, even without improvements, the 77% MD achieved in this case is still better than the 50% achieved by the ideal PCB-based traditional SLS (shown in Figure 3.16). The effects of the biasing wires are further investigated with measurements, which will be discussed in Section 4.

3.4. SUMMARY

In this Section, the theory of electrically invisible antennas was shown to be successfully integrated with the design of MST scatterers in order to increase the modulation depth (MD) of such scatterers. The Method of Moment (MM) simulations,

developed in Section 2, were utilized to investigate the scattering of small wire scatterers (i.e., $L = \lambda/2$) with various loading configurations in order to design the new MST scatterers. These new MST scatterers were based on the design of previously developed dual loaded scatterers (DLS) but with one PIN diode load being replaced with an inductor. This inductor was used to cause a 180° phase shift in the induced current which resulted in a zero scattering (i.e., electrically invisible) state.

Two designs of such an invisible DLS (or IDLS) were presented, the first of which was loaded by an inductor and PIN diode separated equidistantly about the center of the scatterer. Simulations of this design were presented and showed the design had the ability to modulate between visible and invisible states, with an achieved MD of 95%. However, the visible (i.e., scattering) state was significantly less (in magnitude) than a traditional (single loaded) MST scatterer. This may limit the detectability of such a scatterer. To mitigate this issue, a second IDLS design was proposed in which the PIN diode and inductor are collocated at the center of the scatterer. This design resulted in the ability to remove the effect of the inductor during the forward biased state of the diode (i.e., the electrically visible state). The simulations of this design showed that such an IDLS can be designed to scatter in the same way as a traditional MST scatterer while maintaining the ability to also operate in a zero scattering (invisible) state. Simulations showed this design to be (theoretically) capable of a MD greater than 99%.

With the concept of the new IDLS successfully shown, CST Microwave Studio® (CST MWS) [24] was used to simulate the performance of a more practical IDLS fabricated on a PCB. The PCB version of the scatterer was shown to have good performance, achieving a simulated MD of 97%. The CST MWS model was further utilized to examine the non-ideal effects caused by the diode biasing wires in a practical setup. Although the wires were shown to degrade the performance of the IDLS, it still performed significantly better (higher MD) than a traditional SLS likewise implemented on a PCB.

Overall, the new MST scatterer designs have been shown to significantly improve the MD of such scatterers. To further investigate these new designs, Section 4 presents measurement results of these MST scatterers.

4. MEASUREMENTS

The application of electrically invisible antenna theory to the design of MST scatterers was shown, by simulations in Section 3, to have potential for significant improvement in the modulation depth (MD) of such scatterers. In order to further investigate this potential performance improvement (i.e., increase in MD), this Section presents measurement results of scatterers constructed similar to those simulated in Section 3. More specifically, an invisible single loaded scatterer (ISLS), a traditional single loaded scatterer (traditional SLS), and an invisible dual loaded scatterer (IDLS) were constructed "by hand" from wire and lumped elements. The constructed IDLS followed the collocated IDLS design presented in Section 3. Additionally, a collocated IDLS implemented on a printed circuit board (PCB), which was simulated and discussed in Section 3, was also constructed and measured. The details of the fabrication and measurements of the scatterers listed above are presented next.

4.1. SCATTERER FABRICATION

4.1.1. Single Loaded Scatterer Fabrication. Two single loaded scatterers (SLS) were constructed for measurement. The first was an ISLS loaded with an inductor in order to achieve electrical invisibility at a specific frequency. The second was a traditional SLS loaded with a PIN diode. The traditional SLS was constructed for comparison to other scatterers. The details of the construction of each scatterer are given below.

The ISLS was fabricated from 24 AWG (0.511 mm radius) wire sections cut such that once soldered to the load (i.e., an inductor), the length was approximately 60 mm ($\lambda/2$ at 2.5 GHz). A design frequency of 2.5 GHz was selected based on load component availability. More specifically, appropriate inductors with a self-resonant frequency (SRF) above 2.5 GHz are commercially available. The SRF is important to consider when selecting load inductors since the impedance of the inductor varies greatly from the intended value when operating near the SRF (high impedance due to resonance with parasitic capacitance of the package) and above the SRF (capacitive effects dominate) [44]. In this case, the ISLS was centrally loaded with 33 nH surface mount (0201

package) inductor manufactured by TDK (MLK0603L33NJT) [43]. This inductance (33 nH) is less than the optimal value (48.6 nH) determined by simulations in Section 3, however, it was chosen based on availability and specified SRF. The typical SRF (specified by the manufacturer) for this inductor is 4.4 GHz [43]. To illustrate the effect of SRF, the impedance of this inductor is plotted versus that of an ideal inductor below in Figure 4.1.

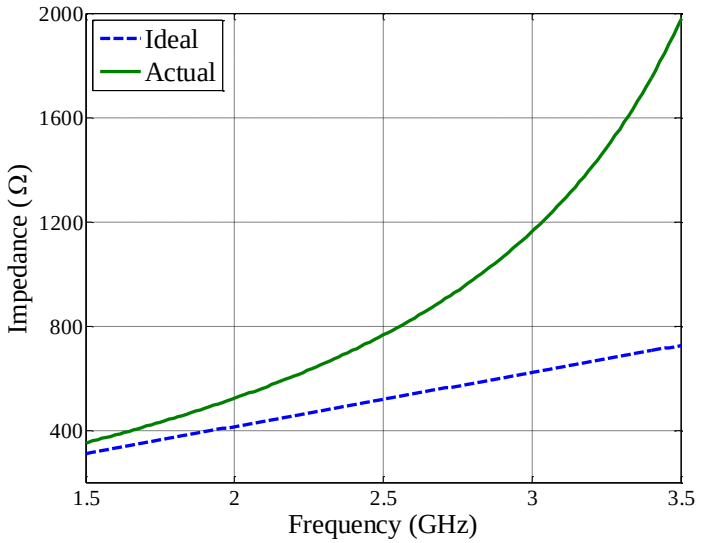

Figure 4.1. Impedance of the 33 nH Inductor.

From Figure 4.1, it is evident that the impedance of the inductor varies more than 200 Ω from ideal at the design frequency. In this case, the variation of impedance is beneficial since the actual impedance of the 33 nH inductor is 765.5 Ω at 2.5 GHz, which is very close to the impedance of the ideal 48.6 nH inductor used in the simulations (764 Ω) at the same frequency. However, some variation in the frequency at which electrical invisibility is achieved should be expected with any variation in impedance (as is discussed in Section 3 and shown in Figure 3.2). Also, the inductor used has a ± 5% tolerance for the value of the inductance (31.35 to 34.65 nH) [43], which may also lead to variation in the frequency at which the scattering null is observed. For this reason, swept

frequency measurements were conducted from 1.5 to 3.5 GHz, in order to ensure the frequency at which the ISLS becomes invisible was measured.

Another practical issue regarding the construction of the ISLS is mechanical strength. The structural strength of the load inductor, which is quite small (0.6 × 0.3 mm), is quite weak, causing the scatterer to easily break if pressure is applied to the load junction. For this reason, the scatterer was taped to a small piece of cardboard (the effect of the cardboard on the scattering properties of the ISLS is expected to be negligible) for mechanical stability during measurements. Figure 4.2 shows a photograph of the constructed ISLS.

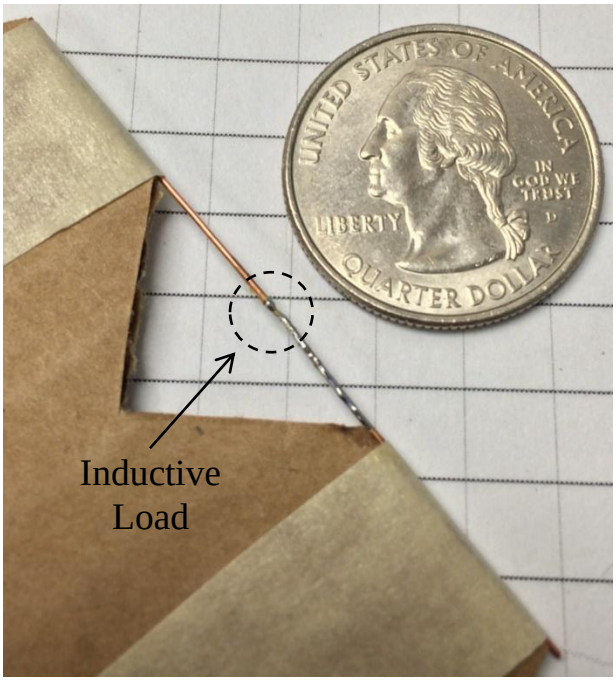

Figure 4.2. Constructed ISLS.

It should be noted that the cardboard has been cut away in the center (as shown in Figure 4.2) in order to minimize its effect on the ISLS response as the current (and scattered fields) are strongest at the center for this design (see Figure 3.3).

For purposes of comparison, a traditional SLS (see Figure 1.1) was similarly constructed. This SLS utilized the same wire size (24 AWG) and basic geometry as the

ISLS; however, it was loaded in the center with a Microsemi GC4270 PIN diode [45]. Small biasing wires (36 AWG) were connected at the ends of the scatterer to deliver the DC biasing current necessary for PIN diode modulation. These biasing wires were connected through ferrite chips in order to prevent high frequency currents, induced on the scatterer, from entering the biasing circuitry. A photograph of the traditional SLS is shown below in Figure 4.3.

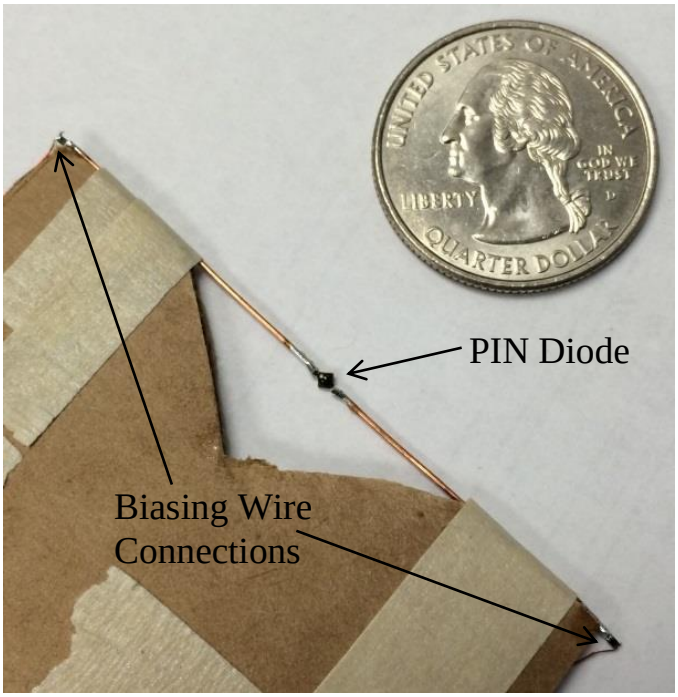

Figure 4.3. Constructed Traditional SLS.

In Figure 4.3, PIN diode load and biasing wires can be seen. Again, the cardboard has been cut away in the center in order to minimize its effect on the induced current. Using a similar process, the collocated IDLS design was also fabricated, as explained next.

4.1.2. IDLS Fabrication. The IDLS (collocated IDLS design from Section 3) was fabricated in a similar fashion to the traditional SLS, but with different elements used for the load circuit. The IDLS was centrally loaded with a Microsemi GC4270 PIN diode [45] in parallel with a 15 nH surface mount (0201 package) inductor manufactured by TDK (MLK0603L15NJT) [43]. This inductance is slightly higher than that determined as

optimal (14 nH) by simulations in Section 3; however, it was chosen based on availability. As a result, slight variation in the frequency at which electrical invisibility is achieved is expected. Again, swept frequency measurements were conducted from 1.5 to 3.5 GHz, in order to ensure the invisible state of the IDLS response was measured. The typical SRF (specified by the manufacturer) for the 15 nH inductor used for the IDLS is 6.6 GHz [43], which results in an impedance variation of approximately 50Ω from ideal at the design frequency. This variation may also contribute to the deviation of the IDLS scattering null from the design frequency. Additionally, a surface mount (0201 package) 0.22 μF capacitor (ECJ-ZEB0J224M) was included in series with the inductor to block the PIN diode DC biasing currents from saturating the inductor. A relatively high capacitance was chosen so that the impedance of the capacitor would be negligible at the measurement frequencies (~0.3 mΩ at 2.5 GHz).

4.1.3. PCB Scatterer Fabrication. PCB versions of the collocated IDLS (presented in Section 3) and traditional SLS were also fabricated. The scatterers were designed and optimized in CST MWS (as discussed in Section 3) and then transferred to a PCB layout for fabrication. The scatterer loads and biasing wires were soldered onto the PCB-based IDLS and SLS scatterers. A photograph of the PCB-based IDLS is shown below in Figure 4.4.

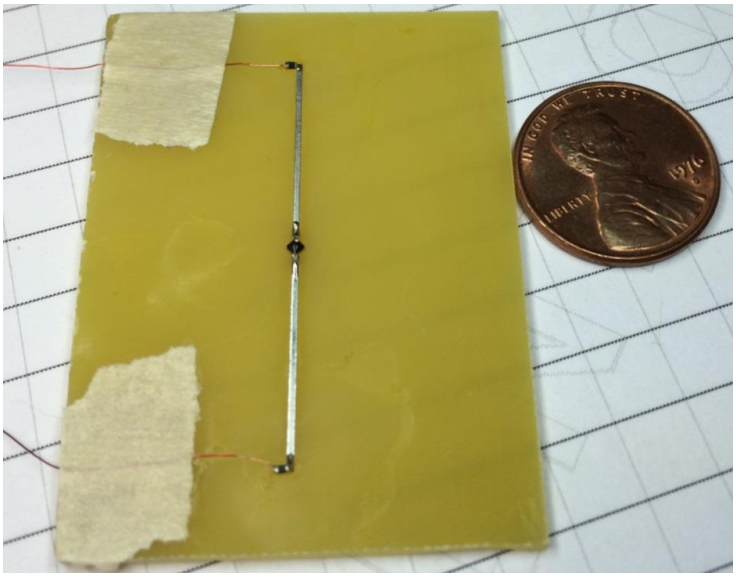

Figure 4.4. PCB-based collocated IDLS.

The PIN diode, biasing wires and connections, and the DC blocking capacitor are all identical to those used for the wire version of the IDLS (described above). The scatterer was loaded with a 6.2 nH TDK surface mount inductor (MLK0603L6N2ST) [43], along with the DC blocking capacitor (described above), which were both soldered to the back of the IDLS as shown in Figure 4.5 below. This particular inductor has a tolerance of ± 0.3 nH which (along with the nominal value of 6.2 nH) may result in an inductance different than the optimal value (6 nH) determined by the simulations. Such variation in the inductance may cause slight variation in the frequency at which electrical invisibility is achieved. The swept frequency measurements will ensure the scattering null is observed. The typical SRF of the inductor is 8.2 GHz [43], which indicates the inductor will closely resemble an ideal inductor at the design frequency. The PCB version of the traditional SLS was constructed similarly (but without the vias and load on the back side). The measurement setup used to evaluate all the constructed scatterers is discussed next.

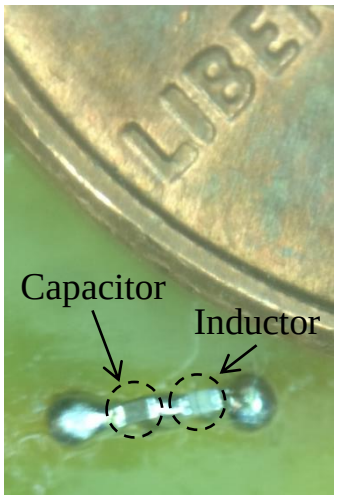

Figure 4.5. Back side of the PCB-based collocated IDLS showing the inductive load and DC blocking capacitor.

4.2. MEASURMENT SETUP

To conduct the measurements, each scatterer, also referred to in this Section as the device under test (DUT), was placed (individually) on a structure of very low permittivity (i.e., relative permittivity of 1.15) foam resembling free-space. This block was placed inside a measurement enclosure (semi-anechoic chamber) approximately 0.5 m from the aperture of two 1-4 GHz ridged horn antennas, as illustrated in Figure 4.6. Photographs of the setup described in Figure 4.6 are shown in Figure 4.7 and Figure 4.8.

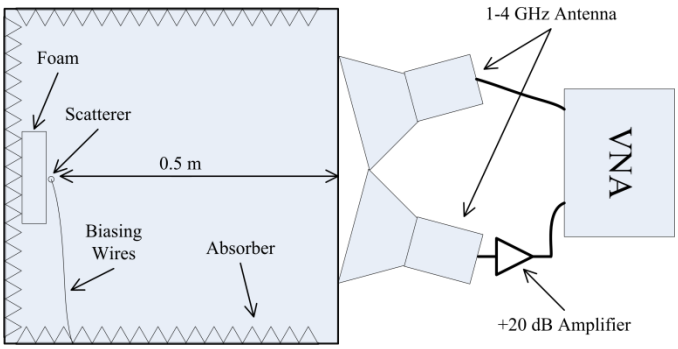

Figure 4.6. Schematic of measurement setup used when measuring the scattered fields of the MST scatterers.

The horn antennas were each connected to a calibrated port of an Agilent 8753E Vector Network Analyzer (VNA), as shown in Figure 4.8. Swept-frequency (1.5 to 3.5 GHz) measurements of the complex transmission coefficient, S21 (related to $|E_s|$), were made. A bistatic setup (shown in Figure 4.6) was chosen for better measurement sensitivity, since the scattering from the DUT is relatively weak. More specifically, a bistatic setup allows for the inclusion of a low noise pre-amplifier (+20 dB gain) at the receiving port (shown in Figure 4.8), which increases the signal to noise ratio (SNR) of the measurement. Additionally, the transmission uncertainty (i.e., S21 error) of the VNA is much lower than the reflection uncertainty (i.e., S11 error) when measuring small signals [46]. Recall from Section 3, that the response of the scatterer may vary with the angle of observation (as shown in Figure 3.19). For this reason, the horn antennas were placed very close together in order to approximate a monostatic measurement (described

by Figure 3.17) in order to attain better correlation between measured (bistatic) and simulated (monostatic) responses of the scatterers. However, before the measured results can be analyzed, consideration must be given to the differences between the measurement setup and the simulations.

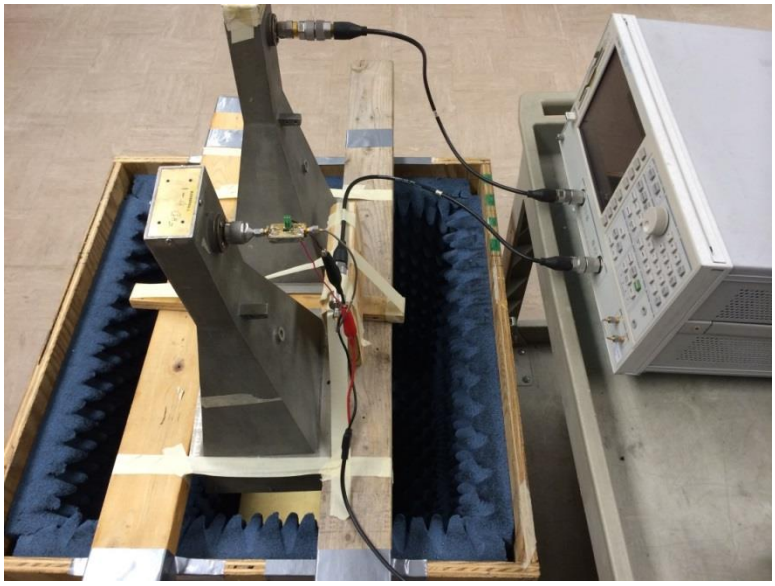

Figure 4.7. VNA connected to the horns radiating into the semi-anechoic chamber.

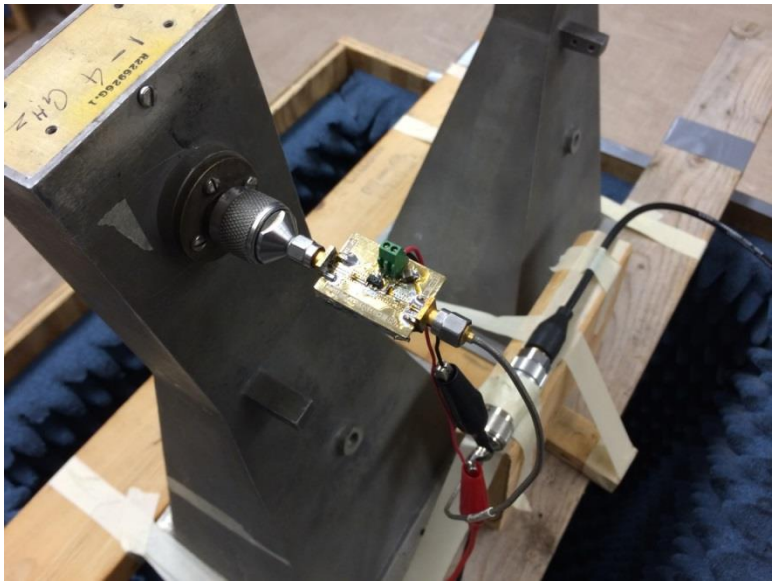

Figure 4.8. Measurement setup: horns, pre-amplifier, and semi-anechoic chamber.

4.2.1. Measurement Considerations. In order to correlate the measured and simulated results, consideration must be given to the differences between the two. First, the distance between the horns and the DUT of 0.5 m was dictated by the size of the available semi-anechoic chamber. This distance (0.5 m) is not in the far-field of the horn antenna (shown in Figure 4.7 and Figure 4.8), which indicates the excitation at the scatterer may not represent a plane wave (relatively uniform phase and magnitude incident along the scatterer). Recall that the simulations (discussed in Section 3) utilized ideal plane wave excitation. However, since the DUT is much smaller than the horn antenna, the field incident on the DUT may still represent a plane wave excitation. To investigate this, CST MWS was used to model the horn antenna and analyze the field distribution (polarized along the length of the scatterer) at a distance of 0.5 m from the aperture. The magnitude and phase for an area approximately the size of the horn aperture at a distance of 0.5 meters from the aperture is shown (at the design frequency of 2.5 GHz) in Figure 4.9. Figure 4.10 shows the magnitude and phase distribution along the DUT (assuming it is centered with respect to the horn aperture) for three different frequencies within the operating frequency range.

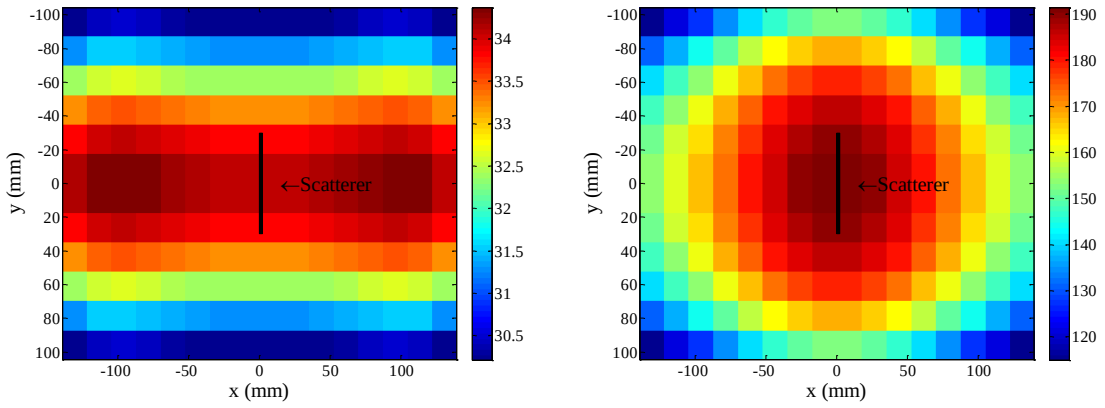

(a) (b)

Figure 4.9. Field from the transmitting horn antenna incident at the DUT (2.5 GHz): (a) magnitude in dBV/m, (b) phase in degrees.

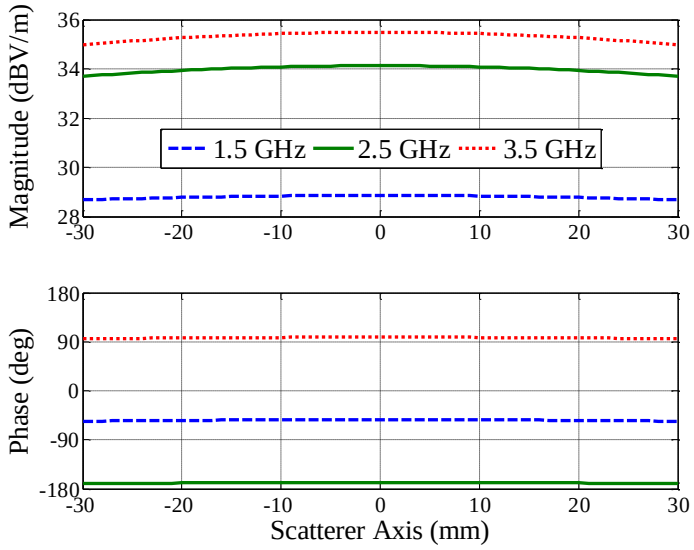

Figure 4.10. Field from the transmitting horn antenna incident at the DUT.

As is evident from Figure 4.9 and Figure 4.10, the measurement setup was able to provide a good approximation to a plane wave excitation (i.e., relatively uniform phase and magnitude along the scatterer) throughout the measured frequency band.

The second aspect to consider is the effect of the frequency response of the receiving horn antenna on the measured response of the DUT. Assuming ideal plane wave excitation (1 V/m) of the DUT (here, the ISLS from Section 3 is used), the subsequent scattering, incident over the aperture of the receiving horn, was simulated. This response was multiplied with the radiated electric field at the horn aperture (determined from the CST MWS simulations of the horn) and integrated over the aperture of the horn. The result was normalized and compared with the simulated result of the DUT (i.e., ISLS scattering), which was also normalized. This comparison is shown below in Figure 4.11. As can be seen from Figure 4.11, the electric field pattern of the horn antenna does not significantly distort the shape of the measured frequency response of the DUT. In fact, there is good agreement between the simulated scattering of the ISLS with and without the horn antenna. It should also be noted that the simulated scattering from the ISLS (DUT) is similar to that shown in Figure 3.5, but calculated at a different distance (0.5 m) and over a wider frequency range.

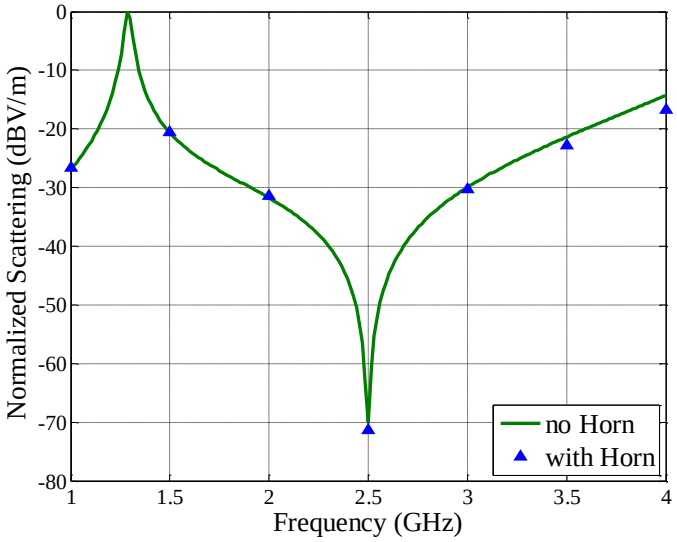

Figure 4.11. Simulated normalized scattering of the ISLS and scattering received by the horn antenna.

The entire measurement setup (shown in Figure 4.6) was not investigated in its entirety by simulation. However, the excitation of the DUT by the fields from the horn antenna was simulated and shown to approximate a plane wave excitation (see Figure 4.10). Additionally, the electric field pattern of the horn was shown to not affect the shape of the DUT's frequency response (shown in Figure 4.11). Therefore, the shape of the frequency response measured (S21) may be directly compared (with the exception of magnitude) to that simulated (discussed in Section 3) for the respective DUT (e.g., ISLS, IDLS, etc.). Therefore, the shape of the frequency response measured (S21) may be directly compared (with the exception of magnitude) to that simulated (discussed in Section 3) for the respective DUT (e.g., ISLS, IDLS, etc.). Note that the mutual coupling between the DUT (i.e., ISLS) and horn is insignificant since the horn is not in the immediate near field of the DUT; hence it was not considered in this investigation.

Another measurement consideration is the separation of the response of the DUT from the ambient scattering that will be present in any measured signal (i.e., S21). For this investigation, coherent background subtraction was utilized to mitigate this issue. To this end, measurements were made of the measurement scene both with and without the presence of a scatterer. In this way, the response of the scatterer may be determined by

coherently subtracting the background measurement from that with the scatterer present. The standard deviation, σ, of the background measurements can then be used to represent the noise floor of the measurement technique. The standard deviation of the background measurements over the operating frequency range is shown below in Figure 4.12.

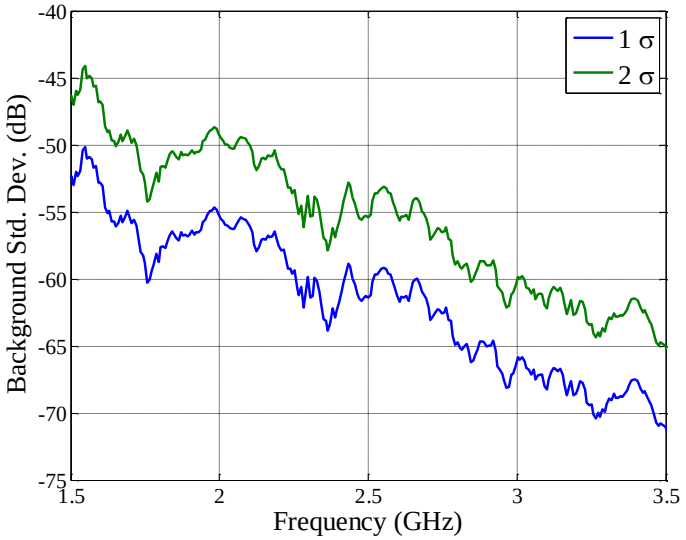

Figure 4.12. Standard Deviation of the Background Measurements (Effective Noise Floor)

Assuming the noise to be Gaussian, ~95% of the noise is contained below the 2σ line while ~68% of the noise is contained below the 1σ line (Figure 4.12) [47]. Each measurement was time averaged (16 samples) which validates the assumption of Gaussian noise distribution due to the central limit theorem [47]. This analysis gives a good idea of the detection limit (i.e., how small of a signal can actually be measured) of this technique. In other words, this analysis provides a limit on how well the "invisible" state of the DUT may be measured.

A last measurement issue to consider involves the additional errors introduced by the presence of the DUT. While the coherent background subtraction technique effectively removes ambient scattering from the measured response of the scatterer, it cannot remove noise sources introduced to the scene by the presence of the DUT. One

example of this is the PIN diode biasing wires attached to the IDLS. This effective noise source is not removed by the coherent background subtraction since the wires are not included in the measurement of the background scene. Due to the biasing wires' small size (36 AWG) and normal orientation to the polarization of the incident electric field (shown in Figure 4.6), the amount of scattering is assumed to be minimal, but may still interfere with the scattering null (i.e. invisible state) of the IDLS response. In order to investigate this issue, various methods were used to mitigate the effect of the biasing wires on the measured results. The effects of the biasing wires will be discussed in more detail in the following Section which presents the measured results.

4.3. RESULTS

4.3.1. ISLS Measurement Results. After coherent background subtraction of the measured S21 data, the resulting response of the ISLS is presented in Figure 4.13.

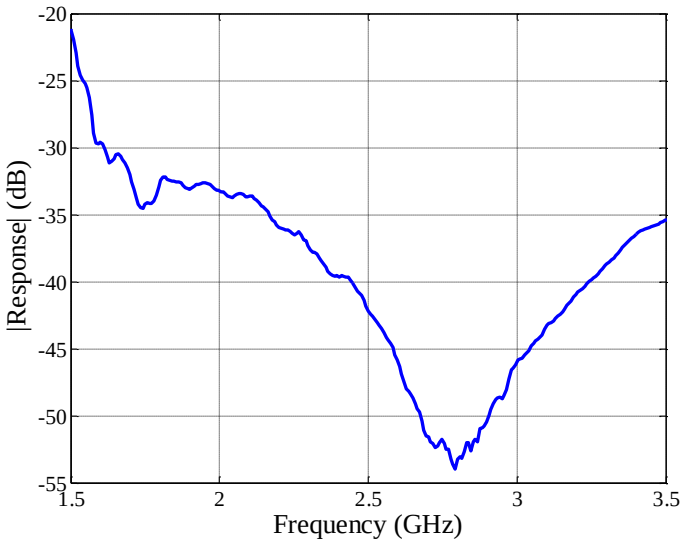

Figure 4.13. Measured response of ISLS.

From Figure 4.13, it is evident that a scattering null similar to that simulated (see Figure 3.5) was obtained. However, the frequency at which the scattering null occurred is slightly shifted from the simulated value (2.5 GHz). This was expected since the load

impedance of the constructed ISLS varied from the impedance used in the simulation (as discussed above). Comparing with the effective noise floor shown in Figure 4.12, it is evident that the measured scattering null is approximately 5 dB above the noise. Recall that the collocated IDLS was designed to perform as an ISLS during the REV state of the diode. Hence, this response (Figure 4.13) represents (without the slight shift from 2.5 GHz) the desired response of the IDLS during the REV state of the diode, which is discussed next.

4.3.2. IDLS Measurement Results. The response of the collocated IDLS after coherent background subtraction of the measured S21 data is presented in Figure 4.14a. For comparison, the traditional SLS response (after coherent background subtraction) is also provided in Figure 4.14b. In an attempt to mitigate the effect of the biasing wires (discussed above), one set of measurements was made using absorber material to cover approximately half of the exposed biasing wires in the anechoic chamber. The results are also included in Figure 4.14a for comparison.

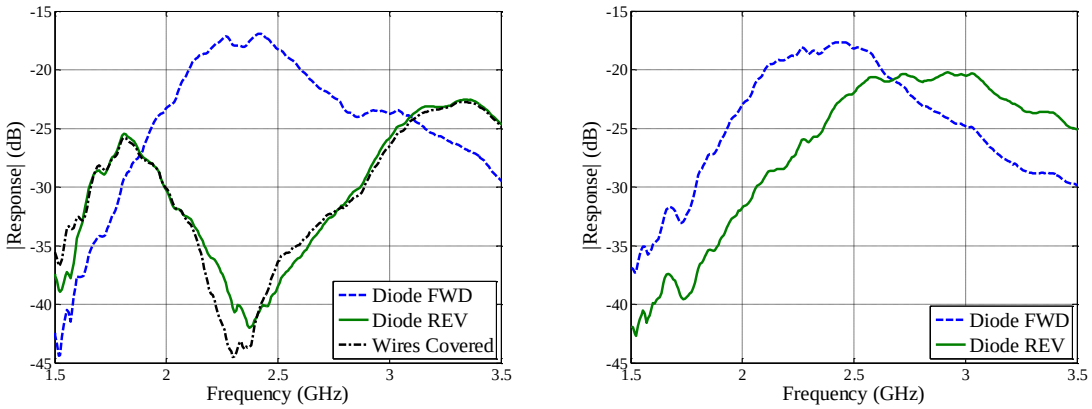

Figure 4.14. Measured response: (a) collocated IDLS, (b) traditional SLS.

Upon comparison of the results presented in Figure 4.14, it is immediately evident that the IDLS (Figure 4.14a) results in a significant improvement to the MD as compared to the traditional SLS (Figure 4.14b) at the design frequency of 2.5 GHz. More specifically, the IDLS achieves an MD of 82%, whereas an MD of 21% is achieved using

the traditional SLS. As expected, the scattering null (i.e., invisible state) was slightly shifted from the design frequency, which is attributed to variations in the inductor values (discussed above). That is to say, the maximum MD for the IDLS of 88% occurred at 2.37 GHz. Additionally, by reducing the scattering from the diode biasing wires (i.e., partially covering the wires with absorbing material), a slightly better MD of 91% (at 2.3 GHz) is achieved (shown in Figure 4.14a). To further illustrate this, Figure 4.15 shows the calculated MD of the collocated IDLS as a function of frequency. The MD for the traditional SLS is also included for comparison.

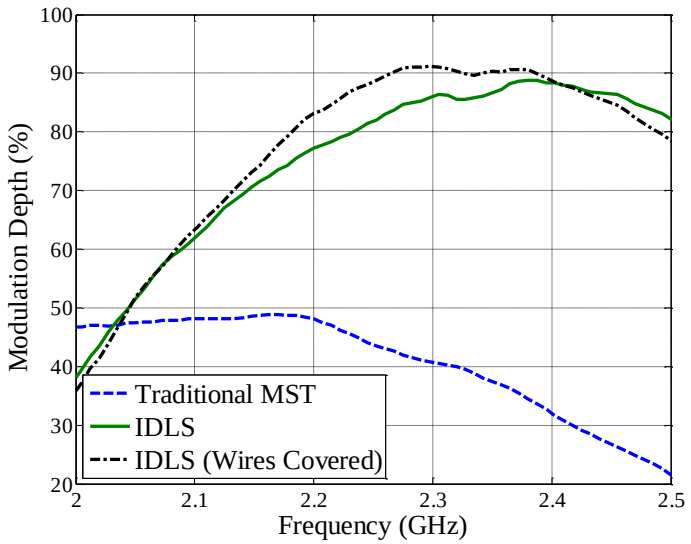

Figure 4.15. Modulation depth of IDLS vs. Traditional SLS.

As can be seen from Figure 4.15, the maximum MD (91%) is achieved at approximately 2.3 GHz with the biasing wires covered. This MD is much better than that of the traditional SLS which never achieves a MD above 50% over the frequency band of interest. Although 91% MD is significant, it is still less than the simulated value for the collocated IDLS presented in Section 3 (99.9%). This difference is attributed in part to the scattering by the small wires used to bias the PIN diode (which is not removed by the coherent background subtraction) which are clearly shown to adversely affect the MD in Figure 4.14 and Figure 4.15. However, due to the fact that the scattering by the PIN diode

biasing wires is a static reflection (i.e., not affected by the PIN diode modulation state), its effect on MD may be removed by further processing or mitigated by different (advanced) measurement techniques.

4.3.3. PCB IDLS Measurement Results. The response of the PCB-based collocated IDLS and traditional SLS (for comparison), after coherent background subtraction, are presented in Figure 4.16. Additionally, Figure 4.16 also displays the simulated results of the PCB-based collocated IDLS from Section 3 for comparison.

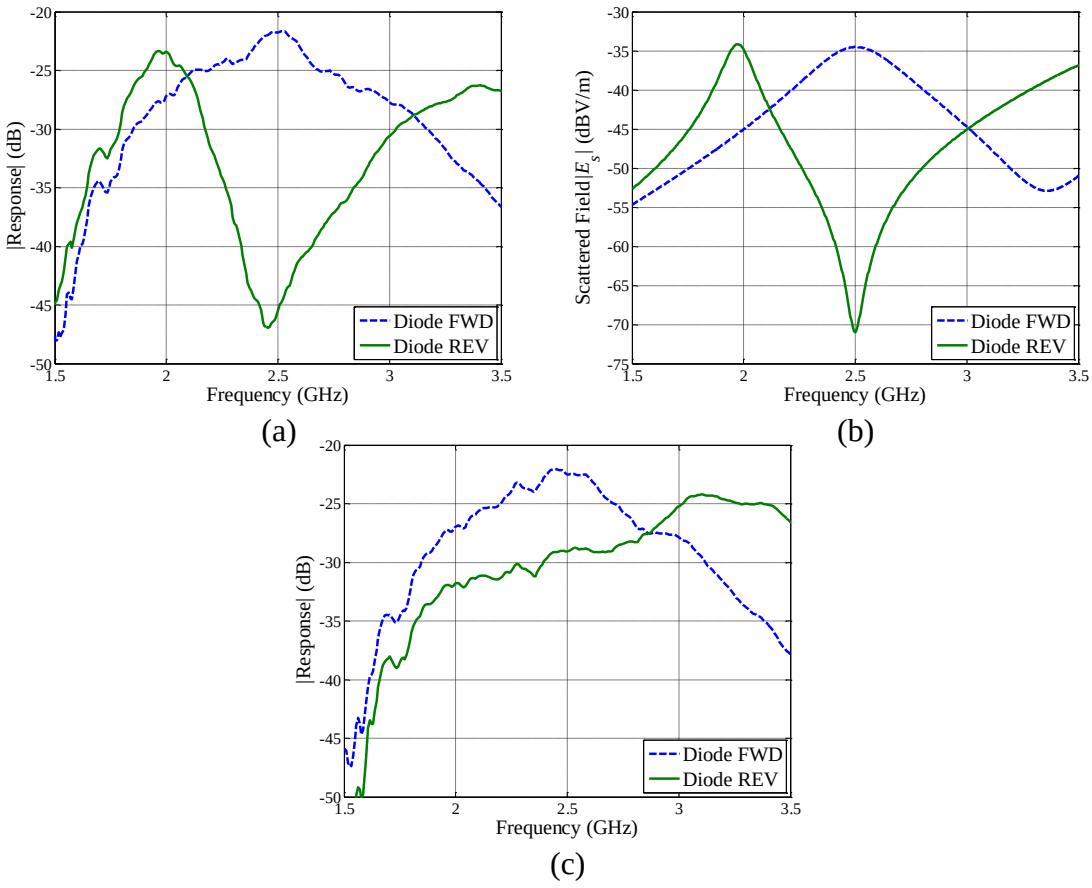

Figure 4.16. Response of PCB-Based Scatterers: (a) measured collocated IDLS, (b) simulated collocated IDLS, (c) measured traditional SLS.

By observing the data given in Figure 4.16, it is evident that the PCB-based collocated IDLS performs better than the PCB-based traditional SLS. The MD, calculated using (1),

of the traditional SLS is 36% while the MD of the IDLS is 88% at 2.5 GHz. This again shows the successful improvement of MD by the inclusion of invisible antenna theory in the design of MST scatterers. Figure 4.16 also shows good correlation between the shape of the measured and simulated response of the collocated IDLS. It should be noted that the magnitudes of these responses are not equivalent, but, as explained above, the shape of the frequency response may be directly compared.

For the PCB-based scatterer measurements, a different technique was used to mitigate the effect of the scattering from the diode biasing wires. For this technique, the wires were included in the background measurement, which was coherently subtracted from the scattering data. In order to achieve this, the wires were secured in the anechoic chamber (see Figure 4.6) and, after the response of the scatterer was measured, the scatterer was cut from the wires and removed from the chamber, leaving the wires in the same position. It should be noted that this is a not a practical solution for mitigating the effect of the biasing wires. The remaining setup (i.e., background including the biasing wires) was measured and subtracted from the measurement containing the scatterer. The effect of the biasing wires (and the removal of their effect) is shown below in Figure 4.17 for the REV state of the diode.

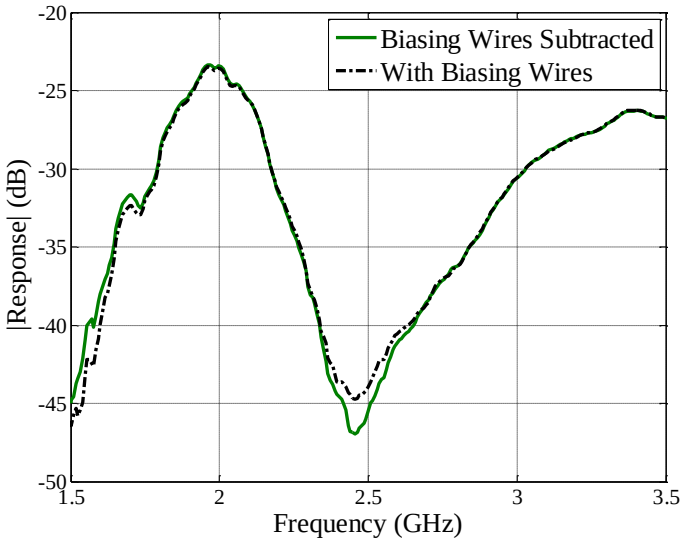

Figure 4.17. Effect of biasing wires on scattering null of the PCB version of the IDLS.

From Figure 4.17, it can be seen that mitigating the effect of the biasing wires results in a deeper scattering null by over 2 dB. This result is consistent with the technique shown in shown in Figure 4.14a (covering the wires with absorber) and indicates that the depth of the scattering null is partly masked by the scattering of the biasing wires. However, even with the partial masking of the deep scattering null, the performance of the IDLS (i.e., MD) is significantly improved as compared to that of the traditional SLS.

4.4. SUMMARY

In this Section, scattering measurements were presented using different versions of MST scatterers; some of which were designed to be electrically invisible during one state of the modulated load (e.g., IDLS). The IDLS was first designed and analyzed by simulations in Section 3. The measured results presented in this Section verified the improvement in the modulation depth of such MST scatterers by comparison to traditional MST scatterer designs (i.e., traditional SLS).

Both wire- and PCB-based IDLS scatterers were fabricated and measured. The response of both IDLS's were then compared to that of the corresponding (wire- or PCB-based) traditional SLS. The measured results indicated that the IDLS design resulted in significant improvements in performance (i.e., MD) over the traditional SLS, as is summarized below in Table 4.1.

Table 4.1. Summary of Modulation Depth

	Modulation Depth	
	IDLS	Traditional SLS
Wire	82%	21%
PCB	88%	36%

Overall, it is evident from Table 4.1 that the new IDLS design significantly improved the MD as compared to a traditional SLS. However, the measurements proved to be quite sensitive to fabrication tolerances (e.g., variations in component values) indicating that precise fabrication methods and components are required to achieve maximum MD (i.e.,

a scattering null) at the frequency of interest. In other words, while Table 4.1 lists the modulation depths achieved at the (intended) design frequency, modulation depths of 90% and greater were achieved during measurements at frequencies slightly shifted from the design frequency. Therefore, with more precise fabrication (e.g., precise inductive loads) the MD achievable by the new designs may exceed that shown in Table 4.1. The scattering from the biasing wires used to modulate the PIN diode were also shown to adversely affect the MD of the measured scatterers. These effects may be mitigated through different measurement or processing techniques. Additionally, further improvement to the MD may be achieved by implementation of other hardware that does not require biasing wires (e.g., optical diodes or local biasing circuit powered by energy harvesting).

5. DISCUSSION AND CONCLUSION

5.1. INTRODUCTION

In this thesis, the theory of electrically invisible antennas [14]-[18] was successfully applied to the design of MST scatterers [5] for the improvement of modulation depth (MD) [9]. In Section 2, electromagnetic simulations based on the Method of Moments (MM) were developed for the purposes of rapid analysis and design of such scatterers. These developed simulations were verified against both the Numerical Electromagnetics Code (NEC) [22]-[23] and CST Microwave Studio® [24] and shown to be accurate. Section 3 presented simulations, performed with the developed MM code, of the scattered fields from both single loaded electrically invisible scatterers (ISLS) as well as new invisible dual loaded scatterers (IDLS). Two new IDLS designs were proposed (i.e., the equidistant and collocated designs discussed in Section 3), both of which were designed to modulate between electrically visible and invisible states, thereby improving the MD. Traditional single loaded scatterers (traditional SLS), representative of traditional MST scatterers (half-wave dipole centrally loaded with a PIN diode), were also simulated for comparison. The simulated results indicated the IDLS (collocated design) capable of achieving 99% MD, while a traditional SLS could achieve nearly 50% MD. Additionally, Section 3 also presents simulations of an IDLS designed for mass fabrication on printed circuit boards (PCBs). The performance of the new PCB-based IDLS design was compared to that of a traditional MST scatterer (half-wave dipole loaded with a PIN diode) and shown to improve performance (i.e., MD). In Section 4, measurements of the ISLS and IDLS were presented and analyzed. The measured results compared well with simulated results, showing scattering nulls (i.e., invisible states) as designed. The measured results of the new IDLS design were compared to measurements of a traditional MST scatterer which verified the performance improvements (i.e., MD) predicted by the simulations. Modulation depths of over 90% were observed for the IDLS, while the traditional SLS achieved approximately 49%. This final Section discusses an additional benefit of the newly designed scatterers (i.e., the mitigation of mutual coupling) and potential future work.

5.2. MUTUAL COUPLING

MST scatterers are often employed in array configurations for rapid antenna testing [8], electric field mapping, imaging, etc. [2]. In such cases, the mutual coupling between elements of different modulation states within such an array can decrease system sensitivity [2] and result in field calculation errors [8]. According to [15], electrically invisible antennas have the potential to reduce the mutual coupling between elements in an array. Therefore, the implementation of the new IDLS (or a similarly-designed element that can become electrically invisible) in an array may mitigate these issues.

In order to investigate this application of the IDLS, the Numerical Electromagnetics Code (NEC) [22]-[23] was used to simulate the input impedance, Z_{in}, of a dipole antenna with a collocated IDLS in close proximity. For this simulation, the PIN diode on the IDLS was in the reverse biased (REV) diode state (i.e., the IDLS is electrically invisible). For comparison, the simulation was also performed using a traditional SLS (also in the REV state). The simulation setup is illustrated in Figure 5.1.

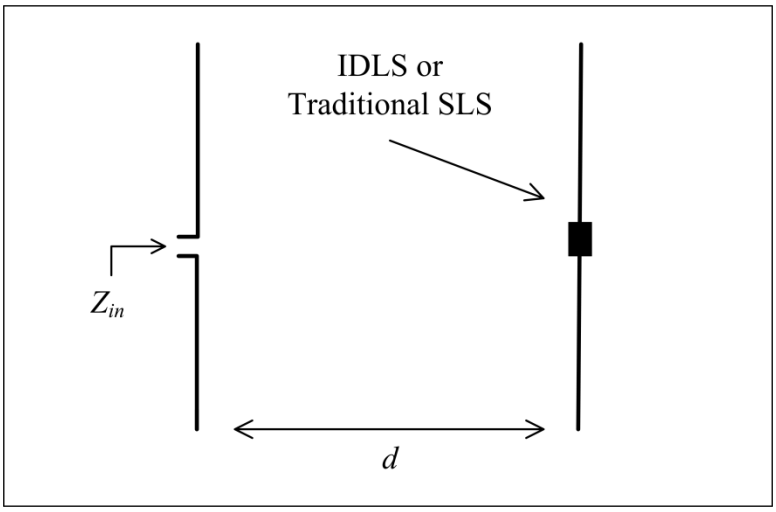

Figure 5.1. Mutual Coupling Simulation.

The dipole input impedance will depend on the nearby MST scatterer (i.e., IDLS or traditional SLS) as well as the separation distance between the two. To illustrate this, the

dipole input impedance was calculated as the separation distance, *d*, between the dipole and the MST scatterer was varied. The results are shown below in Figure 5.2.

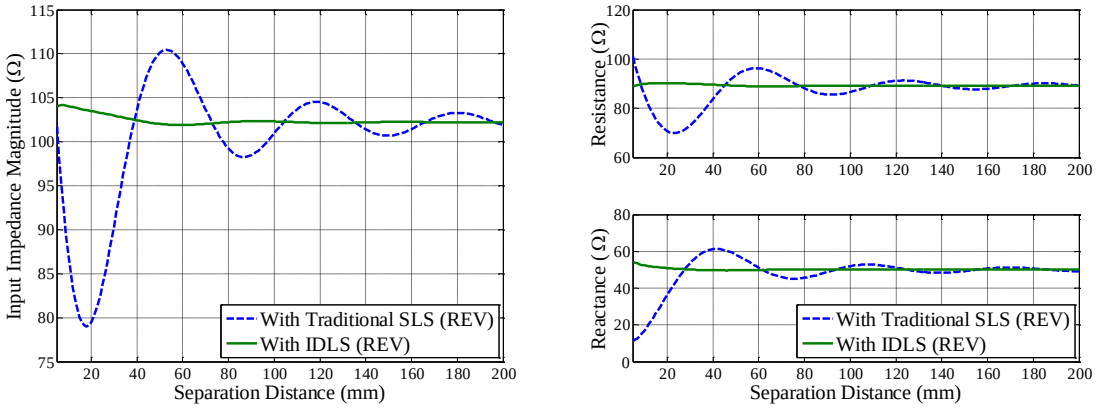

(a) (b)

Figure 5.2. Input impedance of the dipole as a function of separation distance between the MST scatterer: (a) magnitude, (b) resistance and reactance.

As can be seen from Figure 5.2, the effect of the IDLS (during the REV state) on the dipole input impedance is significantly less than that of the traditional SLS (during the REV state), especially for small separation distances. These results indicate the IDLS may have good potential application to MST systems requiring arrays of scatterers (e.g., imaging arrays, etc.). This application may be further investigated and developed in future work on this project.

5.3. FUTURE WORK

The goal of the work presented in this thesis focused on the application of electrically invisible antennas to MST as a means by which the MD of such scatterers may be improved. With this concept successfully shown by simulations and measurements of prototype scatterers, future work will focus on practical improvement and application of such designs.

5.3.1. Improved IDLS Design. As discussed in Section 1, other techniques for the improvement of MST scatterer MD have been developed that focus on increasing scattering during the forward biased state of the modulating load (e.g., PIN diode or photodiode) [10], [13]. The main drawback to these methods, when applied in array applications, is the remaining issue of mutual coupling (discussed above). However, if the two methods could be combined in such a way that the FWD state (i.e., visible state) scattering of the IDLS could be improved/increased (while maintaining the electrical invisibility of the RVS state), the overall performance of the IDLS would also benefit as a result. Improved scattering during the FWD state has been accomplished through various impedance transformation networks connected to the diode [10], [13]. This technique has also been applied to improve performance of radio frequency identification (RFID) tags [11].

5.3.2. Application to RFID. RFID tags are small RF transponders that modulate backscattered signals that are subsequently detected by interrogating systems (tag readers) [48]. The modulated signal backscattered by the tag contains information usually used to identify an object to which the tag is attached [48]. Improving the difference in scattered power between modulation states (related to the MD) of RFID tags has been investigated in [11]-[12] for the improvement of tag performance (e.g., sensitivity). The IDLS design principles discussed in this thesis may have application for improving the MD of RFID tags in some cases. Furthermore, RFID tags are often employed in close proximity to one another where mutual coupling becomes an issue [49]. Therefore, IDLS design techniques may also have application to the design of RFID tags for the mitigation of mutual coupling issues (discussed above).

5.3.3. Energy Harvesting. Another potential improvement to MST, related to RFID techniques, is the inclusion of energy harvesting. When applied to MST, the inclusion of energy harvesting principles allows the scatterer to harvest energy, intended to be used to drive the modulation of the load element, from the interrogating signal [50]. This ability removes the need for biasing wires to control load modulation, which were discussed as source of measurement error in Section 4. Further investigation into the application of energy harvesting methods to the IDLS design is another topic for future consideration.

5.3.4. Potential MST Applications. As stated above, this thesis focused on the concepts of improving the MD of MST scatterers by the integration of electrically invisible antenna theory. A vast area of potential future study is the integration of the IDLS (or similarly constructed scatterers) into existing MST applications. Further research is needed to quantify the possible improvements provided by such a scatterer to specific applications. These application areas include: imaging arrays, RFID (discussed above), materials characterization, etc.

For instance, in Section 3 the ISLS design was proposed to have application to materials characterization. As discussed in Section 3, an ISLS was designed for invisibility in cement-based materials (e.g., mortar). If the properties of the surrounding material changed (possibly due to cracks, ingress of moisture, etc.), the ISLS would lose invisibility (become visible). However, this method had several drawbacks; primarily that the response must be *a priori* known in order to detect changes. Conversely, the IDLS does not suffer from such drawbacks due to its modulation capability. As such, the newly-designed IDLS may be better suited to materials characterization (or other embedded sensing applications).

5.4. SUMMARY

A new MST scatterer design which has the ability to modulate between both visible (scattering) and invisible (minimal scattering) states was proposed, simulated, and successfully measured. Simulations showed this new design to be (theoretically) capable of achieving 99.9% modulation depth. Measurements showed a maximum modulation depth of 91%. This discrepancy is partially attributed to the measurement technique which included the effects of the load (PIN diode) biasing wires. Performance may be improved with more precise measurement techniques. However, achieving the maximum theoretical result is unlikely due to losses in practical implementations (e.g., finite conductivity of the scatterers) which were not taken into account by the simulations. Even so, the new design was shown to significantly improve modulation depth (91%) when compared to that achieved by a traditional MST scatterer (50%). Overall, the new design has shown significant improvement of MD and reduction of mutual coupling (for MST array configurations). Additionally, as discussed above, this new scatterer design

may find application in MST array configurations, RFID tag designs, and materials characterization.

APPENDIX A.
LOADED DIPOLE MATLAB® CODE

```
classdef LoadedScatterer < handle
    %LOADEDSCATTERER Simulate an arbitrarily loaded linear scatterer.
    %   Version 2.0
    %   This object can be used to simulate the scattered fields from an
    %   arbitrarily loaded linear (thin-wire) scatterer. The input
    %   impedance, current distribution, and the RCS can also be computed.
    %
    % References
    % [1] Electromagnetic Waves and Antennas - Orfanidis
    % [2] Field Computations by Moment Methods - R. F. Harrington
    % [3] Antenna Theory 3rd ed. - Balanis
    % [4] Approximations for Terms Related to the Kernel in Thin-wire
    %     Integral Equations - Poggio & Adams
    % [5] Numerical Solution for the Near and Far Fields on an Annular Ring
    %     of Magnetic Current - TSAI
    % [6] Numerical Electromagnetics Code (NEC) - Burke & Poggio
    % [7] Advanced Engineering Electromagnetics - Balanis
    %
    % Updates
    % 20131112 Revised: Version 2.0
    % 20140220 Removed "-" sign from voltage in the magnetic frill
    %          function. Instead the "-" sign is applied to the voltages
    %          sent to the function for better readability.
    % 20140325 Removed all unused or in development code for publishing.
    %
    % Bug Fixes
    % 20140220 There was an error in the calculation of the fields
    %          scattered by the dipole which were fixed to match [7].
    %
    % Copyright 2014 Dylan Crocker
    % The code contained in this file may not be reproduced or used without
    % the express writen permission of the author.
    %

    %% Properties

    properties
        % These are properties that can be set by the user

        % Simulation parameters
        Er = 1           % Relative permativity (complex)
        Freq_Hz = 2.5e9  % Simulation Frequency (must be a scalar)
        Rd_m = 1         % Distance from scatterer to observation point |R|
        IncidentAngle_d = 0      % Excitation incidence angle
        ObservationAngle_d = 0   % Observation angle
        PolarizationAngle_d = 0  % Exitation planewave polarization

        % Note on geometrical settings:
        % Rd_m is the total distance from the center of the scatterer
        % (0,0,0) to the observation point (rho in spherical coordinates).
        % The incident and observation angles are essentially theta in
        % spherical coordinates only 0 is theta = 90. They both ohave a
        % range of +90 degrees to -90 degrees. Remember the scatterer sits
        % on the z-axis. The polarization angle of the incident plane wave
        % is defined as the angle between the E-field vector of the plane-
        % wave and the z-axis (on which the scatterer sits). So a
        % polarization angle of 0 means the E-field is polarized along the
        % z-axis.

        % Scatterer Properties
        ScatterLength_m = 0.0625
        ScatterRadius_m = 0.0002025
        LoadOffset = 0
        LoadZ = [1e-10;  % Colums are loads; rows are states
                 1e10]

        % Solver Settings
        Segments = 0         % Number of mesh segments
        Kernel = 'x'         % Kernal type
        Basis = 't'          % Current expansion (basis) function
        IntAlg = 'l'         % Integration algorithim
```

```
    Adaptive = 1;        % Adapt the mesh for convergence
    MinSegments = 5      % Minimum number of mesh segments (adaptive)
    Silent = 0;          % Suppress certian output messages.

end

properties (Constant)
    kU0 = pi*4e-7                           % Permeability (freespace)
    kE0 = 8.85418782e-12                    % Permitivtty (freespace)
    kC0 = 1/sqrt((pi*4e-7)*(8.85418782e-12)) % Speed of Light (vacuum)
    kKW = 2*pi                              % Wave Number (wl)
end

properties (SetAccess = protected)
    % These properies contain essential simulation data as the
    % calculations are performed. They are availible for get access to
    % the user for more information or perhapse a full calculation is
    % not required (e.g. maybe they only want Zin and not Ez or RCS).
    Dz_w       %
    Zn_w       %
    Zm_w       %
    Zaxis      %
    Zindex     %
    ZMAT       %
    Zin        %
    Yss        %
    Yst        %
    Eincident  %
    Iinduced   %
    states     %
    Eloads     %
    Iloads     %
    Itotal     %
    Etotal     %
    EAz        %
    RCS        %
end

properties (Dependent, SetAccess = protected)
    ETA               % Intrinsic impedance of the medium (ohms)
    VP                % Velocity (m/s)
    Freq_Ang          % Angular frequency (rad/s)
    Lambda_m          % Wavelength (meters)
    ScattererLen_w    % Scatterer Length (wl)
    ScattererRad_w    % Scatterer Radius (wl)
    ObsAngle_rad      % Observation angle
    NumLoads          % Number of loads on the scatterer
    NumCombos         % Number of unique load state combinations
end

%% Constructor, Getters, and Setters
methods

    function set.ScatterLength_m( self, value)
        if (value <= 0), error('Invalid length.'); end;
        self.ScatterLength_m = value;
    end

    function set.ScatterRadius_m( self, value)
        if (value <= 0), error('Invalid radius.'); end;
        self.ScatterRadius_m = value;
    end

    function set.Freq_Hz( self, value )
        if ~isscalar( value )
            error('Simulation frequency must be a scalar value.');
        end
        self.Freq_Hz = value;
    end

    function set.Segments( self, N )
```

```
    if mod(N,2) == 0, N = N + 1; end % Ensure "segements" is odd.
    self.Segments = N;
end

function set.MinSegments( self, N )
    if N < 5, N = 5; end
    if mod(N,2) == 0, N = N + 1; end % Ensure N is odd.
    self.MinSegments = N;
end

function set.Basis( self, value )
     if ((value(1) ~= 't') && (value(1) ~= 'p'))
         error('Invalid Basis function selection')
     end
     self.Basis = value;
end

function set.Er( self, value )
    if (imag(value) > 0)
        error('Really? An energy creating material????');
    end
    self.Er = value;
end

function set.LoadZ( self, value )
    if ~ismatrix(value),
        error('LoadZ must be a matrix input (cols = load state)');
    end
    if isvector(value), value = value(:); end
    if isscalar(value)
        self.LoadZ = [value; value];
    else
        self.LoadZ = value;
    end
end

function set.LoadOffset( self, value )
    if ~isvector(value),
        error('LoadOffset must be a vector input.');
    end
    % Stay on the antenna!!
    value(abs(value) > 50) = 50*sign(value(abs(value) > 50));
    self.LoadOffset = value(:);
end

function ETA = get.ETA( self )
    ETA = sqrt(LoadedScatterer.kU0/ ...
          (LoadedScatterer.kE0*self.Er));
end

function VP = get.VP ( self )
    VP = LoadedScatterer.kC0/sqrt(real(self.Er));
end

function Freq_Ang = get.Freq_Ang( self )
    Freq_Ang = 2*pi*self.Freq_Hz;
end

function Lambda_m = get.Lambda_m( self )
    Lambda_m = self.VP ./ self.Freq_Hz;
end

function ScattererLen_w = get.ScattererLen_w( self )
    ScattererLen_w = self.ScatterLength_m ./ self.Lambda_m;
end

function ScattererRad_w = get.ScattererRad_w( self )
    ScattererRad_w = self.ScatterRadius_m ./ self.Lambda_m;
end

function ObsAngle_rad = get.ObsAngle_rad( self )
```

```
        ObsAngle_rad = self.ObservationAngle_d*pi/180;
    end

    function NumLoads = get.NumLoads( self )
        NumLoads = size(self.LoadZ,2);
    end

    function NumCombos = get.NumCombos( self )
        % Number of unique load state combinations (2 states per load).
        % Do not use self.numloads to avoid method call overhead.
        NumCombos = 2^size(self.LoadZ,2);
    end

end

%% These are the visible worker methods.
methods (Access = public)

    function S = momSolver( self )

        S = 0; % Status flag to return
        buff_size = 5;

        % If the adaptive mesh flag is set refine the mesh until Zin
        % converges. Otherwise run the solver once with the current
        % mesh settings.
        if (self.Adaptive)

            % Start the mesh at the minimum number of segments.
            self.Segments = self.MinSegments;

            err = -999;
            convergence_flag = 0;
            iteration_count  = 0;
            buffer = zeros(1,buff_size);
            while (~convergence_flag)

                iteration_count = iteration_count + 1;

                % Mesh the scatterer.
                mstat = self.mesh();

                % If the mesh is set to high and the adaptive solver
                % has not refined the mesh enough times to fully test
                % convergence the minimum number of segments
                % (starting segments) is to high.
                if (mstat && (iteration_count <= buff_size)),
                    error('Minimum segments set to high.');
                end

                % If the mesh is still having an error after enough
                % iterations to test convergence then tell the user
                % that convergence is impossible.
                if (mstat && (iteration_count > buff_size)),
                    m = 'Could not converge. ';
                    error([m 'Current error: ' num2str(err*100) '%']);
                end

                % Create the Z-Matrix to solve Pocklington.
                self.zmat();

                % Solve for Zin.
                self.zin();

                % Check for convergence
                buffer = [self.Zin(1) buffer(1:buff_size - 1)];
                if iteration_count >= buff_size,
                    err = abs(std(buffer)/abs(mean(buffer)));
                    convergence_flag = err < 0.005;
                end
```

```
                % Update the Segments setting if necessary
                if ~convergence_flag,
                    self.Segments = self.Segments + 2;
                    if ~self.Silent,
                        s = num2str(self.Segments);
                        disp(['Refining Mesh: ' s ' segments']);
                    end
                end

            end

        else

            % If the adaptive meshing is disabled just run through with
            % the current settings.
            mstat = self.mesh();
            if (mstat),
                error('Segments set to high for kernel validity.');
            end
            self.zmat();
            self.zin();

        end

    end % END momSolver

    function S = solve( self, RCS )
        momSolver(self);
        yparams(self);
        eLoadZ(self);
        eFields(self);
        if RCS, rcs(self); end
        S = 0; % Update later to return a useful status byte
    end % END solve

end

%% These are private worker methods.
methods (Access = protected)

    function S = mesh( self )
        % Mesh the scatterer into segments for the solver.

        S = 0; % Status flag to be returned.

        % Set the variables here so the getters are only called once.
        lw = self.ScattererLen_w; % Units: wl
        aw = self.ScattererRad_w; % Units: wl
        N  = self.Segments;       % Mesh segments (always odd).

        % Find dz
        if(self.Basis == 't')
            % In order to use a triangle Basis function the antenna
            % must be divided up into one less segment.
            dzw = lw/(N-1); % wavelengths
        else
            % For Pulse basis functions.
            dzw = lw/N; % wavelengths
        end

        % Check the validity of the kernel.
        % Adapt the kernel if using the adaptive solver.
        % See [4] for more information.
        if     ((dzw/aw < 10) && (self.Kernel(1) == 'a'));
            disp('Mesh to fine for Approximate Thin-Wire Kernel.');
            S = 1;
            if (self.Adaptive)
                disp('Attemtpting the Extended Thin-Wire Kernel.');
                self.Kernel = 'x';
                S = 0;
            end
```

```
    end
    if ((dzw/aw <  2) && (self.Kernel(1) == 'x'));
        disp('Mesh to fine for Extended Thin-Wire Kernel.');
        % if (self.Adaptive)
        %     disp('Attemtpting the Exact Thin-Wire Kernel.');
        %     self.Kernel = 'e';
        % end
        S = 1;
    end

    % Create array of source sample points
    M = (N - 1)/2;
    m = linspace(-M,M,N);
    zmw = m*dzw;

    % Create array of observation points
    znw = m*lw/N;

    % Only call the setters once.
    self.Dz_w = dzw;                % units: wl
    self.Zm_w = zmw(:);             % <- col vector (units: wl)
    self.Zn_w = znw(:);             % <- col vector (units: wl)
    self.Zaxis = zmw*self.Lambda_m; % Z axis vector (units: m)

    % Determine at which segment the "source" is located (index).
    if size(self.LoadOffset) ~= size(self.LoadZ),
        error('Offsets must be specified for each load.');
    end

    % Now change the load location into units of wavelength from
    % percent length
    x = (self.LoadOffset./100)*self.ScatterLength_m/self.Lambda_m;

    % Determine at which segment the "source" is located (index).
    loc = ceil(self.Segments/2) + round(x/self.Dz_w);
    self.Zindex = loc(:);

end % END mesh

function S = zmat( self )

    % Determine the evaluation space of the impedance matrix.
    [X,Y] = meshgrid(self.Zm_w,self.Zn_w);
    space = Y-X;

    % Determine the limits of integration depending on the choice
    % of current expansion (basis) function.
    if    (self.Basis(1) == 't'), delta = self.Dz_w;
    else                          delta = self.Dz_w/2; % pulse
    end

    % Function pointer to the kernel and basis function.
    fun = @(z)kernelBasis(self,space,z);

    % Lets also be able to choose the integration algorithim...
    if (self.IntAlg == 'q'), zs = quadv(fun,-delta,delta);
    else zs = integral(fun,-delta,delta,'ArrayValued',true); end

    self.ZMAT = zs;  % Set the property.
    S = 0;           % Status flag to be returned.

end % END zmat

function I = kernelBasis(self, space, z)
    % This function returns the argument for the integrand. It is
    % the kernel (with the differential operator applied
    % analytically) multiplied by the basis function for that
    % point.

    G = kernel(self,space - z);
    B = basis(self,space,z);
```

```
    I = B.*G;

end % END kernelBasis

function G = kernel(self, space)
    % Evaluate the kernel for the given solution space.
    % Note: The (d^2/dz^2 + k^2) operator is applied analytically.

    k = self.kKW;
    a = self.ScattererRad_w;
    zvals = space;
    type = self.Kernel;

    if     type == 'a'
        % Approximate Thin-Wire Kernal (See pg.446 [3])
        R = sqrt(zvals.^2 + a^2);
        G = exp(-1j*k*R)./(R.^5).*( ...
          (1 + 1j*k*R).*(2*R.^2 - 3*a^2) + (k*a*R).^2);
    elseif type == 'x'
        % Extended Thin-Wire Kernel (See my documentation and [4])
        R = sqrt(zvals.^2 + a^2);
        G = (exp(-1j*k*R)./(16*pi*R.^9).*( ...
          8*R.^6.*(1 + 1j*k*R) + ...
          12*a^2*R.^4.*(-3 + k*R.*(-3j + k*R)) + ...
          8*a^4*R.^2.*(15 + k*R.*(15j + k*R.*(-6 - 1j*k*R))) - ...
          a^6*(105 + k*R.*(105j + k*R.*(-45 + k*R.*(-10j+k*R))))));
    end

end % END kernel

function B = basis(self, space, z)

    B = zeros(size(space));
    if self.Basis(1) == 'p',
        % Pulse basis
        B = ones(size(B));

    elseif self.Basis(1) == 't',
        % Triangle basis
        % See [1] for more information.
        dz = self.Dz_w;
        B = ones(size(B))*(1-abs(z)/dz);
    else
        error('Invalid basis function selection.')
    end

end % END basis

function zin(self)
    % Calculate the input impedance at the terminals where the
    % loads connect. Note: when multiply loaded the input impedance
    % calculated here is calculated with the other ports shorted.
    % This results in a simple calculationa nd a vlaue that can
    % easily be converted to input admittance which is necessary
    % for the rest of the simulations. The Zin vector is NOT
    % Z-paramters! Maybe change this to yin later to avoid such
    % confusion?

    loc = self.Zindex;

    % Drive the antenna with a -1V source at each port and
    % determine the input impedance/admittance for each port.
    % Negative sign used here due to the definition of the current
    % as flowing in the +z direction while a positive input voltage
    % would define current flowing in the -z direction.
    v = -ones(self.NumLoads,1);

    % Calculate the impressed electric field (V/wl) along the
    % antenna from the -1V source at the location(s) of the load.
    Ei = mFrill(self,v);
```

```
    Ii = zeros(size(Ei));
    self.Zin = zeros(length(loc),length(loc));
    for n = 1:length(loc),

        % Calculate the effective current by solving Pocklington's
        % equation using the impressed E-field as the source.
        Ii(:,n) = iDist(self,Ei(:,n),'w');

        % Calculate the impedance for each port on the antenna/
        % scatter. Antenna (Scatterer) only - no incident fields.
        self.Zin(n,:) = v(n)./(Ii(loc,n).');

    end

end % END zin

function [Ew,Em] = mFrill(self, v)
    % [Ew,Em] = mfrill(self, v)
    %    Calculates the impressed electric filed on a dipole
    %    antenna from a voltage source using the magnetic-frill
    %    generator [5].
    %
    %    INPUTS
    %    v   - source voltage (V), this can be a vector.
    %
    %    REQUIRED - obtained by object properties
    %    loc - index of zm representing the antenna segment at
    %          which the source is located. This should be a vector
    %          of same length as v represnting the locations of the
    %          sources represented in v.
    %    lambda - wavelength (m) cooresponding to the simulation
    %             fequency and material.
    %
    %    OUTPUTS
    %    Ew - Column vector representing the impressed E-field
    %         (V/wavelengths) caused by the specified voltage
    %         source(s).
    %    Em - Column vector representing the impressed E-field
    %         (V/m) caused by the specified voltage source(s).
    %
    %    Notes: Assumes b/a = 2.3. This method implements the
    %           magnetic frill calculation which assumes the
    %           observation points are at the center of the wire
    %           (see [5]).
    %
    %    Dylan Crocker 11-09-13
    %

    loc = self.Zindex;
    if size(loc) ~= size(v),
        error('Must specify voltage at each location.');
    end

    k = self.kKW;            % Wave number (1/wl)
    a = self.ScattererRad_w; % Wire radius (wl)
    zn = self.Zn_w;          % Observation points (E-field points)

    % Determine the size of the magnetic frill given b/a = 2.3.
    b = 2.3*a;

    % Calculate the E-field from the "source".
    Ew = zeros(length(zn),length(loc));
    Em = zeros(length(zn),length(loc));
    for n = 1:length(loc)
        % Create vectors that represent the distance from the
        % source (load)location to the a and b of the magnetic
        % frill disk for each evaluation point on the antenna.
        Ra = sqrt((zn-zn(loc(n))).^2 + a^2);
        Rb = sqrt((zn-zn(loc(n))).^2 + b^2);
        Ga = exp(-1j*k*Ra)./Ra;
        Gb = exp(-1j*k*Rb)./Rb;
```

```
            Ew(:,n) = v(n)/(2*log(2.3))*(Ga - Gb); % V/wl
            Em(:,n) = Ew(:,n)/self.Lambda_m; % V/m
        end

    end % END mFrill

    function I = iDist(self, E, unit)
        % I = currentDistribution(self,Z,E)
        %    Calculate the current distribution from the impedance
        %    matrix and the incident or impressed electric field.
        %
        %    INPUTS
        %    E    - Incident or impressed E-Field
        %    unit - Units of E ('w' = V/wl, 'm' = V/m)
        %
        %    OUTPUT
        %    I  Current distributed along the dipole in Amps.
        %
        %    Dylan Crocker 20131109
        %

        if unit(1) == 'w', eps = self.kE0*self.Lambda_m; % F/wl
        else               eps = self.kE0;               % F/m
        end
        w = self.Freq_Ang;

        % Calculate the right side of the Pocklington equation.
        V = -1j*w*eps*E;

        % Calculate the current distribution...
        I = self.ZMAT\V;

    end % END iDist

    function yparams(self)
        % Find the Y-Parameters for the network.

        self.Yss =  1./self.Zin; % Should already have calculated Zin

        % Calculate current induced by a plane wave on the scatter
        % if it had no loads.

        % Field strength of 1 V/m (See Pozar page 36)
        Et = ones(self.Segments,1)*cosd(self.PolarizationAngle_d) ...
             *cosd(self.IncidentAngle_d).*exp(1j*self.kKW*self.Zn_w ...
             *sind(self.IncidentAngle_d));
        Et = Et*self.Lambda_m; % V/wavelength
        self.Eincident = Et;

        % Calculate the current distribution induced by the incident PW.
        It = iDist(self,Et,'w'); % iDist with E in V/wavelength
        self.Iinduced = It;

        % Calculate the tranciever/scatter admittances.
        Vt = 1; % We set Vt (or Vr) to 1 for simplicity.
        self.Yst = It(self.Zindex)/Vt;
        self.Yst = self.Yst(:); % column vector ([2] pg. 123)

    end % END yparams

    function eLoadZ(self)
    % Determine the E-Field caused by the voltages at the loads

        % Define the admittances of the loads for all combinations of
        % load states.
        yLoadZ = 1./self.LoadZ;

        nlds = self.NumLoads;   % Number of loads
        ncmbs = self.NumCombos; % Number of unique load state
                                %  combinations (2 states per load)
```

```
    % Use binary numbers to get indexes
    bstr = dec2bin(0:ncmbs-1,nlds);

    % Transform the binary numbers (as an array of characters) into
    % a matrix for indexing.
    ndex = reshape(str2num(reshape(bstr',[],1))',nlds,ncmbs).'+1;
    self.states = ndex;

    Yz = zeros(nlds,nlds,ncmbs);
    Ytemp = zeros(1,nlds);
    Veff = zeros(nlds,ncmbs);
    Eload = zeros(length(self.Zn_w),ncmbs);
    Iload = zeros(size(Eload));
    for k = 1:ncmbs

        % Assemble the unique state combinations.
        for m = 1:nlds, Ytemp(m) = yLoadZ(ndex(k,m),m); end
        Yz(:,:,k) = diag(Ytemp);

        % Determine the effective voltages at the ports from which
        % to generate an equivalent impressed E-field.
        Veff(:,k) = -(self.Yss+Yz(:,:,k))\self.Yst;

        % Combine E from each load/source
        Eload(:,k) = sum(mFrill(self,Veff(:,k)),2);

        % Calculate the current caused by the fields (Optional)
        Iload(:,k) = iDist(self,Eload(:,k),'w');

    end

    self.Eloads = Eload; % Save to property for later access.
    self.Iloads = Iload;

end % END eLoadZ

function eFields(self)
    % Calculate scattered fields for each load state.

    % Calculate the total current induced on the scatterer from
    % the combination of the incident and equivelent impressed
    % fields (effect of the loads). Then calculate the scattered
    % field from the total current distribution.
    self.Etotal = zeros(size(self.Eloads));
    self.Itotal = zeros(size(self.Iloads));
    self.EAz = zeros(size(self.Eloads,2),1);
    for n = 1:size(self.Eloads,2)
        self.Etotal(:,n) = self.Eincident + self.Eloads(:,n);
        self.Itotal(:,n) = iDist(self,self.Etotal(:,n),'w');
        self.EAz(n) = scatteredFields(self,self.Itotal(:,n));
    end
end % END eFields

function E = scatteredFields(self, I)

    lambda_m = self.Lambda_m;     % (meters)
    dz = self.Dz_w*self.Lambda_m; % (meters)
    zm = self.Zm_w*self.Lambda_m; % (meters)
    Rd = self.Rd_m;               % (meters)
    oAngle = self.ObsAngle_rad;   % (Radians)

    km = 2*pi/lambda_m;   % (m^-1)
    z = Rd*sin(oAngle);   % meters
    rho = Rd*cos(oAngle); % meters
    R = sqrt(rho^2 + (z - zm).^2); % <- vector (meters)

    % Calculate contributions to the E-Field from each wire
    % segment (See [7] pg 284).
    G1 = (-1-(1j*km*R)+(km^2*R.^2))./(R.^3);
    G2 = (3+1j*3*km*R-km^2*R.^2)./(R.^5);
    K = 1j*self.ETA/(4*pi*km);
```

```
            E = K*(I).*(G1 + G2.*(z - zm).^2).*exp(-1j*km*R);

            % Integrate contributions to the E-field along the wire.
            E = trapz(E)*dz;

        end  % END scatteredFields

        function rcs( self )
             % Calculate the radar cross-section (RCS) of the scatterer.
             if(~isFarField(self))
                 disp('Unable to calculate RCS (Not in the Far-Field).');
                 return;
             end
             self.RCS = 4*pi*self.Rd_m^2*abs(self.EAz).^2;
        end % END rcs

        function F = isFarField( self )
            % Ensure the observation distance is in the far field.
            if self.ScattererLen_w <= 0.5,
                F = (self.Rd_m >= (10*self.Lambda_m));
            else
                % 2D^2/wl => 2D^2*wl if D is in units of wl.
                F = (self.Rd_m >= 2*self.ScattererLen_w^2*self.Lambda_m);
            end
        end % END isFarField

    end

end
```

APPENDIX B.
EXAMPLE SIMULATION

```
% This script is an example usage of the developed loaded dipole MM simulations.
% It is setup to do a frequency sweep of a single loaded scatter (half-wave
% dipole centrally loaded with a PIN diode).

close all; clear all; clear classes; clc;

%% Initialize and setup the loaded scatterer object.

d = LoadedScatterer();
d.Freq_Hz = 2.5e9;
d.Er = 1;
d.ScatterLength_m = 0.5*d.Lambda_m;
d.ScatterRadius_m = 0.000511/2;
d.Rd_m = 3;

% Solver settings
d.Segments = 115;
d.Kernel = 'x';
d.Basis = 't';
d.Adaptive = 0;

% Frequency Sweep
f  = linspace(1,4,201)*1e9; f = f(:);
s = 1j*2*pi*f;

%% Setup the load

% Diode
Rd = 1.5;
Ld = 0.6e-9;
Cd = 0.2e-12;
Zd_h = Rd + (s*Ld);
Zd_l = (s*Ld) + (1./(s*Cd));

%% Scatterer Simulation

Idist = zeros(d.Segments,length(f),2);
Ez    = zeros(length(f),d.NumCombos);
RCS   = zeros(size(Ez));

for n = 1:length(f)

    % Calculation per frequency
    d.Freq_Hz = f(n);
    d.LoadZ = [Zd_h(n); Zd_l(n)];
    d.LoadOffset = 0;
    d.solve(1);
    Ez(n,:) = d.EAz;
    RCS(n,:) = d.RCS;
    Idist(:,n,1) = d.Itotal(:,1);
    Idist(:,n,2) = d.Itotal(:,2);

end

%% Plot the results

figure()
plot(f*1e-9,20*log10(abs(Ez(:,1))),'--')
hold all
plot(f*1e-9,20*log10(abs(Ez(:,2))))
xlabel('Frequency (GHz)')
ylabel('|E_s| (dBV/m)')
legend('Diode FWD','Diode REV')
grid on
```

BIBLIOGRAPHY

[1] Bolomey, J.C. and F.E. Gardiol, "Engineering Applications of the Modulated Scatterer Technique," Artech House, Norwood, MA, 2001.

[2] Abou-Khousa, M.A., "Novel Modulated Antennas and Probes for Millimeter Wave Imaging Applications," Ph.D. Dissertation, Electrical and Computer Engineering Department, Missouri University of Science and Technology, Rolla, MO 65409, April 2009.

[3] Hughes, D. and R. Zoughi, "A Novel Method for Determination of Dielectric Properties of Materials Using a Combined Embedded Modulated Scattering and Near-field Microwave Techniques - Part II. Dielectric Property Recalculation", IEEE Transactions on Instrumentation and Measurement, vol. 54, no. 6, pp. 2398-2401, December 2005.

[4] Freiburger, G.S. and R. Zoughi, "Dielectric Material Characterization by Complex Ratio of Embedded Modulated Scatterer Technique States," Proceedings of the IEEE Instrumentation and Measurement Technology Conference, pp. 67-71, Ottawa, Canada, May 16-19, 2005.

[5] Harrington, Roger F., "Small Resonant Scatterers and Their Use for Field Measurements," Microwave Theory and Techniques, IRE Transactions on , vol.10, no.3, pp.165,174, May 1962

[6] Donnell, K. M., M. A. Abou-Khousa, M. Belayneh, and R. Zoughi, "Dual-Loaded Modulated Dipole Scatterer as an Embedded Sensor," IEEE Transactions on Instrumentation and Measurement, vol. 60, no. 5, pp. 1884-1892, 2011.

[7] Donnell, K.M.; Zoughi, R., "Application of Embedded Dual-Loaded Modulated Scatterer Technique (MST) to Multilayer Structures," Instrumentation and Measurement, IEEE Transactions on , vol.61, no.10, pp.2799,2806, Oct. 2012

[8] Bolomey, J.C., et al., "Rapid near-field antenna testing via arrays of modulated scattering robes," IEEE Transactions on Antennas and Propagation, vol. 36, no. 6, pp. 804-814, June 1988.

[9] A.D. Skinner, "Modulation: fundamental techniques for traceability," IEE Colloquium on Accreditation of RF Measurement, pp. 6/1 - 6/6, Feb. 1993.

[10] Bolomey, J.-C.; Memarzadeh-Tehran, H.; Laurin, J.-J., "Optimization of Optically and Electrically Modulated Scattering Probes for Field Measurements," Instrumentation and Measurement, IEEE Transactions on , vol.63, no.1, pp.154,165, Jan. 2014

[11] J.Ch. Bolomey et al., “Electromagnetic Modeling of RFID-Modulated Scattering Mechanism. Application to Tag Performance Evaluation”, Proceedings of the IEEE, vol. 98, no. 9, pp. 1555-1569, Sept. 2010.

[12] P.V. Nikitin, K.V.S. Rao, and R.D. Martinez, “Differential RCS of RFID Tag”, Electronics Letters, vol. 43, no. 8, pp. 431-432, April 2007.

[13] H. Memarzadeh-Tehran, J.-J. Laurin, and R. Kashyap, “Optically modulated probe for precision near-field measurements,” IEEE Trans. Instrum. Meas., vol. 59, no. 10, pp. 2755–2762, Oct. 2010.

[14] Iigusa, K., T. Sawaya, M. Taromaru, T. Ohira, and B. Komiyama, “Experimental Proof of Electrically Invisible State of Inductively Loaded Dipole and Proposal of Electrically Invisible Meander-Lines”, IEEE Transactions on Antennas and Propagation, vol. 54, no. 11, pp. 3374-3382, November 2006.

[15] Iigusa, K., T. Ohira, and B. Komiyama, “An Electrically Invisible Dipole Loaded with a Variable Reactor and Its Applications for a Reconfigurable Antenna”, Electronics and Communications in Japan – Part 1, vol. 89, no. 3, pp. 21 – 35, 2006.

[16] Chen, K.M., and V. Leipa, “The Minimization of the Back Scattering of a Cylinder by Central Loading”, IEEE Transactions on Antennas and Propagation, pp. 576 – 582, 1964.

[17] Iigusa, K., T. Ohira, and B. Komiyama, “An Equivalent Weight Vector Model of Array Antennas Considering Current Distribution along Dipole Elements”, Electronics and Communications in Japan – Part 1, vol. 89, no. 2, pp. 22 – 35, 2006.

[18] Iigusa, K.I., T. Ohira, and B. Komiyama, “Electrically-invisible Parasitic Dipoles for New Reconfigurable Array Antennas,” in Proc. APMC2004, Dec. 2004, p. 694.

[19] Glaser, J.I., “Stealthy Antennas: Minimizing the Radar Cross Section of an Essential Communication System Component”, The WSTIAC Quarterly, vol. 8, no. 2,pp. 11-14.

[20] Iigusa, K., H. Harada, S. Kato, J. Hirokawa, and M. Ando, “Radio-Wave Transparent Surface Containing Lines Loaded with Impedance at Regular Intervals”, IEEE Antennas and Propagation Society International Symposium, pp. 3960-3963, 2007.

[21] Crocker, D.A.; Donnell, K.M., “Application of electrically invisible antennas to the Modulated Scatterer Technique,” Instrumentation and Measurement Technology Conference (I2MTC), 2013 IEEE International , vol., no., pp.392,396, 6-9 May 2013

[22] G. J. Burke and A. J. Poggio, Numerical Electromagnetics Code (NEC) – Method of Moments; Part I: Program Description – Theory, Part II: Program Description – Code, Part III: User's Guide. Livermore, CA: Lawrence Livermore Nat. Lab., Jan. 1981, Rep. UCID-18834.

[23] T. Molteno. (2008). Nec2++. Electronics Group, Department of Physics, University of Otago. [Online]. Jan. 2014, Available: <http://elec.otago.ac.nz/w/index.php/Necpp>

[24] CST – Computer Simulation Technology. <http://www.cst.com>.

[25] C. A. Balanis, Antenna Theory and Techniques: Analysis and Design, 3rd ed. Hoboken: Wiley, 2005.

[26] J. Poggio, and R. W. Adams, "Approximations for Terms Related to the Kernel in Thin-wire Integral Equations," UCRL-51985, Lawrence Livermore Lab., Livermore, CA, Dec. 1975.

[27] Orfanidis, Sophocles J. Electromagnetic Waves and Antennas, Piscataway: ECE Department Rutgers University, 2010. Rutgers University, March 2013, <http://www.ece.rutgers.edu/~orfanidi/ewa/>.

[28] Harrington, R. F, Field Computations by Moment Methods, IEEE Press Series on Electromagnetic Waves, Donald G. Dudley, Series Editor, 1993.

[29] Sarkar, T., "A note on the choice weighting functions in the method of moments," Antennas and Propagation, IEEE Transactions on , vol.33, no.4, pp.436,441, April 1985

[30] G. A. Thiele, "Wire Antennas," in Computer Techniques for Electromagnetics, R. Mittra (Ed.), Pergamon, New York, Chapter 2, pp. 7-10, 1973.

[31] MATLAB – The MathWorks, Inc. <http://www.mathworks.com/products/matlab/>

[32] Mathematica – Wolfram < http://www.wolfram.com/mathematica/>

[33] Tsai, L., "A numerical solution for the near and far fields of an annular ring of magnetic current," Antennas and Propagation, IEEE Transactions on , vol.20, no.5, pp.569,576, Sep 1972

[34] Pozar, David M., Microwave Engineering. Hoboken: Wiley, 2009.

[35] C. A. Balanis, Advanced Engineering Electromagnetics, Hoboken: Wiley, 1989.

[36] Capdevila, S.; Jofre, L.; Romeu, J.; Bolomey, J.C., "Multi-Loaded Modulated Scatterer Technique for Sensing Applications," Instrumentation and Measurement, IEEE Transactions on , vol.62, no.4, pp.794,805, April 2013

[37] Microsemi, MicroSolutions – Microwave Diode Packages, Know What You Are Getting, K. R. Philpot, Microsemi-Lowell.

[38] Microsemi, MicroNote Series 701, PIN Diode Fundamentals, B. Doherty, Microsemi-Watertown.

[39] Fallahpour, M.; Ghasr, M.T.; Zoughi, R., "A multiband reconfigurable CPW-fed slot antenna," Antennas and Propagation Society International Symposium (APSURSI), 2012 IEEE , vol., no., pp.1,2, 8-14 July 2012

[40] Abou-Khousa, M.A.; Baumgartner, M.A.; Kharkovsky, S.; Zoughi, R., "Novel and Simple High-Frequency Single-Port Vector Network Analyzer," Instrumentation and Measurement, IEEE Transactions

[41] Jun Fan; Drewniak, J.L.; Knighten, J.L., "Lumped-circuit model extraction for vias in multilayer substrates," Electromagnetic Compatibility, IEEE Transactions on , vol.45, no.2, pp.272,280, May 2003

[42] Goldfarb, M.E.; Pucel, R.A., "Modeling via hole grounds in microstrip," Microwave and Guided Wave Letters, IEEE , vol.1, no.6, pp.135,137, June 1991

[43] TDK Corporation, [Online], Jan. 2014, Available: <http://www.tdk.co.jp/tefe02/e521_mlk.pdf>

[44] Paul, Clayton R., Introduction to Electromagnetic Compatibility. Hoboken: Wiley, 2006.

[45] Microsemi Corporation, [Online], Mar. 2014, Available: <http://www.microsemi.com/document-portal/doc_download/8703-gc4200-series-pdf>

[46] Agilent Technologies, Inc, [Online], Mar. 2014, Available: <http://cp.literature.agilent.com/litweb/pdf/5968-5160E.pdf>

[47] Navidi, William, Statistics for Engineers and Scientists, 2nd ed. New York: McGraw-Hill, 2008.

[48] Rao, K. V S, "An overview of backscattered radio frequency identification system (RFID)," Microwave Conference, 1999 Asia Pacific , vol.3, no., pp.746,749 vol.3, 1999

[49] Asl, S.E.; Ghasr, M.T.; Zawodniok, M.; Robinson, K.E., "Preliminary study of mutual coupling effect on a passive RFID antenna array," Instrumentation and Measurement Technology Conference (I2MTC), 2013 IEEE International , vol., no., pp.138,141, 6-9 May 2013

[50] Sample, A.P.; Yeager, D.J.; Powledge, P.S.; Mamishev, A.V.; Smith, J.R., "Design of an RFID-Based Battery-Free Programmable Sensing Platform," Instrumentation and Measurement, IEEE Transactions on , vol.57, no.11, pp.2608,2615, Nov. 2008

VITA

Dylan Andrew Crocker was born in Rolla, Missouri and raised on a small farm near Lebanon, Missouri. He was homeschooled until attending community college at Ozarks Technical Community College in Springfield, Missouri before transferring to the Missouri University of Science and Technology in 2009. He received his B.S. in Electrical Engineering (*Summa Cum Laude*) in December 2011 and the M.S. in Electrical Engineering degree in May 2014 from the Missouri University of Science and Technology.

Dylan worked as a LEAD tutor as well as an undergraduate research assistant at the Applied Microwave Nondestructive Testing Laboratory (*amntl*) while an undergrad at the Missouri University of Science and Technology. He also worked a Co-op with Hunter Engineering in St. Louis, Missouri as well as an internship at Associated Electric in Springfield, Missouri before completing his BSEE. After graduating with his BSEE in 2011 Dylan began working for Sandia National Laboratories in Albuquerque, New Mexico. At Sandia, he participated in the Critical Skills Master's Program which supported his MSEE degree. During his MSEE degree Dylan conducted his thesis research at the *amntl*.

Dylan is married to his wife Grace and they have two children Karis and Andrew. Dylan and his family enjoy spending time with friends and family and participating in their local Church.